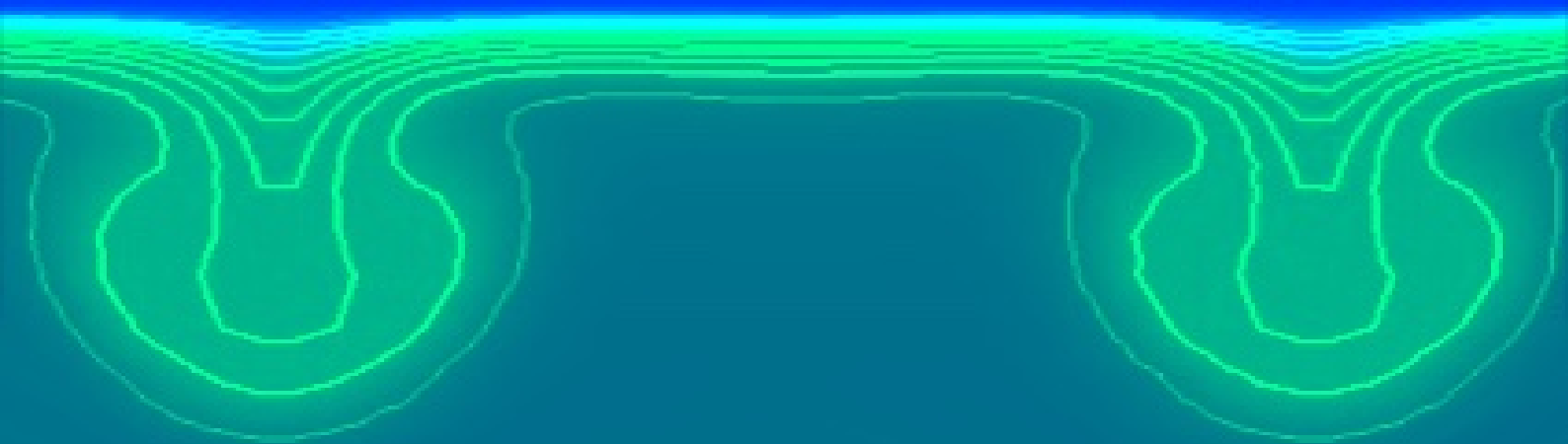


# Secondary Flows in Asymmetrical Contractions

A Numerical Study

Pranav Rajah Molahalli

*Master of Science Thesis*





# Secondary Flows in Asymmetrical Contractions

A Numerical Study

by

Pranav Rajah Molahalli

to obtain the degree of Master of Science  
at the Delft University of Technology,  
to be defended publicly on Monday, October 31 , 2022 at 10:00 AM.

Student number: 5217113  
Project duration: January 1, 2022 – October 31, 2022  
Thesis committee: Prof. R. Pecnik, TU Delft, Supervisor and Chairman  
Dr.ir. J.W.R Peeters, TU Delft  
ir. M. Draskic, TU Delft, Daily Supervisor  
Daily Supervisor : M.Sc. P.C Boldini, TU Delft

An electronic version of this thesis is available at <http://repository.tudelft.nl/>.



# Acknowledgements

My thesis journey for the last ten months has been one of the most challenging but inspiring learning experiences of my life. This journey would not have been possible without the support of many people who have helped me all along.

I would first like to thank my thesis supervisor, Professor Rene Pecnik, for his help and guidance throughout my research. His valuable inputs on my work and enriching and thought provoking discussions that we had, enabled me to develop critical thinking and delve deeper into the field of fluid dynamics.

I would like to express my gratitude to my daily supervisor Marko Draskic for his constant support throughout this journey. His patience, enthusiasm and his ability to explain concepts with clarity has helped me immensely in the writing of my thesis. I am also grateful to my daily supervisor Pietro Boldini for his insightful comments which helped me develop a better understanding of various CFD concepts involved in the thesis.

I am very thankful to Ben and Asif for their assistance and guidance throughout the project.

I would like to express my sincere gratitude to Dr. Juriaan Peeters for being a part of my thesis committee and reading my thesis.

I am also grateful to every single one of my friends who has been on this journey with me for the last two years. Their emotional support since the very beginning helped me cope with being away from home for the last two years.

Finally, I would like to thank my family without whom none of this would be possible. Their constant encouragement and support have helped me stay motivated and complete this exciting and fulfilling two-year journey.



# Abstract

Due to the global energy crisis, there is a growing need to make industrial processes more efficient and clean. One such method is to use effective and renewable working fluids in power and refrigeration cycles. Research in this field during the past decade has placed supercritical CO<sub>2</sub> (SCO<sub>2</sub>) in the forefront due to its non-ideal properties and abundance in nature but, to fully understand their heat transfer properties, insight into boundary layer flow and hydrodynamic instabilities are crucial. Experimental setups such as closed loop wind tunnel contraction facilities are needed which provide a laminar steady flow to take boundary layer measurements. However, using a contraction causes various problems such as formation of secondary flows like boundary layer separation, Gortler vortices, cross-flows and non-uniformity's. In this study a novel 1D contraction shape with curvature on only one side is proposed. This will completely eliminate the risk of Gortler vortices on the bottom plate and make it a suitable candidate for boundary layer experiments. Nevertheless, the risk of the other secondary flows and Gortler vortices on the top wall disturbing this laminar flow remains. Hence, the present research aims to optimise this 1D contraction to reduce the risk of such secondary flows and analyse the growth of Gortler vortices on the top wall using numerical simulations.

Steady state laminar simulations were performed to optimise the design of the 1D wind tunnel contraction. Optimum contraction and settling chamber lengths were found by identifying the risk of flow separation and boundary condition effects respectively. For the optimisation of the contraction wall shape, a family of transformed fifth order polynomial curves with varying inflection point distances were selected. To identify the curve with least risk of boundary layer separation and lowest flow non-uniformity, a multi-objective optimisation procedure was implemented. The procedure found that a curve with inflection point of 101mm downstream of contraction inlet gives the best performance.

To analyse the effect of Gortler vortices on outlet uniformity, unsteady laminar simulations were performed on the contraction by forcing sinusoidal perturbations of different wavenumbers. This study found that perturbations form symmetrical steady stream-wise Gortler vortices in the contraction. The most unstable wavenumber was found to be  $\lambda=83.33 \text{ m}^{-1}$  which formed secondary vortices of high vorticity. However it was also seen that for all wavenumbers, the vortices lose energy as they exit the contraction and do not affect the bottom boundary layer. Further, the effects of a side-wall on the formation of Gortler vortices were also investigated. The results showed that the Gortler vortex closest to the wall is absorbed into high vorticity corner vortices, while those close to the centre-line develop into steady Gortler vortices. No effect on the centre-line velocity profile was seen due to the vortices making the 1D contraction suitable for boundary layer experiments. Finally, it was also seen that the 1D contraction shape produces asymmetrical Gortler vortices due to alternative perturbation methods such as random inlet perturbations.



# Nomenclature

$\delta_1$	Displacement Thickness
$\dot{m}$	Mass Flow Rate (Kg/s)
$\Gamma$	Circulation ( $\text{m}^2/\text{s}$ )
$\lambda$	Wavelength (m)
$\mu$	Dynamic Viscosity (Pa-s)
$\nu$	Kinematic Viscosity ( $\text{m}^2/\text{s}$ )
$\omega$	Angular Frequency (1/s)
$\rho$	Density ( $\text{Kg}/\text{m}^3$ )
$\sigma$	Standard Deviation
$\tau$	Shear Stress (Pa)
$\theta$	Momentum Thickness
$C_{pe}$	Pressure Coefficient Minimum
$C_{pi}$	Pressure Coefficient Maximum
$f$	Brassard Transformation Parameter
$G$	Gortler number
$h$	Contraction Height (m)
$H_i$	Contraction Inlet Height (m)
$H_o$	Contraction Outlet Height (m)
$L_c$	Contraction Length (m)
$Ma$	Mach Number
$R$	Radius of Curvature (m)
$Re$	Reynold's Number
$t$	Time (s)
$U_\infty$	Free-stream Velocity (m/s)
$U_\tau$	Friction Velocity (m/s)
$U_b$	Bulk Velocity (m)
$U_{inlet}$	Mean Velocity Settling Chamber Inlet
$w$	Contraction Width (m)
$x$	Stream-wise Coordinate (m)
$y$	Wall Normal Coordinate (m)
$z$	Span-wise Coordinate (m)



# List of Figures

1.1	Contraction and test section Connected to Natural Convection Loop	2
1.2	2D Contraction	2
1.3	3D Contraction	2
1.4	1D Contraction	3
1.5	Main Components of a Wind Tunnel Facility	4
1.6	Boundary Layer separation over Airfoil by Sturm et al 2012 [8]	5
1.7	Contraction length vs non-uniformity showing boundary layer detachment at the two ends [13]	6
1.8	Matched Cubic Polynomial T.Morel 1975 [11]	6
1.9	Plot Dimensionless x distance $x/L_c$ vs height (mm) of wall shapes with varying parameter $f$	7
1.10	Cross flow on swept wing Dagenhart 1999 [18]	8
1.11	Boundary Layer Growth Seyyedi et al 2019 [22]	8
1.12	Displacement Thickness Schlichting 2015 [23]	9
1.13	Momentum Thickness Hafeez 2020 [24]	9
1.14	Wing-tip vortex due to aircraft wing	11
1.15	Taylor Vortices Between Two Cylinders Childs 2011 [31]	11
1.16	Dean vortices formation in a curved pipe Kalpakli 2012 [33]	12
1.17	Gortler vortices on a concave surface Floryan 1991 [36]	12
1.18	Gortler vortices on a concave surface Floryan 1991 [36]	13
1.19	Formation of streaks and subsequent breakdown to turbulence in Rayleigh scattering experiment 2021 [47]	14
1.20	Inflectional velocity profiles generated due to up-wash regions 2005 [49]	15
1.21	Non-dimensional Stream-wise Velocity contours on a XZ plane showing the formation of streaks and transition to Turbulence 2018 [54]	17
1.22	Non-dimensional Stream-wise Velocity contours on a XZ plane showing the formation of streaks and transition to Turbulence 2018 [50]	17
2.1	1-D contraction Geometry	22
2.2	Top View Of Contraction: Periodic Boundaries on either side of Contraction	28
2.3	Domain-1 (25mm)	29
2.4	Domain-2 (12mm)	29
2.5	Domain-3 (25mm)	30
2.6	Side-View-Shows Bias in Wall Normal and stream-wise direction	31
2.7	Isometric View of Contraction	32
3.1	Poly-line along Centre line symmetry of Geometry - Marked in Red	35
3.2	X-Distance vs X- Pressure Gradient along Poly-line	35
3.3	X-Distance vs X-Pressure Gradient Plot- Zoomed in View	36
3.4	X-Wall Shear 175mm contraction	36
3.5	X-Wall Shear 165mm contraction	36
3.6	Pressure contours Inlet length 60mm	38
3.7	Pressure contours Inlet length 80mm	38
3.8	Plot Parameter $f$ vs $Re_{\delta_{1cr}}$	39
3.9	Plot Parameter $f$ vs $\sigma_p$	39
3.10	Vertical Pressure Line at Outlet X=0.175m	40
3.11	Vertical Pressure Line 75mm Downstream of Outlet X=0.25m	40
3.12	Plot X-distance vs Pressure Deviation $\sigma_p$ for different $f$ values	40
3.13	Pressure Gradients in X- Direction for Different f values	41

3.14 Plot Parameter $f$ vs Maximum Pressure Gradient	41
3.15 Reynolds boundary layer $Re_{\delta_{1out}}$ Outlet	42
3.16 Objective Space $F_1$ vs $F_2$	43
3.17 Optimal Points- Weighted Sum Method	43
3.18 Distance From Ideal Point (0,0)	43
3.19 Plot Parameter $f$ vs Minimum Distance from Ideal Point (0,0)	44
3.20 $f=0.7$ Contraction shape and Inflection Point Distance used for experiments	44
4.1 X-Velocity Contour Unsteady- Domain-2	47
4.2 X-Velocity Contour Steady - Domain-2	47
4.3 Unsteady vs Steady Velocity Profile Outlet Comparison - Domain 2	48
4.4 Velocity Profile - Zoomed in View	48
4.5 X-Vorticity Contour Steady- Domain 3	48
4.6 X-Vorticity Contour Unsteady- Domain 3	48
4.7 Unsteady vs Steady Simulation Velocity Profile Outlet Comparison: Domain 3	49
4.8 Velocity Profile - Zoomed in View	49
4.9 X-Velocity Contour Plot of Initial Perturbation on YZ-Plane at X=-54mm	50
4.10 YZ planes at different x distances to visualise vortex growth	50
4.11 Growth of Gortler Instability shown by x-velocity contour plot from x=0 to x=0.175	51
4.12 (a) Experimental Benmalek 1993 [70] (b) DNS Mendez et al 2018 [50] (c) Present work comparison on mushroom structure in Gortler Instability.	51
4.13 Growth of Gortler Instability shown by x-vorticity contour plot from x=0 to x=0.175	52
4.14 Secondary Instability in DNS by Ren and Fu 2015 [73]	52
4.15 Secondary instability formed within contraction in present study	52
4.16 Iso-surface of Maximum values of Clockwise (Blue) and Counter- Clockwise Vorticity (Red)	53
4.17 X-Velocity Contour Plot of Initial Perturbation on YZ-Plane at X=-54mm	53
4.18 Growth of Gortler Instability shown by x-velocity contour plot from x=0 to x=0.175	54
4.19 Growth of Gortler Instability shown by x-vorticity contour plot from x=0 to x=0.175	54
4.20 Iso-surface of Maximum values of Clockwise (Blue) and Counter- Clockwise Vorticity (Red)	54
4.21 X-Velocity Contour Plot of Initial Perturbation on YZ-Plane at X=-54mm	55
4.22 Growth of Gortler Instability shown by x-velocity contour plot from x=0 to x=0.175	55
4.23 Growth of Gortler Instability shown by x-vorticity contour plot from x=0 to x=0.175	56
4.24 Iso-surface of Maximum values of Clockwise (Blue) and Counter- Clockwise Vorticity (Red)	56
4.25 X-Velocity Profile Showing Initialisation of Inflection Point formation at x=0.030m in upwash region	58
4.26 X-Velocity Profile Showing Inflection Point at x=0.060m in upwash region	58
4.27 X-Velocity Profile Showing Inflection Point at x=0.060m in upwash region	58
4.28 X-Velocity Profile Showing Inflection Point Vanishing at x=0.160m in upwash region	58
4.29 Streak formation in X-Wall Shear Stress Distribution on Top Wall of Contraction	58
4.30 Upwash and Downwash generated by Gortler Vortices	59
4.31 Evolution of Periodic X Wall Shear Stress Distribution as Flow Evolves in Contraction	59
4.32 Growth of Gortler Instability shown by x-velocity contour plot from x=0 to x=0.175	60
4.33 Unsteady Solution: X- Vorticity without Perturbations at Contraction Outlet x=0.175	60
4.34 Unsteady Solution: X- Vorticity with additional Gortler Vortices at Contraction Outlet x=0.175	60
4.35 Z-Velocity Contours to Show Extent of Contraction outlet affected by Corner and Gortler Vortices	61
4.36 Unperturbed Simulation Centre-Line X- Velocity vs Y-Coordinate at X=0.175	61
4.37 Perturbed Simulation Centre-Line X- Velocity vs Y-Coordinate at X=0.175 with Gortler Vortices	61
4.38 X-Velocity Contour Show Unsteady Gortler Vortices at X=0.060 due to inlet turbulence of 5%	62
4.39 Asymmetric Gortler Vortices seen in DNS results of Schrader et al.[51]	62
A.1 Number of Elements in Mesh vs Mean Velocity Plot to Show Mesh Independence	67

---

B.1 Number of Elements in Mesh vs Mean Velocity Plot to Show Mesh Independence . . . 69



# List of Tables

2.1	Fixed Dimensions in Optimisation . . . . .	22
2.2	System parameters at Design Conditions . . . . .	28
2.3	Summary of Domain type for each simulation . . . . .	29
2.4	Steady State Laminar Simulations Details . . . . .	33
2.5	Transient Laminar Simulations (Without Side Walls) Details . . . . .	34
2.6	Unsteady Laminar Simulations (With Side Walls) Details . . . . .	34
2.7	Large Eddy Simulation Details . . . . .	34
3.1	Presence of Flow Reversal at Different Contraction Lengths . . . . .	37
4.1	Comparison of Steady and Unsteady Flow Parameters- Domain 2 . . . . .	48
4.2	Pressure Profile Non-Uniformity Comparison of Steady and Unsteady Simulations . . . . .	49
A.1	Summary of Domain type for each simulation . . . . .	67
B.1	Perfromance Comparision of 6th order to 5th Order Polynomial . . . . .	69



# Contents

<b>1</b>	<b>Introduction</b>	<b>1</b>
1.1	Background . . . . .	1
1.2	Literature Review . . . . .	3
1.2.1	Wind tunnel facilities . . . . .	3
1.2.2	Secondary Flows and Optimisation . . . . .	4
1.2.3	Gortler Vortices in the contraction . . . . .	10
1.2.4	Literature Summary . . . . .	17
1.3	Thesis Objectives. . . . .	18
1.3.1	Research Objective 1 . . . . .	18
1.3.2	Research Objective 2 . . . . .	18
1.4	Scope of Study and Chapter Overview . . . . .	18
<b>2</b>	<b>Methodology</b>	<b>21</b>
2.1	Physical Domain and Geometry . . . . .	21
2.2	Steady State Analysis . . . . .	23
2.2.1	Settling Chamber Length. . . . .	23
2.2.2	Contraction Length . . . . .	23
2.2.3	Contraction Wall Shape . . . . .	23
2.2.4	Flow Parameters Analysed to Find Wall Shape Performance . . . . .	24
2.2.5	Optimisation Method . . . . .	25
2.3	Unsteady Analysis . . . . .	26
2.3.1	No Perturbations . . . . .	26
2.3.2	Perturbations Introduced to Flow Field . . . . .	26
2.4	Boundary Conditions and Computational Domain . . . . .	27
2.4.1	Boundary Conditions . . . . .	27
2.4.2	Computational Domain. . . . .	28
2.5	Computational Mesh . . . . .	30
2.6	Governing Equations: Incompressible Navier Stokes Equations . . . . .	32
2.6.1	Numerical Techniques . . . . .	32
2.7	Simulation Overview . . . . .	33
2.7.1	Chapter Summary . . . . .	34
<b>3</b>	<b>Results and Discussion- Shape Optimisation</b>	<b>35</b>
3.1	Contraction Length . . . . .	35
3.2	Settling Chamber Length. . . . .	37
3.3	Contraction Wall Shape Optimisation . . . . .	38
3.3.1	Qualitative effect of Changing Wall Shapes. . . . .	38
3.3.2	Multi-objective Optimisation . . . . .	42
<b>4</b>	<b>Results and Discussion- Unsteady Simulations</b>	<b>47</b>
4.1	Unsteady (Without Perturbations) . . . . .	47
4.1.1	Domain-2 . . . . .	47
4.1.2	Domain-3 . . . . .	48
4.2	<b>Unsteady Laminar With Perturbations (Without Side Walls)</b> . . . . .	<b>49</b>
4.2.1	Perturbation Wave-number = $83.33m^{-1}$ (1 Sine Wave) . . . . .	50
4.2.2	Perturbation Wave-number= $166.66m^{-1}$ (2 Sine Waves) . . . . .	53
4.2.3	Perturbation Wave-number= $250m^{-1}$ (3 Sine Waves) . . . . .	55
4.2.4	Higher Wave-numbers . . . . .	56
4.2.5	Comparison of Different Perturbations . . . . .	57
4.2.6	Secondary Instabilities and Inflectional Velocity Profiles . . . . .	57
4.2.7	Effects of Gortler Vortices on Wall Shear in Contraction . . . . .	57

---

4.3	<b>Unsteady Laminar With Perturbations (With Side Walls)</b> . . . . .	59
4.4	Alternative Perturbation method: Random Inlet Turbulence . . . . .	62
<b>5</b>	<b>Conclusion</b> . . . . .	<b>63</b>
5.1	Summary . . . . .	63
5.2	Recommendations and Scope for Future Research . . . . .	64
<b>A</b>	<b>Appendix</b> . . . . .	<b>67</b>
A.1	Mesh Independence study . . . . .	67
<b>B</b>	<b>Appendix</b> . . . . .	<b>69</b>
B.1	Sixth Order Polynomial Shape . . . . .	69

# Introduction

## 1.1. Background

Climate change has become one of the greatest problems faced by humankind in the 21<sup>st</sup> century. The exploitation of natural non-renewable resources such as fossil fuels have caused widespread pollution leading to global warming. It is predicted by Stocker et al 2013 [1] that if current trends continue without immediate greenhouse gas mitigation efforts, by the year 2030 the average global temperature rise could be as high as 2°C for certain countries. Hence there is an urgent need to move towards renewable energy and more efficient systems.

Industrialisation has been identified as one of the leading causes for climate change. It is imperative that industries across the world update and innovate their current processes before irreversible damage is caused. This has led to growing research on innovative techniques to improve the efficiency and environmental impact of industrial processes. One such innovation has been in the field of novel working fluids for power cycles such as supercritical carbon dioxide (SCO<sub>2</sub>) to replace conventional fluids. It has been found by Ahn et al 2015 [2] that SCO<sub>2</sub> power cycles give a higher efficiency for mild turbine inlet temperatures when compared to other systems. This is because they require lower compressor work input due to their novel real gas properties near the critical point. They are also more compact and have a higher power density than conventional systems due to high pressures and densities. SCO<sub>2</sub> is also a non-toxic, non-flammable, non-carcinogenic and thermodynamically stable alternative. It has a low critical temperature and a relatively low critical pressure. These properties make SCO<sub>2</sub> a forerunner of the working fluids of the future.

However, the use of SCO<sub>2</sub> in power cycles has its challenges due to the non-ideal behaviour of SCO<sub>2</sub> near the Widom line, where large gradients of density and viscosity are seen on heating. This behaviour can also cause changes to the hydrodynamic stability of the fluid as shown by Ren and Pecnik 2019 [3]. Understanding the intricacies of these instabilities and their possible transition to turbulent flow is of great importance since they can affect the overall heat transfer and efficiency of the system.

To investigate these instabilities in SCO<sub>2</sub> experimentally, a low speed wind tunnel facility for boundary layer measurements is currently under construction in the Process and Energy lab in TU Delft. This setup will consist of a vertical natural convection loop to drive the flow, and heat transfer measurements will be taken in a test section to understand the transition of the boundary layer. As shown in Fig. 1.1, the main parts of the contraction include two differentially heated vertical legs, a settling chamber, screens, honeycombs, a contraction, a diffuser and a test section. This wind tunnel facility does not contain a leading edge in the test section to generate a growing boundary layer due to size and space restrictions in high pressure system. Hence the boundary layer measurements will be taken on the bottom wall of the test section channel itself.

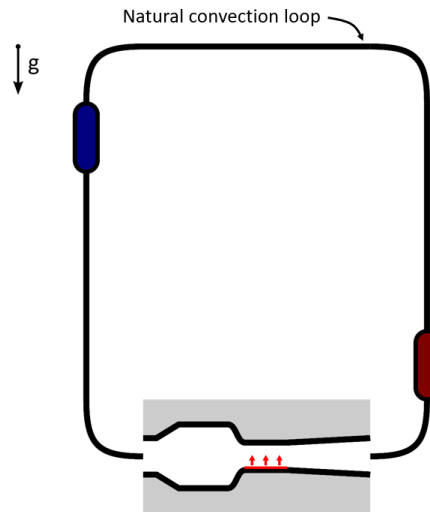


Figure 1.1: Contraction and test section Connected to Natural Convection Loop

One major challenge in the construction of such a facility is in the design of the contraction section. The instability experiments will be possible only if a laminar flow is achieved at the inlet of the test section. Due to the curvature, presence of edges and varying cross section, contractions are inherently prone to various secondary flows such as boundary layer separation, edge flows and cross flows. Additionally, due to the low kinematic viscosity of  $\text{SCO}_2$ , they have high Reynolds numbers even in low-speed wind tunnels. This causes a risk of curvature induced instabilities to form in the contraction called Gortler vortices. Using a conventional 2D or 3D wind tunnel as show Fig.1.2 and Fig. 1.3 can lead to a formation of these vortices on the top and bottom walls which would render the experimental setup invalid.

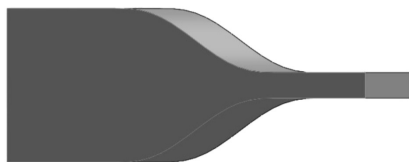


Figure 1.2: 2D Contraction

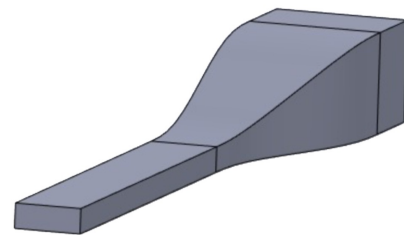


Figure 1.3: 3D Contraction

To circumvent the problem of Gortler vortices on the bottom boundary layer, this thesis proposes a novel 1D contraction as shown in Fig. 1.4. However the problem of other secondary flows in the contraction and Gortler vortices on the top boundary layer still exist. Hence, this research will aim to optimise this contraction and show through numerical simulations that the proposed geometry is successful in producing a laminar boundary layer on the bottom wall as per the requirement of the experimental facility.



Figure 1.4: 1D Contraction

As this contraction type has not been used previously for boundary layer measurements, a comprehensive literature study will be performed to understand the numerical methods, optimisation techniques and perturbation analysis that can be used to understand the flow through this 1D contraction.

The present study will aim to answer the following broad research questions:

1. What is the optimum contraction length and settling chamber length for this experimental setup?
2. Which wall curvature function and inflection point distance gives the best performance for a 1D contraction?
3. Is the flow through the contraction stable and steady after the addition of perturbations?
4. What wavenumber of the perturbation is most unstable?
5. Do the Gortler vortices effect the bottom boundary layer on which heat transfer boundary measurements are to be take?

## 1.2. Literature Review

This section contains a literature review of the research relevant to the wind tunnel contractions, secondary flows in contractions, contractions optimisation and the Gortler instability. The section will be divided into three subsections, the first will give a brief introduction to wind tunnel facilities, the second will detail the optimisation and secondary flows in a wind tunnel contraction, while the second will discuss existing literature on the Gortler instability and vortices.

### 1.2.1. Wind tunnel facilities

A wind tunnel facility is a setup used for blowing fluids through a test section for the replication of aerodynamics and flow phenomena. They can be constructed in a wide range of sizes depending on their purpose of application, from large wind tunnels for aeronautical studies, to smaller wind tunnel in academic laboratories. They can be categorised into two main types depending on the velocity of the fluid flow in the system, low speed wind tunnels where the Mach number  $Ma < 0.3$  and high speed wind tunnels where  $Ma > 0.3$ .

Wind tunnels can also be categorised on the setup of the circuit used to transport the fluid. A closed wind tunnel consists of a closed loop of fluid that is recirculated inside the system, while an open loop takes ambient air which it drives through the tunnel. An example of a wind tunnel with its main parts named is shown in Fig 1.5.

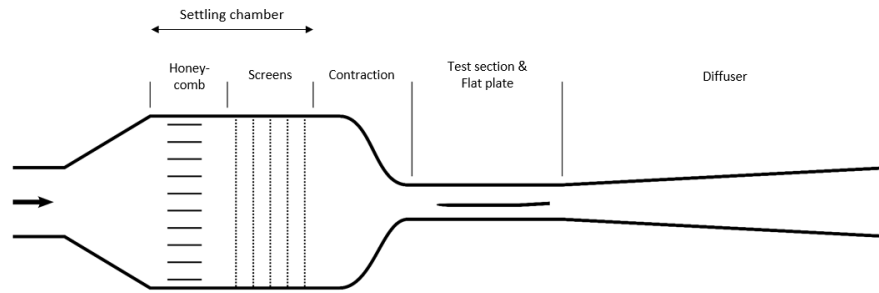


Figure 1.5: Main Components of a Wind Tunnel Facility

A short description of the main components of a wind tunnel facility shown in Fig 1.5 are given below.

(a) Settling Chamber- This is the channel before the contraction that houses the various turbulence reduction devices such as honeycombs and screens. The honeycomb structures are long hexagonal tubular structures that reduce lateral turbulence and swirl in the flow 1989 [4]. The screens also reduce turbulence by removing all lengths scales larger than the mesh size of the screen. These structures might add some small scale turbulence to the system, however these scales are dissipated much faster in the mean flow.

(b) Test Section- This is the channel in which the required measurements are taken. The wind tunnel facility design should be such that the flow entering the test section should be as uniform and laminar a flow as possible.

(c) Diffuser- The diffuser is used for the purposes of pressure recovery in the setup. This is done to decrease dynamic pressure to ensure that the pressure losses in the screens and honeycombs are kept to a minimum. There is also a risk of boundary layer separation in the contraction, however additional screens can reduce this risk as shown by Bell and Mehta 1989 [4].

(d) The wind tunnel contraction is described in section 1.1. The contraction is susceptible to various secondary flows such as boundary layer separation, cross flows and edge flows. Hence its design is crucial to the functioning of the wind tunnel facility. The following subsections will go deeper into existing literature on contraction design.

### 1.2.2. Secondary Flows and Optimisation

A wind tunnel contraction is a channel of varying cross section. For low speed flows ( $Ma < 0.1$ ), the contraction follows the principle of conservation of mass for a channel flow. As the section decreases in the stream-wise direction, the flow is accelerated to ensure that the same amount of mass leaves the contraction. The contraction has multiple uses in a wind tunnel facility which are detailed below.

(a) Reduce turbulence levels in the fluid flow by decreasing the fluctuating velocities as a fraction of the mean flow velocity ( in the stream-wise direction).

(b) Reduce boundary layer thickness at the entrance of test section.

However there is still a risk of various secondary flows that can form in the contraction. Secondary flows are all those flows that cause deviations from uniform laminar stream-wise velocity. These flows affect the flow uniformity at the contraction outlet which renders it unsuitable for its experimental applications. In this subsection a review of these secondary flows and the optimisation and design techniques found in literature are summarised.

## Boundary Layer Separation

The contraction consists of a concave section and a convex section which are joined together at an inflection point. These curvatures inherently lead to the formation of adverse pressure gradients near the inlet and outlet of the contraction. Adverse pressure gradients occur when there is an increase in the static pressure of the fluid in the stream-wise direction. As the fluid flows through the contraction on average the velocity increases, however near the wall local curvature effects dominate the flow. These lead to a minima of velocity to occur within the contraction at the inlet. Similarly a maxima of velocity occurs within the outlet. This non-monotonous increase in velocity leads to pressure gradients in the contraction. This behaviour was also analytically identified by Tsien 1949 [5] and Cohen et al 1962[6] where they found that for a finite length contraction it was impossible to avoid the presence of adverse pressure gradients. Rouse and Hassan 1949 [7] experimentally confirmed the presence of these adverse gradients in contractions.

Adverse pressure gradients in a boundary layer where the momentum is low can lead to flow stoppage or reversal. This flow reversal characterised by the velocity gradient  $\frac{du}{dy}$  going from positive, to zero to negative. Flow reversal can lead to a phenomenon known as boundary layer separation which is characterised by sudden thickening and unsteadiness of the boundary layer. Fig. 1.6 shows boundary layer separation flow reversal over a curved airfoil surface.

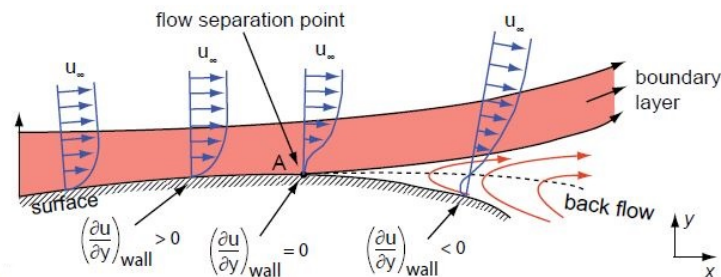


Figure 1.6: Boundary Layer separation over Airfoil by Sturm et al 2012 [8]

Boundary layer separation is of greater importance in relation to laminar boundary layers. This is because, unlike turbulent flows where high momentum fluid is transferred to the boundary layer, laminar flows have a well defined low momentum region that is susceptible to flow reversal. This boundary layer separation can cause unsteadiness effects in the flow which can disturb the laminar boundary layer required in low speed wind tunnels. Hence there has been widespread research on contraction design to reduce the risk of boundary layer separation.

One of the first analytical results on separation criteria for laminar and turbulent boundary layers was proposed by Stratford 1954 and 1959 [9] [10]. This result is widely used as an estimate to predict boundary layer separation in contraction design and related the pressure gradients in the contraction to the Reynold's number(Re). Stratford's criteria was used by Thomas Morel to design axi-symmetric 1975 [11] and 1977 [12] 2D contractions. In this method the maximum and minimum coefficient of pressure values ( $C_{pi}$  and  $C_{pe}$ ) were set by Morel before hand so as to satisfy the Stratfords criteria. He used this method to prepare design charts for different values of contraction ratio ( $CR = H_i/H_o$ ) and contraction length  $L_c$ .

The contraction length was seen to play a big role in the risk of boundary layer separation. Bell and Mehta 1988 [13] investigated the risk of boundary layer separation due to variation of the contraction length. They found that on increasing the contraction length the risk of separation at the inlet is reduced. However beyond a certain critical length, separation occurs at the outlet of the contraction. There results are shown in Fig.1.7.

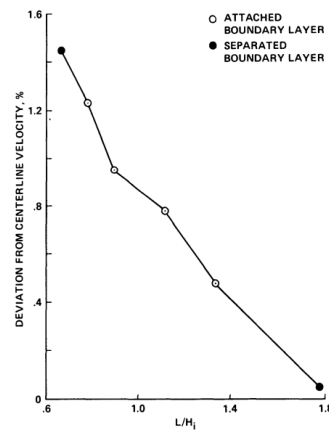


Figure 1.7: Contraction length vs non-uniformity showing boundary layer detachment at the two ends [13]

The effect of contraction length on boundary layer separation was also investigated by Mikhail and Rainbird 1978 [14] in their paper on the design of axi-symmetric contractions. They argued that boundary layer separation at the outlet is far more likely to occur in laminar flows than turbulent flows. Hence its importance in the design of the contraction should be relative to the flow type.

Another factor that greatly effects the the risk of boundary layer separation is the wall shape of the contraction. The earliest wall shapes used for contraction design had very little design procedure involved. Many contractions were built with "by- eye" estimates and hand drawings. Analytical work by Tsien 1943 [5] and Cohen 1962 [6] provided estimates of separation free wall shapes, however these solutions were for ideal infinitely long contractions which were of little practical use. Morel in his design for axisymmetric 1975 [11] and 2D contractions 1977 [12] used a matched cubic polynomial shape as shown in Fig. 1.8.

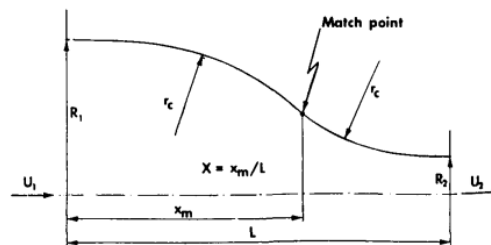


Figure 1.8: Matched Cubic Polynomial T.Morel 1975 [11]

He found that that this shape gave adequately low pressure maxima and minima in the contraction for a low contraction length. Morel also varied the inflection point distance of this curve  $x_m$  to generate a family of curves with different matching point values. It was seen that the more downstream the inflection point, the lower is the pressure maxima at the inlet and higher is the pressure minima at the outlet. Hence the region of greater separation risk changed with the inflection point.

Bell and Mehta 1988 [13] compared the matched cubic to a third, fifth and seventh order polynomial shape . They found that the fifth order polynomial gave the best performance with no separation and a lower boundary layer Reynolds number at the outlet. The fifth order polynomial has its inflection point at the centre of the contraction length. To generate a family of curves with varying inflection point distance, Brassard and Ferchichi 2005 [15] derived an analytical transformation of the Bell fifth order shape. The transformation equation is given by equation:

$$h = \left[ -\eta \left[ 1 - \left( \frac{H_o}{H_i} \right)^{\frac{1}{f}} \right] + 1 \right]^f \quad (1.1)$$

Where  $\eta$  is given by:

$$\eta = 10\xi^5 - 15\xi^4 + 6\xi^3 \quad (1.2)$$

Here a value of the Brassard parameter  $f < 1$  moves the inflection point downstream of the centre while a value of  $f > 1$  pushes it upstream. At  $f = 1$  the original Bell and Mehta polynomial is obtained. Fig. 1.9 shows the different wall shapes produced with varying parameter  $f$ .

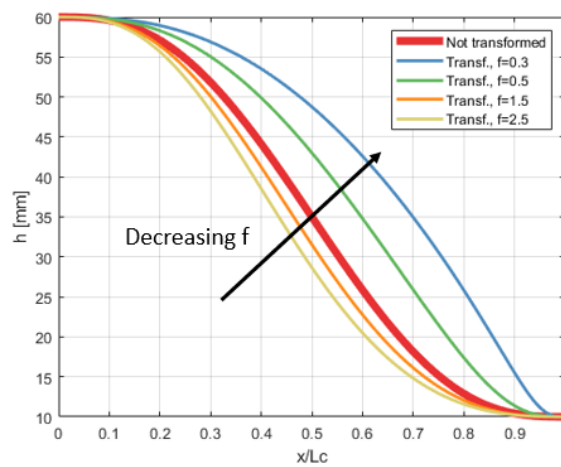


Figure 1.9: Plot Dimensionless  $x$  distance  $x/L_c$  vs height (mm) of wall shapes with varying parameter  $f$

A comparison of wall shapes with different fixed  $f$  values was made by Doolan 2007 [16] for 2D contractions. He used the existence of separation, outlet boundary layer Reynolds number and flow uniformity at the outlet to gauge the performance of the curves. He found that an  $f$  value close to 1 would be ideal for the contraction with a low risk of separation.

Another curve that was proposed by Sargison and Rossi 2004 [17] for low speed wind tunnels was the sixth order polynomial curve. This is a 7 parameter whose inflection point distance can be selected to generate the required curve. They saw that for the least risk of separation, the best performing curve is one which has its inflection point distance as downstream as possible while maintaining a monotonically decreasing wall contour. The sixth order curve also allows for control of the inlet and outlet curvature which can be set by the designer. However the wall contour without any inlet and outlet curvatures was found to perform the best.

### Cross-Flows

Cross-flows are secondary flows in the fluid that are perpendicular to the direction of the stream-wise flow. Cross-flows are generated due to three-dimensional effects which cause curvatures in the streamlines. Curvatures cause span-wise pressure gradients to form which lead to the cross-flows. A cross-flow on a streamline is shown in Fig 1.10.

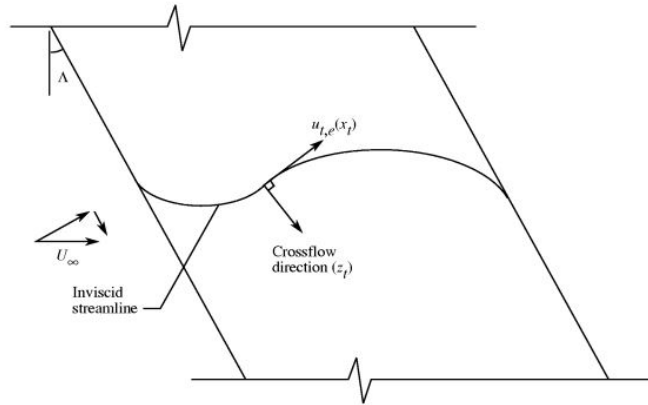


Figure 1.10: Cross flow on swept wing Dagenhart 1999 [18]

Cross-flows can cause unwanted thickening of the boundary layer and flow separation in the contraction. Yao 1991 [19] was the first to study cross-flows in the context of wind tunnel contractions. He found that the cross-flow was a strong function of contraction length. A larger contraction length reduced the risk of cross-flows. He also observed that cross-flows could be avoided by using a 2 dimensional or axi-symmetric contraction.

Mehta 1979 [20] in his PHD thesis found that any cross-flows caused by corner effects in 2D contractions remain localised and do not effect the centreline velocity of the test section.

### Boundary Layer Thickness

When viscous fluids flow over a surface, a thin layer of fluid with large velocity gradients is formed over the surface due to the no-slip condition at the fluid-wall interface, called the velocity boundary layer. The velocity in this region goes from zero at the wall to free-stream velocity of the initial flow. This concept was first theorised by Ludwig Prandtl in his ground breaking paper in 1904 [21]. This discovery simplified the analysis of flows over objects to a large extent since two distinct regions of flow could be identified, a free-stream flow which could be solved with inviscid analysis, and the boundary layer, which is solved including viscous effects. Fig. 1.11, shows a developing boundary layer.

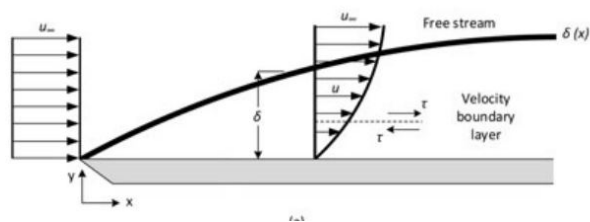


Figure 1.11: Boundary Layer Growth Seyyedi et al 2019 [22]

Boundary layer thickness can be defined in multiple methods. If defined as a mass flow deficit, the boundary layer thickness is called displacement thickness  $\delta_1(x)$ . Here it is taken to be that distance from the wall that a hypothetical fluid of freestream would have, to equal the mass flow rate of the true flow. This is shown in Fig. 1.12.

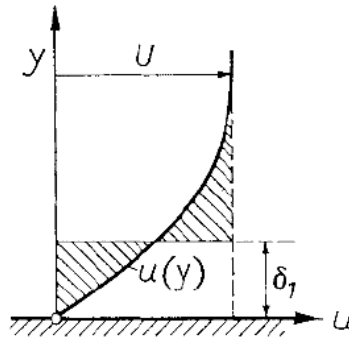


Figure 1.12: Displacement Thickness Schlichting 2015 [23]

For a laminar boundary layer obtained using the Blasius solution  $\delta_1(x)$  is given by:

$$\delta_1(x) = 1.7208 \sqrt{\frac{\nu x}{u_0}} \quad (1.3)$$

A similar definition can be made for the momentum flow rate and it is known as the momentum thickness given by  $\theta$  or  $\delta_2(x)$ . This is shown in Fig. 1.13.

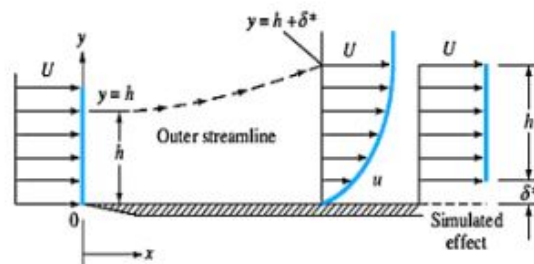


Figure 1.13: Momentum Thickness Hafeez 2020 [24]

For a laminar Blasius boundary layer the momentum thickness can be approximated by:

$$\delta_2(x) = 0.664 \sqrt{\frac{\nu x}{u_0}} \quad (1.4)$$

To have a velocity profile of maximum possible uniformity at the end of the contraction, the boundary layer thickness at the outlet has to be at a minimum. Research on contraction design aims to keep the boundary layer Reynolds number considering displacement thickness ( $Re_{\delta_1}$ ) at a minimum for the contraction. Bell and Mehta 1988 [13] used this criterion to determine the best performing wall shape, where they found that the fifth order polynomial gave a minimum.

### Non-uniformity at Outlet

The non-uniformity of the flow at the outlet of the contraction is its deviation from a channel flow. The non-uniformity occurs because the contraction causes streamlines to curve in the test section which

leads to a velocity overshoot at the top of the outlet. This causes an imbalance between the velocity field at the top of the outlet with respect to the bottom, causing a non-uniform profile. Different researchers have used different methods to define the non-uniformity at the outlet. Morel in his design for axisymmetric and 2D contractions defined the non-uniformity of the velocity field as  $u_2 = (V - U_e)/U_\infty$ . Another method of defining the non-uniformity of the velocity at the exit plane was used by Bell and Mehta 1988 [13] who took the standard deviation of the velocity profile. A similar approach of using section velocity profile to gauge non-uniformity was used by Fang et al 2001 [25]. They quantified the non-uniformity as a ratio of the maximum velocity deviation to the mean velocity.

Watmuff 1986 [26] qualitatively gauged the upstream and downstream distances from the contraction inlet and outlet within which non-uniformity's would be strong. This was done by looking at the pressure iso-contours linked with the contraction and their influence outside the contraction.

### Optimisation

Optimisation is a mathematical process by which the best possible output is obtained by choosing an optimum value of input parameters. Optimising generally involves the maximising or minimising of an objective function subject to some equality or inequality criterion. Wind tunnel contractions can be optimised to identify which shape configuration leads to least risk of different secondary flows explained in the previous subsections.

Most research on contraction design has focused on comparison of results obtained by simulating different wall shapes such as Doolan 2007 [16] and Bell and Mehta [13]. Only a few papers have been found that use true optimisation methods to obtain the best performing wall shape. Leifsson and Koziel 2015 [27] used a surrogate based optimisation (SBO) techniques that optimises a Bezier curve with five control points. The optimisation technique uses a low fidelity solver that is then compared with a high fidelity solver and experimental data to check for accuracy. The objective function to be minimised was the flow uniformity at the outlet of the contraction. The results from the SBO were successful in providing a wall shape with non-uniformity below acceptable levels.

Doolan and Morgans 2007 [28] built an optimisation software tool that numerically determines the best third order Bezier curve for given constraints. The constraints to be minimised were the boundary layer Reynolds's number at outlet, the flow non-uniformity and the risk of separation in the contraction. They used three different optimisation techniques to analyse their robustness, efficiency and accuracy of solution, Sequential Quadratic Programming (SQP), DIRECT and Efficient Global Optimization (EGO). They found that EGO was the most robust system and always produced acceptable solutions as long as the initial random sampled data was large enough.

### 1.2.3. Gortler Vortices in the contraction

#### Vortices

Vortices are a fluid flow phenomenon where there exists a rotating motion of the fluid around a centreline. Vortices can be found in a wide range of natural and industrial application, ranging from large scale cyclones to vortex tubes. Fig. 1.14 shows a vortex formed due to an aircraft's wing, known as a wing-tip vortex. The intensity of a vortex is quantified by a parameter known as the vorticity. The vorticity  $\omega$  is a vector field that is derived from the velocity field by taking the curl,  $\omega = \nabla \times u$ .

Vortices can be formed in several different ways depending on the flow phenomenon. One such mechanism is a centrifugal inviscid instability that occurs in shear flow over a concave surface. Taylor in his paper on revolving fluids was the first to describe this instability 1917 [29]. He noticed that, in fluid flow between revolving cylinder, beyond a certain angular velocity, stream-wise vortices are formed. He



Figure 1.14: Wing-tip vortex due to aircraft wing

showed that the sufficient condition for the formation of these vortices was a decrease in the circulation ( $\Gamma$ ) in the radial direction. However this condition is only a necessary condition for the instability and the presence of viscosity at low Reynold's could also stabilise the flow. This was shown by Taylor in his famous experimental work on concentric rotating cylinders 1923 [30]. He showed that until a certain velocity limit a Couette flow was maintained in the cylinders after which the instabilities, now known as Taylor vortices are formed. These vortices are shown in Fig. 1.15.

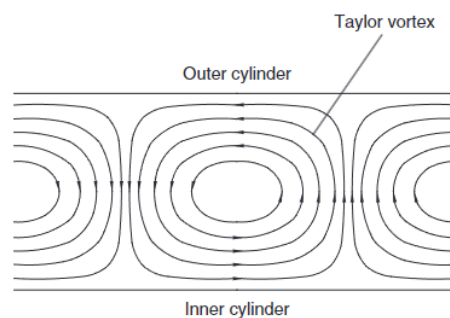


Figure 1.15: Taylor Vortices Between Two Cylinders Childs 2011 [31]

In a similar instability to Taylor vortices, Dean 1928 [32] found that fully developed flow in curved channels or pipes also produced stream-wise steady vortices, now known as Dean vortices. These are vortices that have open streamline unlike the Taylor vortices which are closed. The instability occurs in the bulk of the fluid in a channel or pipe that leads to momentum transfer in the span-wise direction. Dean vortices in a pipe are shown in Fig. 1.16.

A third kind of centrifugal instability that exists is the Gortler vortex, which occurs in curved boundary layer flows. In his paper on boundary layer flow on concave surfaces, Gortler found a generalisation of Rayleigh's inflection point criterion 1880 [34] showing that an inviscid centrifugal instability can form when there is a sign change of :

$$\frac{d^2U}{dy^2} + \frac{1}{R} \frac{dU}{dy} \quad (1.5)$$

In the limit of a flat plate where  $R \rightarrow \infty$ , this criterion reduces to Rayleigh's criterion as shown by

Gortler 1940 [35]. Gortler further found that this centrifugal instability was seen to be stabilising for two-dimensional disturbances, however three dimensional perturbations were successful in triggering

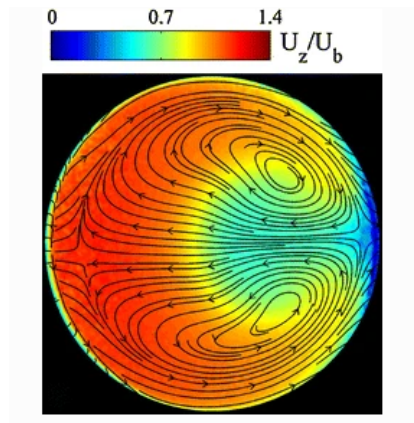


Figure 1.16: Dean vortices formation in a curved pipe Kalpakli 2012 [33]

the instability. He defined a non-dimensional parameter, now known as the Gortler number, to predict the onset of these vortices. The Gortler number is given by:

$$G = \frac{U_e \theta}{\nu} \left( \frac{\theta}{R} \right)^{1/2} . \quad (1.6)$$

The Gortler vortices are in the form of stream-wise counter-rotating vortices formed in the boundary layer of the flow. The counter-rotation forms alternating regions of up-wash and down-wash, where fluid is transported away from and to the boundary layer respectively. This momentum transfer leads to a change in the boundary layer thickness in the span-wise direction, with the boundary layer becoming thinner in regions of down-wash and thicker in regions of up-wash. The change in boundary layer thickness also leads to changes in parameters such as the wall shear stress distribution with region of down-wash having high wall shear stress and regions of up-wash having low wall shear stress. The vortices along with the stream-wise velocity profile on a concave flat plate are shown in Fig. 1.17.

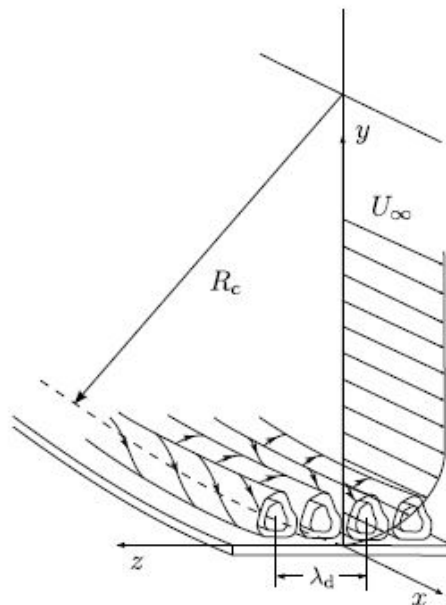


Figure 1.17: Gortler vortices on a concave surface Floryan 1991 [36]

Linear stability analysis has been used to understand the growth of Gortler vortices on curved surfaces due to infinitesimal disturbances. A locally parallel approximation was used by Floryan and Saric 1982 [37] to plot a 2-dimensional neutral stability curve between Gortler number  $G$  and non-dimensional wavenumber  $\beta$  for weakly concave surfaces. However the neutral stability curve is valid only for low  $G$  value, very large  $\beta$  and only plots the regions of steady vortical disturbances. The analysis showed that  $G=0.46$  or more would lead to these steady stable vortices in a Blasius boundary layer. Saric 1994 [38] also noted that for weak curvatures that produce stream-wise vortex growth of less than  $O(1)$ , the Gortler instability can be discerned from the boundary layer growth. The neutral stability curve is shown in Fig. 1.19

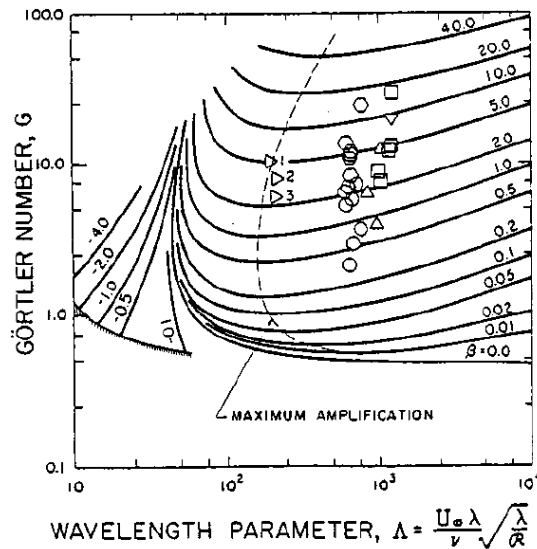


Figure 1.18: Gortler vortices on a concave surface Floryan 1991 [36]

It is seen from the neutral stability curve that there exists a certain cutoff wavelength of  $\lambda_c = 44.29$  below which the disturbances are only attenuated. A maximum amplification contour can also be defined at every value of  $\beta$  as shown in the figure.

The methods used for linear instability however were deemed to be inaccurate since they assumed a separation of variable in the derivation which made the flow independent of the stream-wise coordinate Mendez 2020 [39]. This led to the plotting of inaccurate neutral stability curves.

Floryan and Saric 1982 [37] also noted the large discrepancies obtained between different linear stability and experimental results. This was attributed to the sensitivity of the neutral curve on the geometry of the flow. They stated that the curvature of the streamlines played a large role in determining which wavelengths are amplified in the flow.

Hall 1983 [40] was the first to find a solution to this problem where he numerically integrated the flow equations. He concluded that the parallel flow approximations were erroneous since the ordinary differential equation approximations could not effectively capture the decay of vortices at the edge of the boundary layer. This inaccuracy led to artificial spreading of the neutral curve for higher wavelengths. Hall also concluded that a single critical Gortler number to define flow transition does not exist like parallel flows since the Gortler problem by its nature depends highly on the receptivity mechanism of the disturbances.

Recently, further advances were made on unsteady disturbances by Boiko et al 2017 [41], who described a three dimensional neutral stability surface. They plotted  $G$  and  $\beta$  along with the non-dimensional frequency parameter  $F$ . It was also shown that the formulating the receptivity problem to solve only the most unstable modes was more accurate than using different methods like the local approach that

solves only for a specific range of  $G$ .

### Experimental Studies

Apart from the fundamental research on the formation of Gortler vortices, there has been a surge in the experimental research on this instability in the past few decades. This is due to the fact that several industrial facilities use components with curved surfaces which leads to a risk of Gortler vortices. Even though Gortler vortices are steady vortices in a laminar flow, they can lead to secondary instabilities which can cause a transition of the flow from laminar to turbulence. This turbulence can cause changes in mixing and heat transfer of the process. This makes it even more important to fully understand the formation of Gortler vortices and its effect on different curved geometries.

Experiments to analyse the Gortler instability have been performed for a wide range of geometries for different speeds, from sub-sonic flow to super-sonic flow. The three main geometries used in literature are purely curved concave surfaces, curved surfaces with a flat plate and compression ramps. Different methods have been used by researchers to trigger the perturbations. To produce steady perturbations roughness elements are used with a constant span-wise wavelength. If unsteady perturbations are to be produced, a blowing and suction mechanism can be used where the fluid is injected into or sucked out of the boundary layer.

Various experiments have been performed to study the formation of Gortler vortices. The most common methods of experiments performed are the visualisation methods by Gregory and Waker 1956 [42], Beckwith and Holley 1981 [43] and the probe method Swearingen and Blackwelder 1987 [44] and Winoto et al 2005 [45]. Most experiments are performed on concave channels or plates of constant curvature.

Flow visualisation involves the addition of a dye or particles to the flow to observe time averaged flow structures. It is the oldest method of deriving valuable qualitative information from the Gortler instability. Ito 1987 [46] studied the two dimensional characteristics of the Gortler vortices using visualisation techniques by introducing stream-wise smoke tracers on a uniform concave flat plate. The idea was that when vortices form the up-wash created would cause the smoke stream lines to converge. He found that the vortices evolve spatially and have a convective nature in the stream-wise direction. The vortices however evolve very slowly and no visual change is seen until a Gortler number of  $G=10.1$ . The Gortler vortices formed were also seen to be steady vortices.

More recently Huang et al 2021 [47] performed visualisation experiments on a hypersonic concave surface. This experiment had the added ability of visualising the vortex formation in three dimensions, in comparison to the planar view of previous experiments. This was performed using CO<sub>2</sub>-enhanced filtered Rayleigh scattering flow visualization. Roughness elements with a constant span-wise wavelength were used for the initial perturbations. They visualised flow structures such as three dimensional waves, low speed streaks, mushroom structures and hairpin vortices in the flow. They found that the three dimensional wave initially formed secondary instabilities which then leads to flow transition and turbulence further downstream. This flow transition is shown in Fig. 1.19.

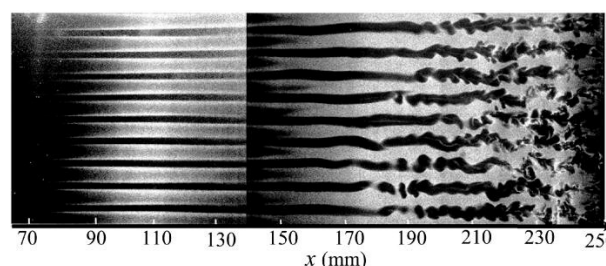


Figure 1.19: Formation of streaks and subsequent breakdown to turbulence in Rayleigh scattering experiment 2021 [47]

Though visualisation experiments give a qualitative understanding of the formation of Gortler vortices,

to develop a full understanding of this instability quantitative measurements are required. Tani [48] in 1962 was the first to perform these quantitative experiments. He used a pitot tube to analyse Gortler vortices in an incompressible flow on a concave surface. The experiments were performed at subsonic speeds and tested on both laminar and turbulent boundary layer. The fluctuations of velocity and span-wise wavelengths obtained from the experiments corroborated the previous theory that had been developed on this instability.

Further improvements were made in this field by using hot wire anemometer setups that can provide better accuracy for both subsonic and supersonic flows.

Mitsudharmadi et al 2005 [49] performed hot wire experiments on a concave surface at subsonic speeds using free-stream perturbations. They were able to confirm the presence of the sinuous and varicose secondary instabilities in the flow. They stated that the presence of inflectional velocity profiles in the boundary layer marked the onset of the secondary instability. This inflectional profile is shown in Fig. 1.20 in comparison to the undeformed Blasius boundary layer.

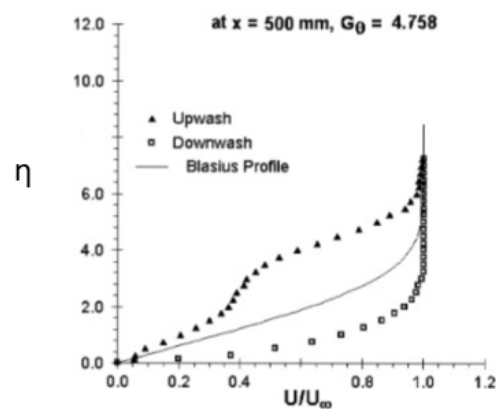


Figure 1.20: Inflectional velocity profiles generated due to up-wash regions 2005 [49]

It was seen that the formation of mushroom like structures indicate the formation of the secondary instability.

### Numerical Studies

As computer technology progressed and newer more accurate numerical methods were developed, research on numerical simulations of Gortler vortices increased. Numerical simulations for Gortler vortices have been restricted mostly to direct numerical simulations (DNS) studies where the Navier Stokes (NS) equations are solved without the use of any turbulence model. This is because Gortler instability can lead to flow transition and subsequent turbulence, and only DNS can capture these lower scales. Since all the scales present in the flow are resolved, the DNS provides the best description of the fluid flow. However, this comes at extremely high computational costs which restricts this type of study to relatively simple geometries. It is also restricted to relatively low Reynolds numbers since the range of scales to be resolved grows with  $O(Re^{0.75})$ .

Different methods have been used for the perturbation of the boundary layer to trigger the Gortler vortices. They include perturbation by adding roughness elements to the surface by Mendez et al 2018 [50], Schrader et al 2011 [51], freestream turbulence Ducoin et al 2016 [52] and free stream vortical structures Schrader et al 2011 [51]. Like the experiments, the roughness elements produce steady vortices while the other perturbation methods produce unsteady vortices.

Two types of DNS studies have been used in literature, temporal DNS and spatial DNS. The temporal DNS employs a locally parallel approximation that evolves the flow in time. Temporal DNS has been found to be ineffective in predicting the spatial evolving nature of the Gortler instability. This was seen in the temporal DNS studies of Liu and Domaradski 1993 [53] where they did not find their results comparable to experimental studies.

The first spatial DNS was performed by Schrader et al 2011 [51] on a concave surface using roughness elements and freestream inlet turbulence to trigger the instability. They found that all three perturbations were successful in generating high amplitude Gortler vortices. The freestream turbulence that contains a number of wavelengths is seen to trigger the single wavelength that is the most unstable wavelength. However the Gortler vortices formed are seen to be asymmetrical due to the superimposition of multiple wavelengths with more stability. Further research on DNS using roughness elements was also performed by Mendez et al 2018 [50] who completely resolved the laminar to turbulent transition that occurred due to Gortler vortices of a fixed span-wise wavelength. The linear and non-linear growth regions of the flow were also identified. They also found that using roughness elements of larger amplitude caused the transition area to move upstream. The fixed wavelength Gortler vortices at  $G=12$  are shown in Fig. 1.22.

Free-stream turbulence was also investigated by several authors as perturbations after Schrader's initial work. Sharma and Ducoin 2018 [54] investigated the Gortler instability by adding random freestream turbulence to the flow. They used free-stream turbulence intensities of 1% and 0.1%. It was found that the turbulence intensity at the inlet of the concave surface affects the downstream distance of flow transition. For a higher turbulence intensity of 1% the transition occurs closer to the inlet. Fig. 1.21 shows the comparison of transition for the two stream-wise velocities. Ducoin et al 2017 [55] studied the effect of inlet turbulence on concave surfaces in Savonius turbine blades. They found that Gortler vortices are also triggered on turbine blades, a factor that hadn't been previously taken into consideration when analysing blade performance. As Gortler vortices of several wavelengths are triggered due to the random turbulence, the competing wavelengths at low  $Re$  can cause the flow to maintain its laminar nature as mushroom structures before transition.

The DNS simulations give a lot of information of the flow transition and vortex formation, however as stated before their application is restricted to simpler geometries. Alternative methods such as Unsteady Reynolds Averaged Navier Stokes (URANS) were seen to give Coefficient of friction ( $C_f$ ) values 50% less than the DNS by Ducoin et al 2017 [55] and hence were deemed as inaccurate for the Gortler flow.

Large eddy simulations have been seen as a computationally cheaper method to study the Gortler vortices. Research has been performed on more complex geometries using LES. Lopes et al 2006 [56] studied a turbulent flow through an S-shaped duct using LES. They found that the concave surfaces were more susceptible to the formation of Gortler vortices than convex. The Gortler vortices were resolved by taking an average of the stream-wise velocity and streaks were seen to form on the concave wall. The vortices were seen to affect the Reynolds stress and turbulent kinetic energy production in the duct.

Tseng and Ferziger 2004 [57] performed an LES of a turbulent flow over a wavy surface. On performing a steady flow analysis they found that the flow forms Gortler vortices by periodic vortex connection and separation process.

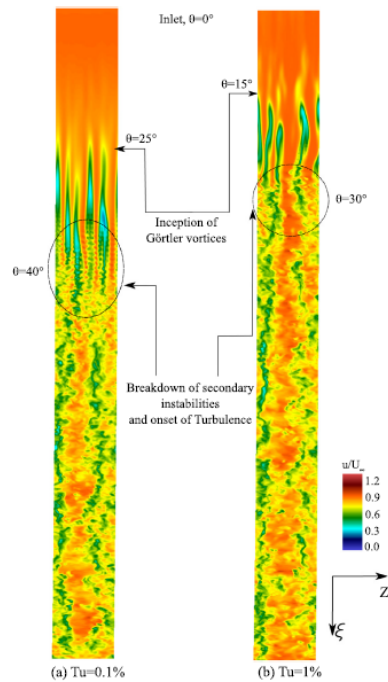


Figure 1.21: Non-dimensional Stream-wise Velocity contours on a XZ plane showing the formation of streaks and transition to Turbulence 2018 [54]

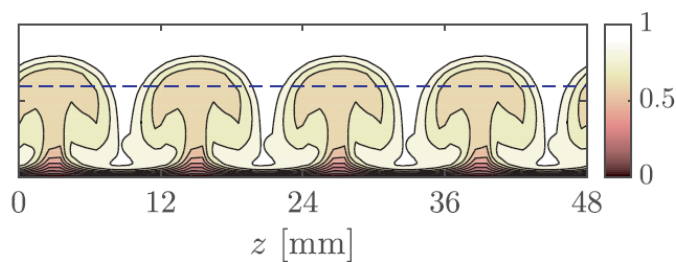


Figure 1.22: Non-dimensional Stream-wise Velocity contours on a XZ plane showing the formation of streaks and transition to Turbulence 2018 [50]

#### 1.2.4. Literature Summary

From the literature review discussed above, it is clear that most research on contraction design is focused on the optimisation of 2D, 3D and axisymmetric contractions. Most research on laminar flows in contractions focuses on the risk of boundary layer separation since it can be a leading cause for unsteadiness of the flow. Flow uniformity and boundary layer thickness are also parameters that need to be minimised at the outlet of the contraction. It is seen that the wall shape plays a crucial role in determining the values of these parameters. Different wall shapes have been used in literature like cubic polynomial, fifth order polynomial and sixth order polynomials. Higher order polynomial wall shapes are seen to have a better performance for flow separation and outlet  $Re_{\delta_1}$ . It is also seen that the inflection point of the wall shape has a big effect on the overall performance of the wall shape. However no contraction design studies performed on 1D contractions are found in the literature review. Most research focuses on performing a simple quantitative comparison of different wall shapes, however there only a few papers that perform a full optimisation of the wall shape performance. Also no optimisation study has been found that find the best performing inflection point value of the widely used fifth order polynomial wall shape, which defines the scope of this thesis.

Literature on Gortler vortices is divided into linear stability analysis, experimental and numerical analy-

sis. In linear stability analysis it was found that all the initial literature was identifying the critical Gortler number by plotting neutral stability curves. However it was seen in later research that as receptivity and initial disturbance type plays a large role in determining the stability, no critical Gortler number could be found. Experimental studies have been focused on visualisation methods and probing methods. While visualisation methods give a very good understanding of the qualitative growth of the, probe methods like pitot tubes and hot wire experiments give quantitative details that are seen to agree with the theoretical results. Most numerical studies performed on Gortler vortices are DNS with a few LES for more complex geometries. The DNS studies use various receptivity mechanisms such as wall roughness elements or freestream turbulence. All of these methods were seen to be successful in triggering Gortler vortices. However most of the research is focused on purely concave walls with constant wall curvature and there is no literature found on analysing the effect of Gortler vortices on the walls of wind tunnel contraction for the use in instability experiments where a concave wall is followed by a convex wall. Also, since the formation of Gortler vortices is highly dependent on the curvature of the streamlines in the stream-wise direction, the novel 1D contraction is expected to have a unique behaviour to instabilities, which defines the scope of the thesis.

### 1.3. Thesis Objectives

This thesis has two main research objectives that are detailed below.

#### 1.3.1. Research Objective 1

**Optimise geometry of novel 1D contraction to minimise the risk of secondary flows.**

Three important parameters will be optimised in this study, the contraction length, the length of the settling chamber and the shape of the contraction wall curve. An optimum contraction and settling chamber length will be found using results from steady state simulations. Methods from Bell and Mehta 1988 [13] and Watmuff 1986 [26] will be implemented where the lengths will be varied to ensure minimum separation, minimum boundary layer thickness and a solution independent of boundaries. Fifth and sixth order polynomial wall shapes will be simulated and the curve with most optimal inflection point distance will be chosen by performing a multi-objective optimisation procedure of flow parameters.

#### 1.3.2. Research Objective 2

**Analyse the the formation of Gortler instabilities in the 1D contraction and their stability and effect on the bottom boundary layer.**

To analyse the formation of Gortler vortices on the top boundary layer, perturbations will be added to the mean flow upstream of the contraction inlet similar to experimental studies by Peer Hossaini 1988 [58] and DNS studies by Mendez et al 2018 [39] and Schrader et al [51] using Ansys Fluent. The formation of Gortler vortices will be analysed for different span-wise wavenumbers to identify the most unstable wavenumber. The effects of the Gortler vortices on wall shear will also be analysed to find correlation with visualisation experiments such as Huang 2021 [59]. The stability of these vortices and their influence on the bottom boundary layer will be analysed.

### 1.4. Scope of Study and Chapter Overview

The scope of this thesis study is limited to the optimisation and perturbation analysis of incompressible constant property flows through the proposed novel 1D contraction geometry to understand its suitability for boundary layer measurement experiments. Heat transfer effect and buoyancy effects will not be

included in the study as they do not apply to the practical problem studied and have negligible effect on the simulation. An overview of the chapters in this report is presented below.

- **Chapter 2** details the geometry, governing equations and computational methodology used to run the different steady and unsteady simulations performed in this study. The chapter ends with a summary of all the simulations performed along with the domain used, boundary conditions and mesh type.
- **Chapter 3** discusses the results obtained from steady state simulations on the 1D contraction. Optimum lengths of the settling chamber and contraction are found and a multi-objective method to optimise a transformed fifth order wall shape to find the best performing inflection point is described.
- **Chapter 4** discusses the unsteady simulations performed on the 1D contraction. Simulations without and with perturbations are detailed and the formation of Gortler vortices and their evolution through the contraction are discussed.
- **Chapter 5** gives a conclusion of the methodology and results obtained in the previous chapter. It ends with recommendations for future research on this topic.



# 2

## Methodology

For this study an optimisation of the shape of a 1D wind tunnel contraction is performed. The optimisation is done by utilising data parameters obtained by running steady state simulations on a few selected curves from the family of curves of wall contours. The contraction length, upstream channel length and contraction shape are optimised using this procedure. After the shape is selected, this wall shape is numerically tested for the formation of curvature induced instabilities called Gortler vortices. Both unsteady laminar viscous perturbation analysis and Large Eddy Simulations (LES) are performed in the contraction to see if the the vortices formed on the top wall of the contraction affect the boundary layer on the bottom wall where heat transfer measurements are to be taken. All the simulations are performed by using the commercial CFD solver Ansys Fluent 2019 R3. The numerical methodology used for both the unsteady and steady state simulations is described in this chapter.

In this chapter the geometry and computational domain, meshing methodology, boundary conditions, governing equations and computational methodology are described for the steady state simulations (used for shape optimisation) and unsteady simulations (for Gortler vortices).

### 2.1. Physical Domain and Geometry

The geometry to be optimised is based on an experimental setup currently being built for heat transfer boundary layer measurement to understand the hydrodynamic instabilities of SCO<sub>2</sub>. Since high pressure systems are under size and safety restrictions, a flat plate cannot be used to act as a leading edge to form a developing boundary layer. The measurements are thus taken on the developing wall boundary layers of the test section . Hence, the history of the flow in previous sections like the contraction have a large influence on the measurements to be performed.

Further, the geometry proposed for this experimental setup is a novel one-dimensional wind tunnel contraction in which the only contracted dimension is the y-direction size. This ensures that there is no possibility of instabilities being induced due to curvature on the bottom surface, as it can now be made completely flat. The wind tunnel contraction, settling chamber and test section are shown together in Fig. 2.1.

In the present study, steady and unsteady simulations will be performed on the contraction geometry. Results from the steady state simulations will be used for optimisation of the contraction shape, while results from unsteady simulations will be used to analyse formation of Gortler vortices. The different simulations performed are summarised below.

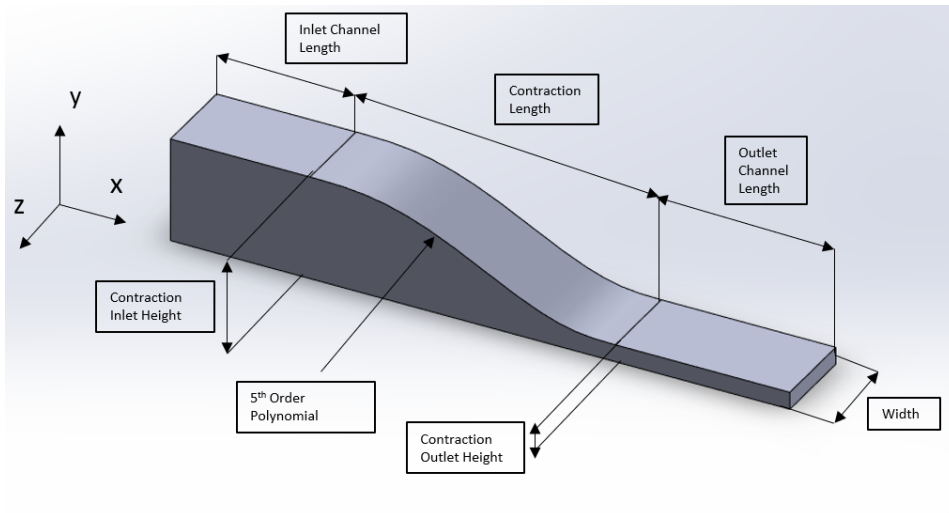


Figure 2.1: 1-D contraction Geometry

### List of Simulations Performed

1. Steady State Laminar Viscous Simulation.
2. Unsteady Laminar Simulation with Sinusoidal Perturbation (Excluding Side Walls).
3. Unsteady Laminar Simulation with Sinusoidal Perturbation (Including Side Walls).
4. Large Eddy Simulation with Random Inlet Turbulent perturbations.

Additionally, an unsteady simulation will be performed without adding perturbations will be performed to support the findings of experimental results like Boiko et al 2010 [60], which show that external forced perturbations are required to produce symmetric Gortler vortices. This is detailed in subsection 2.3.1.

In the geometry shown in Fig. 2.1, practical considerations have been made to fix the size of some of the dimensions involved in the construction. One important factor to be considered is that the total volume of the geometry cannot exceed a total of 1000cc (1 litre) due to safety considerations arising from the very high pressures involved in supercritical CO<sub>2</sub> (>73.8bar). This adds additional constraints to the size of the setup. The dimensions that have been fixed for this optimisation are indicated in tabular form in Table 2.1

Table 2.1: Fixed Dimensions in Optimisation

Fixed Dimension	Size
Test Section Length $L_t$	100 mm
Contraction Inlet Height $H_i$	60 mm
Contraction Outlet Height $H_o$	10 mm
Width of Setup $W$	50 mm

The remaining dimensions and shape that are varied and optimised in the present study include the settling chamber length, the contraction length and the wall shape contour of the contraction. These are detailed in section 2.2.

## 2.2. Steady State Analysis

Steady state simulations will be performed on the 3D geometry in which the following three dimensions are varied.

### 2.2.1. Settling Chamber Length

The settling chamber to the contraction, also known as the settling chamber, is present upstream of the contraction. The settling chamber houses various turbulence reducing devices such as screens and honeycombs. Hence it needs to be long enough for the solution to be physically accurate. It also should be long enough so that the solution is independent of the inlet boundary conditions. The boundary condition interference is qualitatively identified by looking at the pressure contours near the inlet.

However if the settling chamber is too long, it increases the boundary layer thickness at the inlet of the contraction and also increases the size of the computational domain. Hence, an optimum length must be found to satisfy all these considerations. Watmuff's 1986 [26] method of identifying the extent of upstream non-uniformity effects will be used to find this optimum value.

### 2.2.2. Contraction Length

The length of the contraction also needs to be minimised for reducing space occupied and minimise boundary layer thickness at contraction outlet. However when the contraction length is decreased, adverse pressure gradients at the inlet and outlet also increase, which leads to higher risk of boundary layer separation as shown by Morel 1975 [11] and Bell and Mehta 1988 [13]. Hence, an optimum length of the contraction needs to be found at which the risk of separation is minimised.

To find this length, the contraction length is varied keeping all other dimensions constant and parameters at design conditions. The contraction length is gradually increased to determine the critical length beyond which no flow reversals are seen. The wall shear stress in the x-direction is used to quantitatively identify any spots of flow reversal within the contraction. A value of x wall shear stress less than zero is identified to be a region of flow reversal.

### 2.2.3. Contraction Wall Shape

Higher order polynomial wall shapes will be analysed as they have been found to have a better performance as seen in research by Bell and Mehta 1988 [13]. Two main families of curves will be simulated namely, the fifth order polynomial and sixth order polynomial functions.

An optimal contraction wall shape contour will be found by using the Brassard transformation 2005 [15] of the fifth order Bell and Mehta polynomial 1988 [13]. In this transformed polynomial, the inflection point distance from contraction inlet can be varied by changing the value of a control parameter "f". By varying f a whole family of curves can be generated all having different inflection point values. An optimum value of this parameter f will be found using a multi-objective function optimisation technique. The data needed for this optimisation is also generated by running steady state laminar viscous simulations. The wall height h from the x-axis of the transformed fifth order polynomial as a function of non-dimensional x-distance  $\xi$  and parameter f is given by equation 2.3.

$$h = \left[ -\eta \left[ 1 - \left( \frac{H_o}{H_i} \right)^{\frac{1}{f}} \right] + 1 \right]^f \quad (2.1)$$

Where  $\eta$  is given by:

$$\eta = 10\xi^5 - 15\xi^4 + 6\xi^3 \quad (2.2)$$

The details of this optimisation are further explained in section 2.2.5.

The 6th order Sargison wall shape 2004 [17] was found to under-perform in comparison to the 5th order Bell and Mehta polynomial in preliminary results, hence it was not pursued further for unsteady analysis. The results have been documented in Appendix B.

Further, unsteady perturbed flow analysis will be done on this optimised contraction shape to study the evolution of Gortler vortices. This analysis will have two approaches: a laminar viscous model with sinusoidal perturbations and a Large Eddy Simulation (LES) with a specified inlet isotropic turbulence level. These methods are further detailed in section 2.3

## 2.2.4. Flow Parameters Analysed to Find Wall Shape Performance

To estimate how well a wall shape performs in a simulation, various flow parameters will be analysed. Four flow parameters will be discussed in this study, the the critical boundary layer Reynold's number at the contraction inlet, the non-uniformity at the outlet, the pressure gradient at the outlet of the contraction and the Boundary layer Reynolds number at the outlet. All the values calculated will be at the centre-line of the contraction. A brief description of these parameters is given below.

1. **Critical Boundary Layer Reynold's ( $Re_{\delta_{1cr}}$ ) at Inlet:** Boundary layer separation in the contraction occurs due to the presence of adverse pressure gradients. From Bell and Mehta's 1988 [13] study on low speed wind tunnel contractions it is seen that the risk of separation depends on the magnitude of adverse pressure gradients formed and the boundary layer thickness. Hence the boundary layer thickness at the inlet of the contraction plays a crucial role in determining the risk of flow separation at inlet. As varying the Reynold's number changes the boundary layer thickness at the inlet, it can be used as a method to gauge the risk of separation. Above a certain value of critical boundary layer Reynold's number, flow reversal occurs and the contraction is no longer suitable for experiments. The critical Reynold's number can be found by varying either the fluid properties or the mass flow through the contraction. In this study the mass flow will be varied as it is much simpler to perform. In this way critical Reynolds's values will be found for different wall shapes.

The boundary layer Reynolds number considering displacement thickness  $\delta_1$  is given by,

$$Re_{\delta_1} = \frac{\rho u \delta_1}{\mu} \quad (2.3)$$

Where,

$$\delta_1 = \int_0^{H_i} \left(1 - \frac{u}{U_b}\right) dx \quad (2.4)$$

The bulk velocity  $U_b$  is defined as,

$$U_b = \frac{1}{H_i} \int_0^{H_i} u dy \quad (2.5)$$

2. **Flow Non-Uniformity at Outlet:** The flow non-uniformity at the outlet of the channel will also be determined to analyse contraction performance. Researchers such as Morel 1975 [11] and Fang et al 2001 [25] used the velocity profile deviation from channel flow to quantify the non-uniformity at the outlet. However the presence of boundary layers that grow downstream of the contraction makes it more complex to quantify the decrease of non-uniformity downstream of the channel. An alternative method of using the vertical pressure profile will be used in this study which does away with the need to quantify the non-uniformity of boundary layers. A standard deviation of the pressure profile will be used to quantify the non-uniformity.

The standard deviation is given by:

$$\sigma_p = \sqrt{\frac{\sum_{i=1}^N (P_i - P_{avg})^2}{N}} \quad (2.6)$$

Where N is the number of data points on the vertical line. A relation between  $\sigma_p$  and parameter  $f$  will then be found for the optimisation.

As the non-uniformity depends on the curvature of the contraction at the outlet, non-uniformity values will be found for different wall shapes.

3. **Adverse Pressure Gradients at Outlet:** As the outlet of the contraction also has a risk of boundary layer separation as shown by Bell and Mehta 1988 [13], the value of adverse pressure gradients at the outlet will be calculated for different wall shapes. This will be done by calculating the pressure gradient  $dp/dx$  along the wall at the outlet and identifying the regions where  $dp/dx > 0$ .
4. **Boundary Layer Reynolds's number Outlet:** The boundary layer Reynold's number at the outlet is the last parameter that will be calculated. Bell and Mehta 1988 [13] optimised a low speed contraction to have a minimum  $Re_{\delta_{1out}}$ . This will also be calculated using displacement thickness similar to the critical Reynold's at the inlet.  $Re_{\delta_{1out}}$  will then be found for all different curves to be simulated.

### 2.2.5. Optimisation Method

The optimisation is performed for the two objective functions using a multi-objective optimisation method in the 5 steps shown below.

1. Data will be extracted from steady state laminar simulations performed on the different contraction shapes. Four different parameters will be analysed to gauge the performance of the contraction as described in section 2.2.4. Their values as a function of Brassard parameter  $f$  will be plotted.
2. Next, to include only competing parameters into the contraction, two of the most important parameters will be chosen out of the four parameters. Using MATLAB's curve fitting software the two selected parameters will curve fit.
3. Since we have one input parameter that we need to optimise and two output parameters that need to be minimised, a Multi-objective/Pareto optimisation technique will be used to find the optimal  $f$  value. A scalarization based multi-objective technique will be used called the weighted sum method. A brief description of the method is given below.

### Weighted Sum method

In this method both the objective functions (say  $F_1$  and  $F_2$ ) will be aggregated to form one single objective function( say  $F$ ) that needs to be minimised, with two weights that add up to 1 (say  $w_1$  and  $w_2$ ). Additional constraints are also put on the bounds of  $f$ ,  $w_1$  and  $w_2$ .

$$\text{Minimise } - - - F = w_1F_1(f) + w_2F_2(f) \quad (2.7)$$

Subject to,

$$w_1 + w_2 = 1 \quad (2.8)$$

$$0 \leq w_1 \leq 1 \quad (2.9)$$

$$0 \leq w_2 \leq 1 \quad (2.10)$$

$$0.5 \leq f \leq 1.5 \quad (2.11)$$

4. Once the Pareto front is generated, the most optimal point will be chosen to be that Pareto point that is closest in distance to the to the ideal minimum point which is at the origin.
5. The value of parameter  $f$  at this minimum point will then be chosen as the optimum transformed fifth order polynomial for the wall shape of the experimental setup.

## 2.3. Unsteady Analysis

Unsteady simulations are performed on the computational domains to understand if they have steady state solutions on adding perturbations. Reference simulations will be performed without perturbations to understand the steady state solutions of the system.

### 2.3.1. No Perturbations

An unsteady simulation is performed without any added perturbations to the flow field at the inlet. This simulation is performed for two main reasons:

- To assess whether the unsteady simulation converges to the steady state solution given sufficient computational time.
- To act as a reference state flow field to compare results with perturbed simulations performed as detailed in subsection 2.3.2

To check for convergence to steady state, several parameters of the flow such as contraction outlet velocity profiles, contraction outlet uniformity and contraction inlet boundary Reynold's numbers will be compared.

### 2.3.2. Perturbations Introduced to Flow Field

To analyse the flows stability in the curved contraction section, perturbations will be added through the inlet boundary conditions detailed in section 2.4.

Two different perturbation methods will be used for the simulations in this study. For the laminar viscous simulation, sinusoidal perturbations will be introduced to the velocity inlet on the top wall in the negative  $y$ -direction. This is done because to trigger Gortler vortices it is seen that perturbations need to be in the radial direction of the wall curvature as shown in Mendez et al 2020 [39]. Further, these

sinusoidal perturbations are given wavelengths in the span-wise direction since experimental results like Boiko et al 2010 [60] show that such perturbations are successful in triggering the Gortler instability. The perturbation equation is shown in equation 2.12.

$$U_{perturbation} = 0.001\sin(\omega z) \quad (2.12)$$

The value of angular frequency  $\omega$  will be varied to generate perturbations of different wave-numbers in the top boundary layer. The second perturbation method that will be used to trigger Görtler vortices will be random isotropic turbulence at the inlet of the contraction. These turbulence are specified as a percentage of the mean velocity of the flow. This perturbation method has been seen to trigger Görtler vortices in DNS studies such as Schrader et 2011 [51].

## 2.4. Boundary Conditions and Computational Domain

Boundary value problems involve the solving of differential equations on a closed finite domain along with added constraints which are prescribed on the edge of the domain called the boundary curve. Since CFD simulations generally involve solving governing equations on a finite computational domain, they are inherently boundary value problems. These boundary conditions can be defined in several different ways depending on the geometry, flow and physics of the given problem.

### 2.4.1. Boundary Conditions

The boundary conditions used in the simulations performed in the present study are briefly described below.

- **Pressure inlet and outlet:** A pressure inlet or outlet is specified depending on the simulation performed. The pressure at the boundary is specified as a gauge pressure of  $P_g=0$  for all the simulations carried out in this study. The condition specifies a constant pressure at that boundary surface and the Bernoulli equation is then used to calculate the velocity components on that surface.

For the LES, to analyse the formation of instabilities in the contraction due to turbulence in the boundary layer, an isotropic random turbulence level is specified at the pressure inlet as discussed in section 2.3.2.

- **Mass-flow/ Velocity inlet and outlet:** The mass flow and velocity boundary conditions are used to specify the mass flow values or velocity vectors respectively at the boundary of the domain. Since the simulations in the present study are incompressible with a constant density ( $\rho = \text{constant}$ ), both the mass-flow and velocity boundary conditions are equivalent and can be used interchangeably.

For the laminar perturbed simulations, sinusoidal perturbations are prescribed through the velocity inlet in the wall normal direction -y direction. The perturbations are prescribed as specified in section 2.3.2. The mass-flow rate, velocity and properties of SCO<sub>2</sub> are shown in Table. 2.2.

- **Symmetry Boundary Condition:** The symmetry boundary condition is a boundary condition used to mirror symmetrical computational domains. The surface selected for the symmetry defines the plane about which the domain is mirrored. Using a symmetry boundary condition helps in greatly decreasing the total computational time and memory required for a CFD simulation.

For the geometry in this study for simulation 1 and simulation 3, a central YZ plane at  $x=25\text{mm}$  is taken to be the symmetry plane. However one constraint of using this boundary condition is that there should be no flow variable fluxes across this plane from one half of the domain to the other.

Table 2.2: System parameters at Design Conditions

Parameter	Value
Mass Flow Rate $\dot{m}$	0.05 Kg/s
Velocity $U_{inlet}$	0.02371m/s
Density $\rho$ @ (90Mpa, 306K)	702.85kg/m <sub>3</sub>
Dynamic Viscosity $\mu$ @ (90Mpa, 306K)	56.306 $\mu$ Pa – s

- **Periodic Boundary Condition:** A periodic boundary condition is used when the flow field in the computational domain demonstrates cyclic periodic patterns. One cycle of the domain in the direction of periodicity can be simulated with periodic planes on either side as shown in Fig. 2.2. These periodic planes, unlike symmetry planes allow the variation of flow variable fluxes across the boundary.

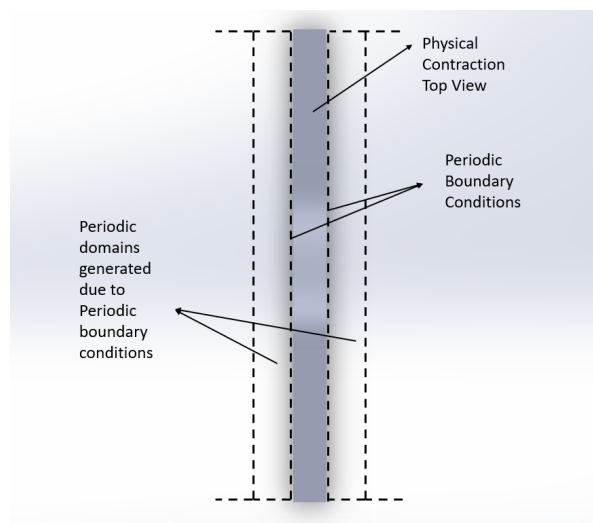


Figure 2.2: Top View Of Contraction: Periodic Boundaries on either side of Contraction

- **No Slip Boundary Condition:** The no slip condition is a boundary condition in viscous fluids that imposes a zero velocity on a wall/surface. Due to the fluids viscosity, fluid molecules close to the wall adhere to the surface. This boundary condition plays an important role in the development of boundary layers within the domain.

### 2.4.2. Computational Domain

The various boundary conditions discussed in the previous subsection are enforced on a part of the true geometric physical domain that is used for the simulation called the computational domain. The computational domain greatly reduces the size of the true domain by utilising symmetries and repeating structures inherent in the geometry. This helps in drastically reducing the memory requirements and increasing the speed of calculation.

In this study, different computational domains are used for different simulations. A summary of the type of domain used for the different simulations are performed is given in Table 2.3.

Table 2.3: Summary of Domain type for each simulation

Simulation Type	Domain Used	Shown in Figure
Steady Laminar	Domain 1	Fig. 2.3
Unsteady Laminar (No Side Wall)	Domain 2	Fig. 2.4
Unsteady Laminar (With Side Wall)	Domain 3	Fig. 2.6
Large Eddy Simulation	Domain 2	Fig. 2.4

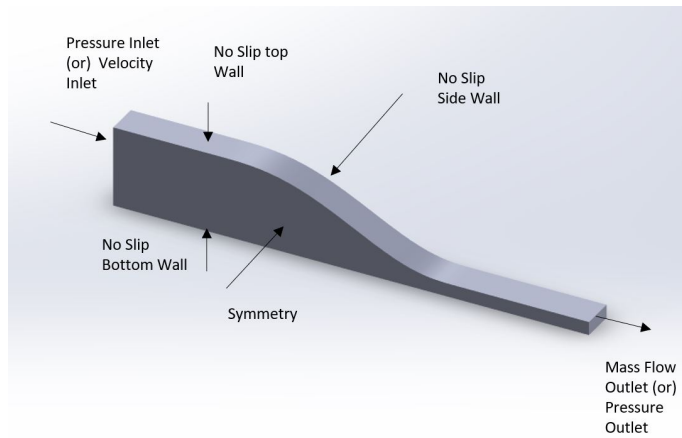


Figure 2.3: Domain-1 (25mm)

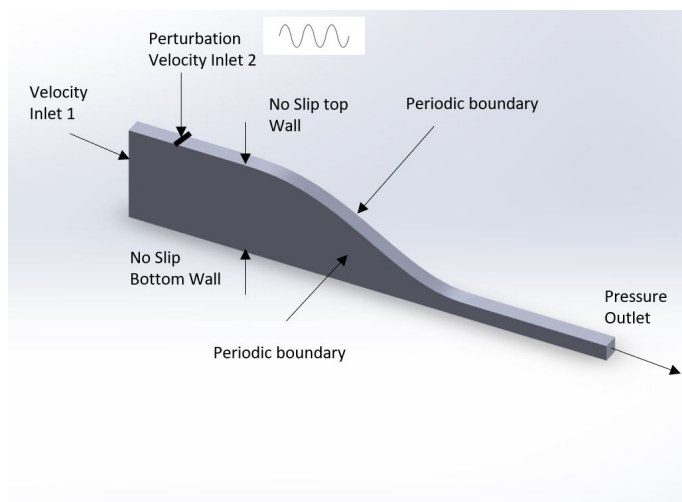


Figure 2.4: Domain-2 (12mm)

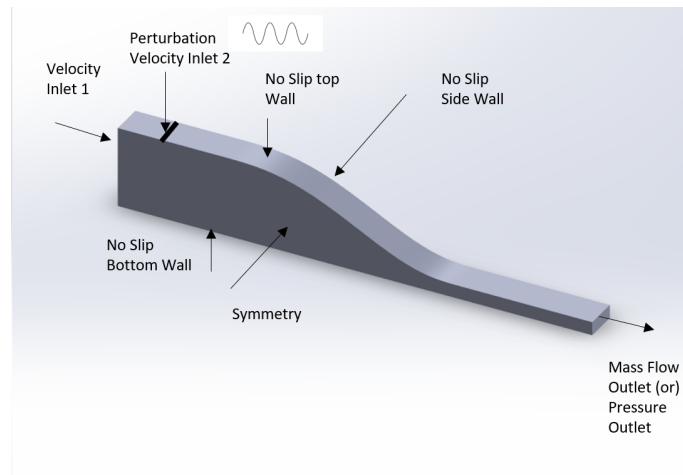


Figure 2.5: Domain-3 (25mm)

**Domain Initialisation:** For the simulations to have a faster convergence, the flow field variables need to be given a good guess for an initial value. This is done by using the hybrid initialisation method in Fluent[61]. In this method the Laplace equation is solved iteratively to generate the initial velocity and pressure values of the flow field.

Where the Laplace equation is given by :

$$\nabla^2 \phi = 0 \quad (2.13)$$

and velocity is related to the potential by

$$v = -\nabla \phi \quad (2.14)$$

The Laplace equation is solved for 10 consecutive iterations which develops an initial field that is closer to the true flow than assigning random constant values to the domain.

In the LES simulation, results from a laminar steady state simulation are used to initialise the flow field for faster convergence.

## 2.5. Computational Mesh

Mesh generation is the process of dividing a continuous geometric domain into a finite set of nodes at which important parameters and values can be calculated. The nodes approximate locally the behaviour of the flow in the domain, thereby providing an accurate representation of the total flow.

Meshes can be generated into two main types:

- **Structured Mesh** : Structured meshing is a meshing technique in which uniformity is maintained in the mesh elements shape and an implicit connectivity is created between adjacent elements. For simpler geometries structured meshes are easier to mesh, take up lesser memory and also help decrease solving time. Structured meshes also demonstrate lower false diffusion since the mesh elements are aligned in the direction of the flow[61]. However for complex geometries it is not always possible to generate a structured mesh, especially in regions of very high curvature and intricate geometry.
- **Unstructured mesh** : Unstructured meshing is a meshing technique in which mesh elements are not uniform in shape and connectivity data needs to be saved for each node to completely define the relation between adjacent nodes. Though computationally and memory wise more intensive,

unstructured meshes are suitable for very complex geometries. However they are susceptible to numerical diffusion which can lead to non-physical solutions [61].

Both structured Kao 2017 [62] and unstructured meshing Sargison 2004 [17] meshing techniques have been used in previous studies. For the computational domain in this study a fully structured mesh is generated to avoid numerical diffusion and have faster computational times. The mesh was created in the Fluent meshing software is used for the simulations of the wind tunnel contraction. An edge sizing is performed on every dimension of the geometry and the behaviour of the sizing is kept on "hard", which means the mesh conforms to the sizing specified. For domain 1 the mesh is biased in the span-wise and wall normal directions while for domain 2 it is highly biased only in the wall normal direction.

Edge sizing is varied depending on the section of the physical domain meshed. In the stream-wise direction the settling chamber, contraction and test section have 60, 300 and 60 elements respectively. In the wall normal direction 60 elements are used and the biasing of the elements depends on the simulation performed. In the span-wise direction for steady state simulations on the large domain 60 elements are used. For unsteady simulations 60 elements are used even though the domain is half the size to fully resolve any vortical structures formed.

For simulations 2,3 and 4 where perturbations are introduced, additional care is taken to maintain the wall  $y^+$  at a low value to fully capture the effects of the boundary layer development and instabilities. The wall  $y^+$  is defined in the equations below.

$$y^+ = \frac{U_\tau * y}{\nu} \quad (2.15)$$

where the friction velocity  $U_\tau$  can be written in terms of the wall shear stress and is given by:

$$U_\tau = \frac{\tau}{\rho} \quad (2.16)$$

Using these results, the first cell length  $y$  can be calculated by taking an appropriate  $y^+$  value depending on the simulation performed. For simulations 2 and 3 where a laminar viscous simulations is performed with sinusoidal perturbations, a  $y^+$  of around 10 is used. For simulation 4 where an LES is performed using inlet turbulence levels, a  $y^+$  of around 1 is maintained.

Examples of the meshes generated using the above methods are shown in Fig. 2.6 and Fig. 2.7. The final meshes used for the simulations are generated after a mesh independence study which is added in Appendix A.

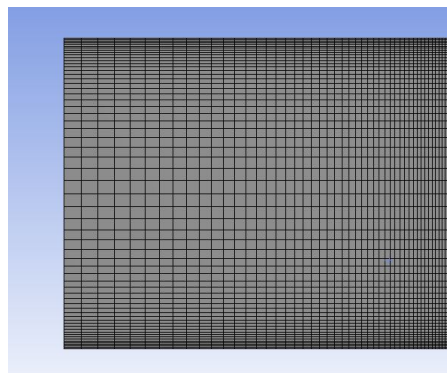


Figure 2.6: Side-View-Shows Bias in Wall Normal and stream-wise direction

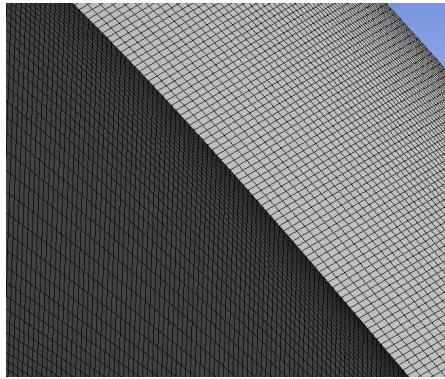


Figure 2.7: Isometric View of Contraction

## 2.6. Governing Equations: Incompressible Navier Stokes Equations

The governing equations of fluid flow are known as the Navier Stokes (NS). These are a set of partial differential equations that mathematically describe the flow of viscous Newtonian fluids. They are fundamental expressions of conservation of mass and momentum for a fluid and include terms for rate of change, advection, viscous forces, pressure gradients and body forces. For fluid flow at low Mach numbers ( $Ma < 0.3$ ) compressibility effects can be neglected and the NS equations in three dimensions can be written in their incompressible form in Einstein notation as follows.

$$\frac{\partial u_i}{\partial x_i} = 0 \quad (2.17)$$

$$\rho \left( \frac{\partial u_i}{\partial t} + \frac{\partial u_i u_j}{\partial x_j} \right) = -\frac{\partial p}{\partial x_i} + \mu \frac{\partial^2 u_i}{\partial^2 x_j} + \rho g_i \quad (2.18)$$

Here the density  $\rho$  and viscosity  $\mu$  are taken to be constants.

For the steady state laminar viscous solver where the flow variables are considered to be independent of time, the time derivative term in the NS equations vanishes.

In this study, the energy equation is not solved as there is no heat exchange in the domain.

### 2.6.1. Numerical Techniques

In this subsection the numerical methods used to solve the governing equations will be discussed.

#### Discretisation Technique: Finite Volume Method

The finite volume method (FVM) is a technique of solving systems of partial differential equations by integrating over cell volumes to convert the equations into a system of linear algebraic equations. It is a highly versatile method and can be used to solve the governing equations over any mesh shape. In Ansys Fluent the different flow variables are stored at the centroid of the cells. The flow variables are then assumed to vary linearly across the volume of the cell. Each term is integrated individually to form a matrix set of linear algebraic equations which are then solved iteratively for the pressure and velocity field.

### Solver and Pressure velocity coupling

Since the flow is incompressible and fluid densities are taken as a constant in this study, a pressure based solver is used. A coupled approach is used to solve the equations in which equations 2.1-2.4 are solved simultaneously after rewriting the continuity equation in the form of a Poisson equation for finding the pressure field.

The coupling used for the simulations is the SIMPLEC pressure velocity coupling method. The SIMPLEC method was chosen as it is seen to perform well for incompressible flows and has a slight computational time advantage to the SIMPLE algorithm 1984 [63].

### Spatial discretisation

For finding gradients the least square cell based method is used which is computationally less expensive than other methods with similar accuracy as the Green-Gauss node based method. For momentum and pressure discretisation, a second order upwind scheme is used as it has lower false diffusion and higher accuracy than first order schemes[61].

### Temporal discretisation

For the discretisation of the unsteady term in the NS equations a second order implicit time scheme is used for higher accuracy. For Simulation 4 where an LES is performed and the smaller scales are resolved by using a turbulence model a bounded second order implicit solver is used. This is because bounding the flow variables can lead to better convergence and a lower risk of unwanted oscillations in the flow while modelling the smaller scales.

### Sub-grid Model (for LES)

Since large eddy simulations only resolve the larger vortices in the flow field and filter out the finer scales, a sub-grid turbulence model is required to model these scales. For this study the Wall Adaptive Local Eddy viscosity (WALE) model is used as it is seen to give good results for wall bounded [61] and transitional flows in Bertolini 2021 [64].

## 2.7. Simulation Overview

The following section gives a tabular summary of the different simulations performed , their boundary conditions and domain.

1. Steady State Laminar Simulations		
Setting	Description	Described in section
Inlet Boundary	Pressure Inlet	2.4.1 Pressure In-/Outlets
Outlet Boundary	Massflow Outlet	2.4.1 Massflow In-/Outlets
Mesh	Structured Mesh	2.5 Mesh
Domain and Side Boundaries	Domain 1, Symmetry B.C.	2.4.2 Steady Domain

Table 2.4: Steady State Laminar Simulations Details

2: Transient Laminar Simulations (Without Side Walls)		
Setting	Description	Described in section
Inlet Boundary	Massflow inlet	2.4.1 Massflow In-/Outlets
Outlet Boundary	Pressure Outlet	2.4.1 Pressure In-/Outlets
Mesh	Structured Mesh	2.5 Mesh
Domain and Side Boundaries	Domain 2, Symmetry B.C.	2.4.2 Unsteady Domain

Table 2.5: Transient Laminar Simulations (Without Side Walls) Details

3: Unsteady Laminar Simulations (With Side Walls)		
Setting	Description	Described in section
Inlet Boundary	Massflow Inlet	2.4.1 Massflow In-/Outlets
Outlet Boundary	Pressure Outlet	2.4.1 Pressure In-/Outlets
Mesh	Structured Mesh	2.5 Mesh
Domain and Side Boundaries	Domain 2, Periodic B.C.	2.4.2 Unsteady Domain

Table 2.6: Unsteady Laminar Simulations (With Side Walls) Details

4: Large Eddy Simulation		
Setting	Description	Described in section
Inlet Boundary	Massflow Inlet	2.4.1 Massflow In-/Outlets
Outlet Boundary	Pressure Outlet	2.4.1 Pressure In-/Outlets
Mesh	Structured Mesh	2.5 Mesh
Domain and Side Boundaries	Domain 2, Periodic B.C.	2.4.2 Unsteady Domain

Table 2.7: Large Eddy Simulation Details

### 2.7.1. Chapter Summary

This chapter details the computational methodology of the simulations performed. It first details the the physical domain and geometry that is to be simulated and gives a list of simulations that are performed. After this the methodology of the steady state and unsteady analysis are detailed along with the boundary conditions used. Next the computation domains used for the simulations are shown, along with the governing equations and numerical methods used to solve them. Finally a tabular summary of the different simulations is given.

# 3

## Results and Discussion- Shape Optimisation

In this chapter, the results obtained from steady state simulations that are used for optimisation of the 2D contraction shape will be presented and discussed in detail.

### 3.1. Contraction Length

Steady state simulations are performed and the contraction length is varied keeping all other dimensions constant. The un-transformed fifth order polynomial wall shape is taken for the wall contour. A mass flow rate of 0.05kg/s is maintained in the contraction which is the experimental design flow rate of the setup. A poly-line is drawn on the centreline symmetry along the wall of the entire geometry as shown in Fig. 3.1. Pressure gradients in the stream-wise direction are calculated on this poly-line as shown in Fig. 3.2.

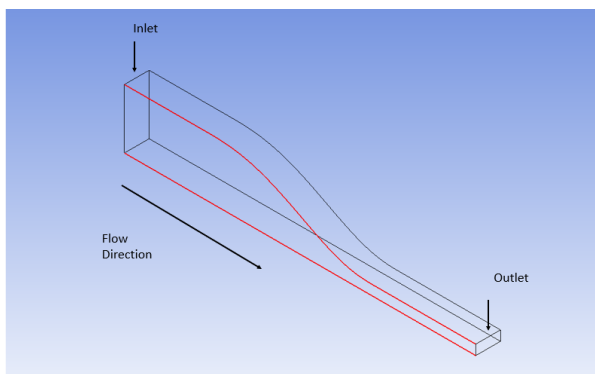


Figure 3.1: Poly-line along Centre line symmetry of Geometry - Marked in Red

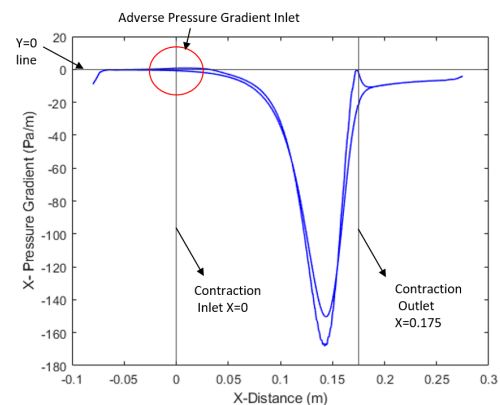


Figure 3.2: X-Distance vs X- Pressure Gradient along Poly-line

It is seen in Fig. 3.2 that there exists one distinct region of adverse pressure gradient in the contraction near the inlet. This adverse gradient is seen to occur within the contraction. Similar results are seen for 2D contractions by Morel 1975 [11] where adverse pressure gradients are formed within the contraction inlet. This is attributed to the velocity minima occurring within the contraction inlet instead of the at the inlet due to local curvature effects dominating overall flow acceleration.

The maximum of this adverse pressure gradient is found to occur at a distance of 3.5mm downstream of the inlet of the contraction. This is shown in a zoomed in view in Fig. 3.3

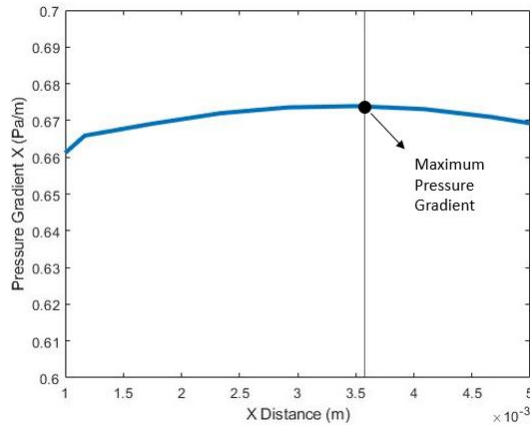


Figure 3.3: X-Distance vs X-Pressure Gradient Plot- Zoomed in View

It is seen that depending on the length of the contraction in the geometry, there might exist flow reversal zones caused by adverse pressure gradients. These regions are identified by seeing where the x-direction wall shear stress is less than zero. Results show that flow reversal due to adverse pressure gradients can either be confined only to the edge along the side wall as seen in Fig. 3.4, or can also occur on the top wall just within the contraction as shown in Fig. 3.5. Separation of flow on the concave surface has been noted by several authors such as Morel 1975 [11] and Bell and Mehta 1988 [13] and occurs due to the presence of adverse pressure gradients in the contraction. Secondary flows like flow separation due to sharp corner have also been noted in experimental studies such as Johl et al 2004 [65].

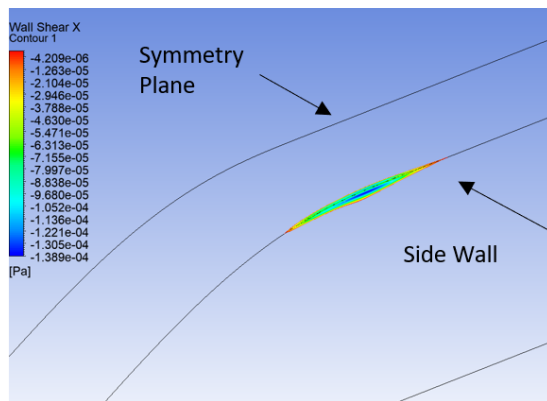


Figure 3.4: X-Wall Shear 175mm contraction

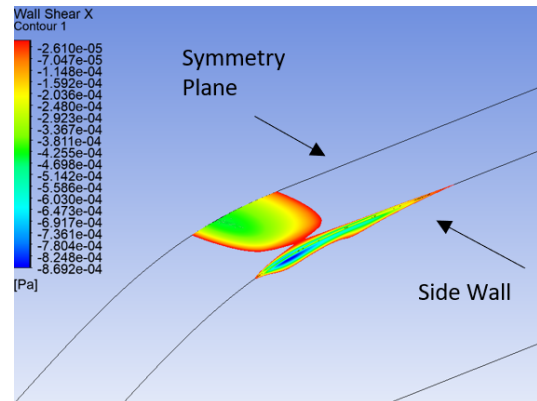


Figure 3.5: X-Wall Shear 165mm contraction

Beyond a certain length of contraction the separation region along the top wall disappears and only the reverse flow region along the edge of the side wall remains. The contraction length and the region of flow reversal are shown in tabular form in Table. 3.1.

From Table. 3.1 it is clear that there exists some maximum contraction length beyond which no reversal takes place on the top wall of the contraction inlet. This length is found to be 175mm for the current geometry. It is also interesting to note that no boundary layer separation is seen at the exit for any of the different contraction lengths simulated even though adverse pressure gradients are found at the

Table 3.1: Presence of Flow Reversal at Different Contraction Lengths

Contraction Length (mm)	Flow Reversal	
	Inlet Top Wall	Inlet Side Edge
160	Yes	Yes
160	Yes	Yes
165	Yes	Yes
170	Yes	Yes
175	No	Yes
200	No	Yes

outlet. This behaviour was also described by Bradshaw 1973 [66] who stated that convex surfaces are stabilising and hence have a lower risk of boundary layer separation than concave surfaces. Similar behaviour was found by Madhusudan et al 1994 [67] in a boundary layer study on an S- blade consisting of consecutive concave and convex sections.

The flow reversal seen in Fig. 3.5 can cause boundary layer separation and unsteadiness in the contraction which can disturb the laminar flow at the outlet and render the setup unsuitable for boundary layer experiments. Bell and Mehta's 1988 study of low speed wind tunnels [13] also concluded that there exists some optimum contraction length to prevent risk of separation at inlet. However, they also found that increasing the length over that optimum might lead to separation at the contraction outlet which would also disturb the laminar flow. This flow reversal at the outlet however was not found in any of the different contraction lengths simulated in this study.

Mehta 1979 [20] in his work on two dimensional blower tunnel design showed that for edge and cross flows in a contraction remain localised to the edge and do not disturb the flow through the centre of the contraction. Additionally the use of corner fillets to stop the merger of two different boundary layers at the edge has been shown to reduce the formation of such secondary flows in a study by Johl et al 2004 [65].

From analysing the above results, it was decided that a contraction length of 175mm would be ideal for the experimental setup since this would minimise the risk of flow reversal and boundary layer separation. This length will be used for all further simulations in the thesis study.

## 3.2. Settling Chamber Length

Steady state simulations are performed for different settling chamber lengths to find the shortest length that is unaffected by the boundary conditions. The settling chamber also needs to be large enough to house various turbulence reducing components such as the screens and honeycomb channels.

Different inlet lengths were simulated ranging from 50mm to 160mm. It was found that boundary conditions for settling chamber lengths above 60mm do not interfere with the flow simulations. This was determined by analysing the isobars connected to the contraction similar to the paper by Watmuff 1986 [26].

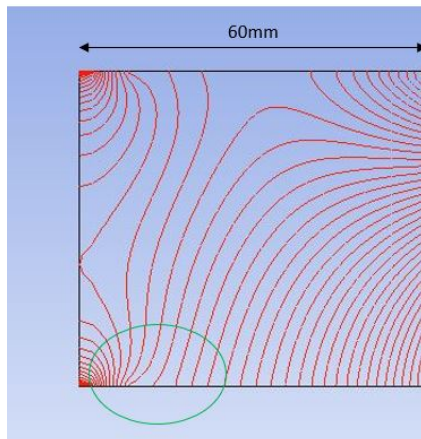


Figure 3.6: Pressure contours Inlet length 60mm

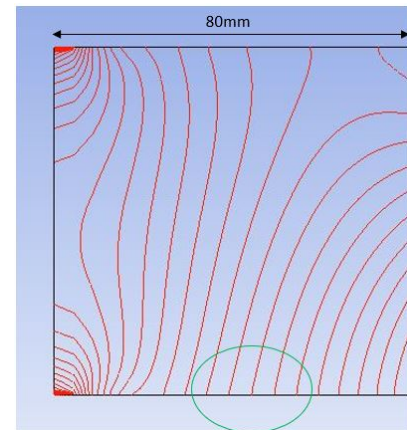


Figure 3.7: Pressure contours Inlet length 80mm

For the simulation with 60mm settling chamber length it can be seen from Fig. 3.6 that the pressure contours are disturbed by the boundary layer, hence affecting the flow field downstream. However in Fig. 3.7 for the 80mm case the isobars are not influenced by the boundary conditions.

As the experimental setup also requires having extra space for placing screens and honeycombs in the settling chamber, an settling chamber of 100mm is proposed for the experimental setup. However for further simulations, for the unsteady cases since the settling chamber length does not make a difference to the Gortler vortex analysis and to decrease computational time an settling chamber length of 80mm is used.

### 3.3. Contraction Wall Shape Optimisation

Once the contraction length and settling chamber length are fixed, the wall contour shape of the contraction is optimised. In this subsection the results obtained in optimising the Brassard transformed fifth order polynomial are shown. First the qualitative effect of changing wall shape on flow conditions is discussed, after which a multi-objective optimisation is performed to select the best performing wall shape.

#### 3.3.1. Qualitative effect of Changing Wall Shapes

**Critical Reynolds Number Boundary Layer (Inlet)** It is found that for a given wall shape, there exists

a critical value of the boundary layer Reynold's number after which flow reversals occur. This critical Reynolds ( $Re_{\delta_{1cr}}$ ) was found to be a function of the Brassard Parameter  $f$  used to generate wall shapes. The mass-flow rate through the contraction was varied to obtain a varying Reynolds's number in the boundary layer at the contraction inlet to find  $Re_{\delta_{1cr}}$ . The  $Re_{\delta_{1cr}}$  was evaluated for different pressure and temperature (physical properties) values and it was found to be independent of these properties.

The value of  $Re_{\delta_{1cr}}$  is plotted for five different parameter  $f$  values. It is seen that as the value of parameter  $f$  decreases the  $Re_{\delta_{1cr}}$  at the inlet of the contraction also decreases. These points are then curve fitted using a power function in  $f$  in the form of  $F_1 = af^b + c$ , where  $a = 478.9$ ,  $b = -2.524$ ,  $c = 471.8$  are constants that develop the best curve fit for this given data-set. The data points of  $Re_{\delta_{1cr}}$  and the curve fitted function are shown together in Fig. 3.8.

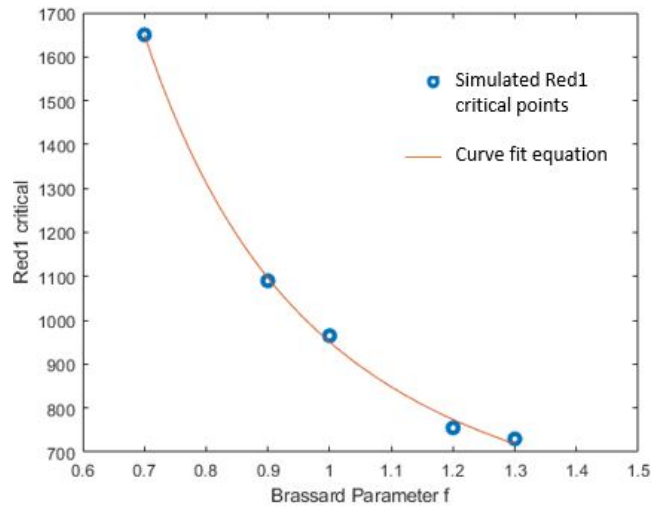


Figure 3.8: Plot Parameter  $f$  vs  $Re_{\delta_{1cr}}$

### Pressure Non-Uniformity

Another effect seen on varying the wall shape of the contraction was that the non-uniformity of the flow field at the outlet also changed. This non-uniformity is quantified by taking the standard deviation. It was found that the standard deviation ( $\sigma_p$ ) is also a function of the parameter  $f$ . As  $f$  is increased the non-uniformity at the outlet of the contraction decreases.

The values of  $\sigma_p$  is found at five distinct values of  $f$ . These values are then curve fitted using a fourth order polynomial function given by  $F = af^b + c$ , where  $a=0.008624$ ,  $b=-2.715$  and  $c=0.01352$  which is found to give a good fit. The five data points of  $\sigma_p$  along with the curve fitted function are shown in Fig. 3.9.

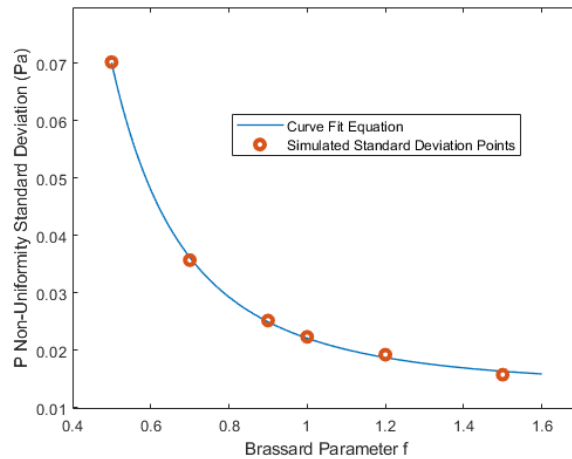


Figure 3.9: Plot Parameter  $f$  vs  $\sigma_p$

It is also seen that this non-uniformity at the contraction outlet rapidly decreases as the fluid flows downstream in the test section. This can be seen when the two pressure lines are compared as shown in Fig. 3.10 and Fig. 3.11.

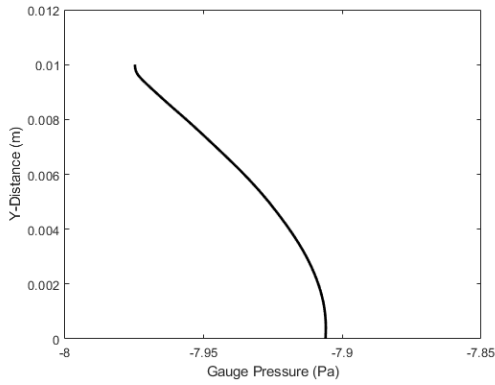


Figure 3.10: Vertical Pressure Line at Outlet X=0.175m

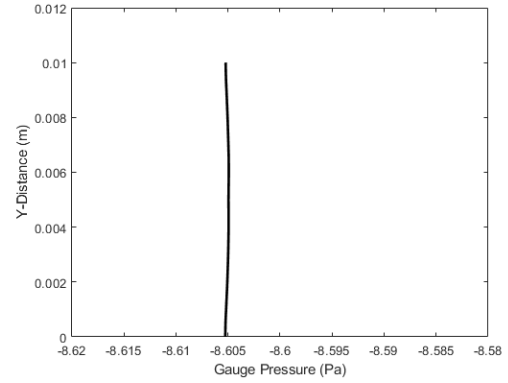
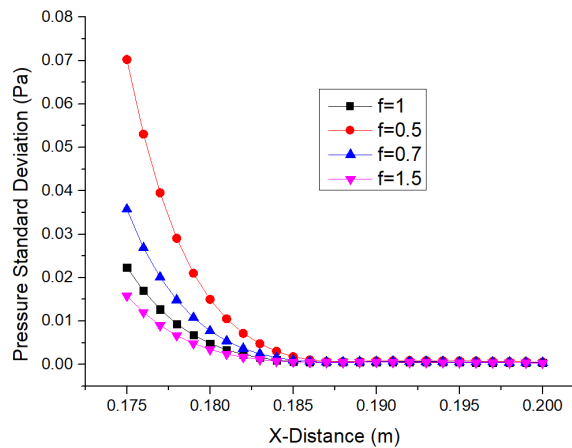


Figure 3.11: Vertical Pressure Line 75mm Downstream of Outlet X=0.25m

This property of the pressure line to increase in uniformity as the flow moves through the test section gives us a good estimate as to where the influence of the contraction ends and a uniform channel flow boundary layer develops. The value of non-uniformity through the test section for a few randomly selected values of parameter  $f$  is given in Fig. 3.13.

Figure 3.12: Plot X-distance vs Pressure Deviation  $\sigma_p$  for different  $f$  values

From Fig. 3.13 we can see that after a distance of 12mm downstream of contraction inlet, all pressure deviations collapse on each other. This decay found to be exponential in nature and a curve fit equation was found to approximate this behaviour. This equation is given below.

$$F(f, x) = (3.81 * 10^{22})e^{(-9.12f^2 + 26.24f + 301.6)x} \quad (3.1)$$

This exponential behaviour is also observed by Morel 1977 [12] where the non-uniformity plots of 10 different nozzles collapsed on each other. Morel estimated the rate of non-uniformity decay as  $\exp(-2\pi x/H_0)$ .

### Adverse Pressure Gradients Outlet

It is also seen that a change in wall shape changes the magnitude of pressure gradients at the contraction outlet. This can be seen in Fig. 3.13, where a curve with a higher  $f$  value tends to have lower pressure gradients and vice versa. This is expected since as  $f$  increases the curvature of the convex wall shape decreases.

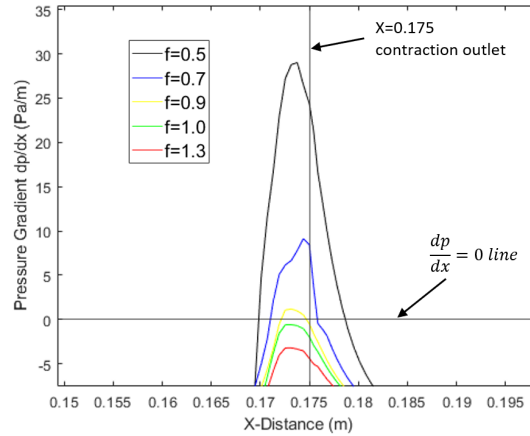


Figure 3.13: Pressure Gradients in X- Direction for Different  $f$  values

From Fig. 3.13 it is also evident that the maximum value of these gradients fall within the contraction. On average the maxima is located around 2-3mm upstream of the outlet. This behaviour is also seen in Morel’s study on 2D 1977 and axisymmetric contractions 1975 [12][11].

At the simulated mass flow rate of 0.05kg/s, it was found that only certain  $f$  values produce adverse pressure gradients. Fig. 3.14 demonstrates this trend and shows the departure from a negative to a positive pressure gradient.

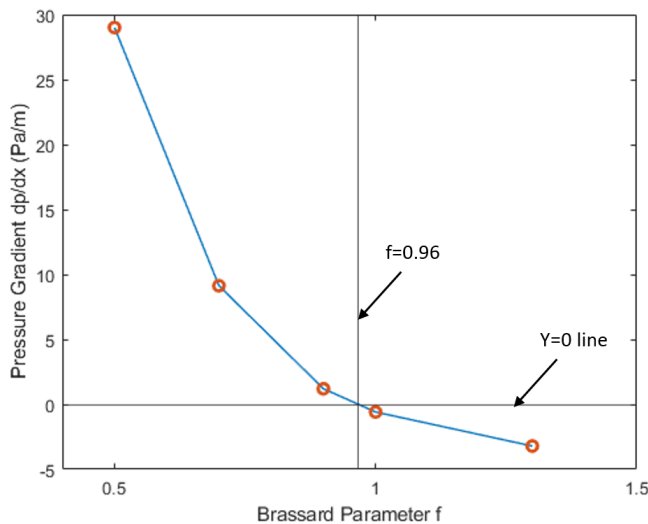


Figure 3.14: Plot Parameter  $f$  vs Maximum Pressure Gradient

### Outlet boundary layer Reynold’s number

It is seen that the Reynold’s number of the bottom plate boundary layer ( $Re_{\delta_{1out}}$ ) at the contraction outlet also varies with the parameter  $f$ . The boundary layer at the bottom is analysed as this is where

the heat transfer experiments are to be conducted. The  $Re_{\delta_{1out}}$  is evaluated 14mm downstream of the outlet since nearer to the outlet regions of decreasing boundary layers are encountered due to curvature induced non-uniformity's. The variation follows a logarithmic relation as shown in Fig. 3.15, where increasing the value of parameter  $f$  increases  $Re_{\delta_{1out}}$ .

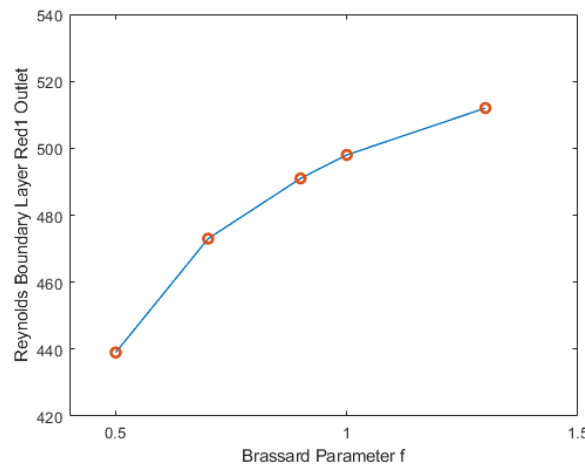


Figure 3.15: Reynolds boundary layer  $Re_{\delta_{1out}}$  Outlet

According to linear stability analysis, a flat plate boundary layer  $Re_{\delta_1}$  of 520 is the critical value required for instabilities to be triggered. It is seen that even 14mm downstream of the outlet the values of  $Re_{\delta_1}$  are less than 520. This makes it acceptable for the boundary layer experiments to be conducted in the test section.

### Choosing Parameters to Optimise

Four parameters have been discussed that are effected by changing parameter  $f$  however all the parameters are not seen to be equally important. The adverse pressure gradients at the outlet are not seen to cause any separation at the contraction outlet even at very high mass flow rates. Also the  $Re_{\delta_1}$  at the outlet is seen to be well below the value required to conduct instability experiments. Hence these two parameters are not considered in the optimisation procedure. The parameters chosen for optimisation,  $Re_{\delta_{1cr}}$  and  $\sigma_p$  are named as Objective functions F1 and F2 respectively.

### 3.3.2. Multi-objective Optimisation

To perform the multi-objective optimisation the objective space of the problem is first plotted between functions  $F_1$  and  $F_2$  are first normalised and then plotted against each other. This objective space is shown in Fig. 3.16 and consist of all possible solutions of the optimisation problem.

The objective space is a curve since there is only one input parameter to the problem which is the parameter  $f$ .

Next the Pareto optimal points are found on this objective space using the weighted sum method method. From the results in Fig. 3.17 is evident that the weighted sum method is successful in finding all the Pareto optimal points in the entire objective domain. Hence it is deemed a suitable method of optimisation.

To find the best performing  $f$  value from all the Pareto optimal the minimal distance from the ideal point (0,0) which is a pseudo-point of highest  $Re_{\delta_{1cr}}$  and  $\sigma_p$ . These distances  $d_1 \dots d_n$  are visualised in Fig. 4.7, where  $n$  is the number of Pareto optimal point.

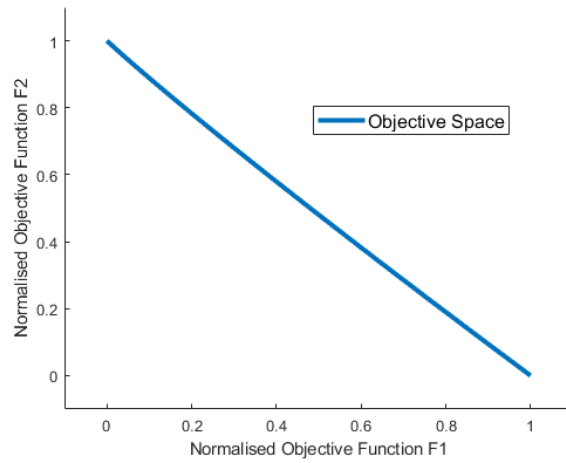


Figure 3.16: Objective Space  $F_1$  vs  $F_2$

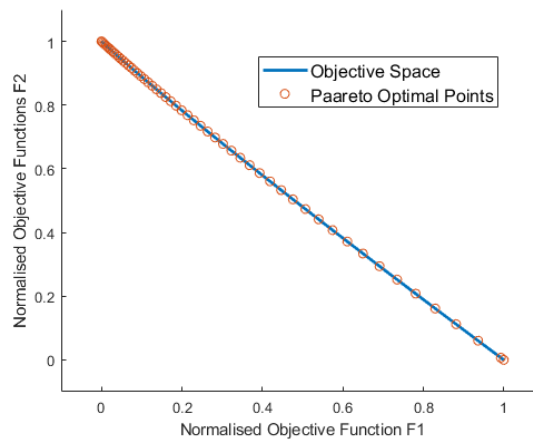


Figure 3.17: Optimal Points- Weighted Sum Method

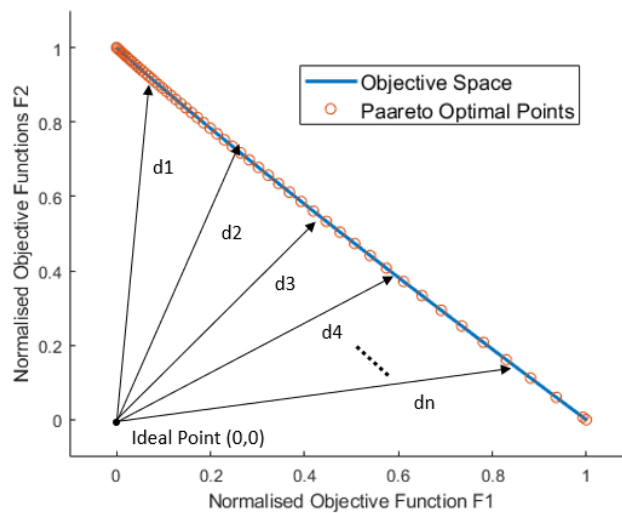


Figure 3.18: Distance From Ideal Point (0,0)

These distance are plotted versus  $f$  in Fig. 4.8 and the minimum point indicated is chosen to be the most optimum  $f$  value for the wall shape of the contraction.

The results from the optimisation indicate that the best performing shape has an optimised value

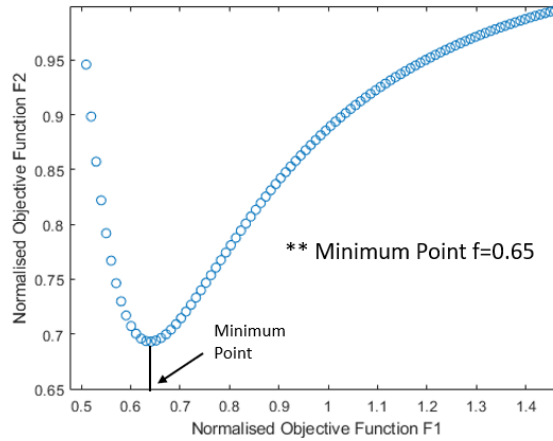


Figure 3.19: Plot Parameter  $f$  vs Minimum Distance from Ideal Point (0,0)

of  $f = 0.65$ . This means that a wall shape with an inflection point downstream of the centreline has an overall better performance than a wall shape with the inflection point at the centre. This validates the use of Brassard's transformation 2005 [15] over Bell and Mehta's 1988 [13] fifth order polynomial with  $f = 1$ . A wall shape with  $f = 0.65$  has an inflection point that is pushed downstream by 27.5mm.

The optimisation results show good agreement with past research done on contraction design. Research shows that when higher order polynomial wall shapes are used having an inflection point downstream of the centreline, it helps reduce the risk of separation as seen in Sargison 2004 [17] and Lakshman 2018 [68].

Taking practical considerations into account the experimental setup was manufactured using a rounded off  $f$  value of 0.7. This wall shape was then used for the unsteady simulations. The wall shape and its inflection point distance are shown in Fig. 3.20.

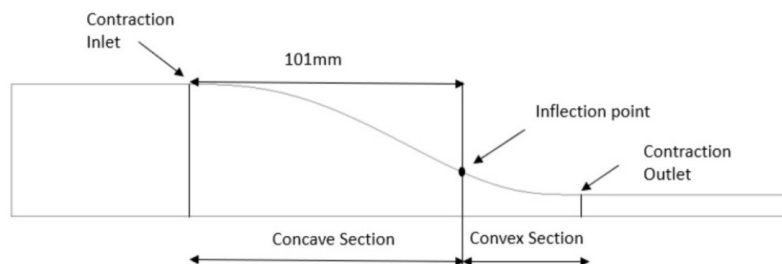
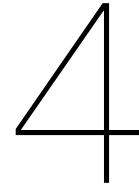


Figure 3.20:  $f=0.7$  Contraction shape and Inflection Point Distance used for experiments

### **Chapter Summary**

This chapter details the results obtained from the steady state simulations and optimisation of the contraction shape. Firstly the procedure to find the optimum contraction length and settling chamber length are given. After this the effects of changing wall shape on different flow parameters are detailed. Next two of the most important parameters are chosen and used to perform a multi-objective optimisation to obtain the best wall shape.





# Results and Discussion- Unsteady Simulations

This chapter details and discusses the results obtained from the unsteady simulations performed on the wind tunnel contraction. Firstly results from unsteady laminar viscous simulations without any perturbations are compared with steady state results. After which results from unsteady laminar viscous simulations with and without side-walls with the addition of sinusoidal perturbations are analysed for instabilities. Finally results from LES are detailed with perturbations in the form of random inlet turbulence levels.

## 4.1. Unsteady (Without Perturbations)

An unsteady simulation without perturbations is performed to analyse if the flow is stable in the absence of any forced disturbances. This steady state solution will also act as a reference state for the perturbation analysis in the following sections. This is done by comparing the unsteady simulation results with the results from steady state simulations at experimental conditions of 0.05kg/s mass flow rate. As domain 2 (without side walls) and domain 3 (with side walls) have different steady states due to wall effects, both the domains are compared independently. The velocity contours and profile,  $\sigma_p$  and x-vorticity plots will be analysed for the comparison.

### 4.1.1. Domain-2

The x-velocity contours are plotted on a yz plane at x=0.175 at the contraction outlet. It is seen that the steady and unsteady plots of these contours converge to the same solution.

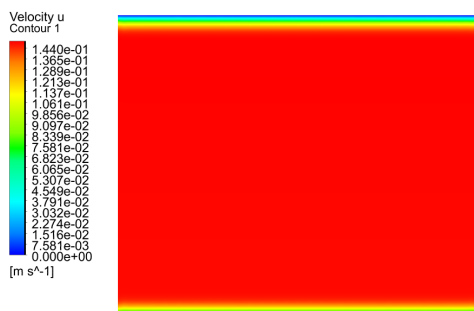


Figure 4.1: X-Velocity Contour Unsteady- Domain-2

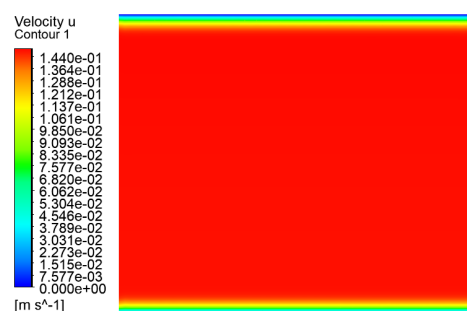


Figure 4.2: X-Velocity Contour Steady - Domain-2

The x-velocity profile and pressure non-uniformity  $\sigma_p$  at the contraction outlet are plotted and detailed Fig. 4.3, Fig. 4.4 and Table. 4.1. The figures show that the velocity profiles collapse onto each other and the value of  $\sigma_p$  are nearly the same. These further confirm the convergence of the steady and unsteady simulations for Domain-2.

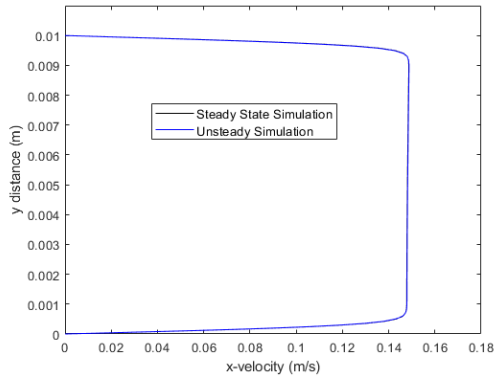


Figure 4.3: Unsteady vs Steady Velocity Profile Outlet Comparison - Domain 2

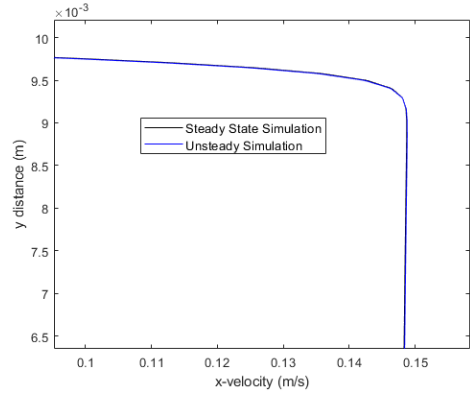


Figure 4.4: Velocity Profile - Zoomed in View

Table 4.1: Comparison of Steady and Unsteady Flow Parameters- Domain 2

Simulation Type	$\sigma_p$
Steady State	0.0349
Unsteady	0.0351

### 4.1.2. Domain-3

For domain 3 the x-vorticity contours are plotted on a yz plane at x=0.175 at the contraction outlet as shown in Fig 4.5 and Fig. 4.6. It is seen that the steady and unsteady simulations converge to produce



Figure 4.5: X-Vorticity Contour Steady- Domain 3



Figure 4.6: X-Vorticity Contour Unsteady- Domain 3

nearly identical vorticity fields. The steady state solution of the vorticity field seems to form 3 distinct vortices near the side wall: a large elongated counterclockwise vortex that spreads from from the top to bottom wall, a small clockwise vortex on the bottom wall and a small clockwise vortex on the top wall. These vortices remain confined to the side wall and do not cause flows that effect the centre-line velocity of the channel. The formation of similar corner vortices has also been observed by Lastra et al 2013 [69] in their experimental study on the design of wind tunnel contractions.

The centre-line x-velocity profiles and non-uniformity  $\sigma_p$  are also plotted and detailed.

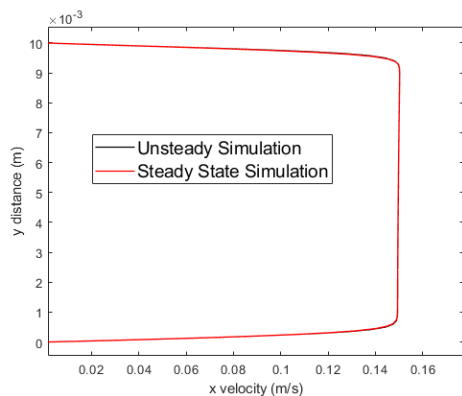


Figure 4.7: Unsteady vs Steady Simulation Velocity Profile  
Outlet Comparison: Domain 3

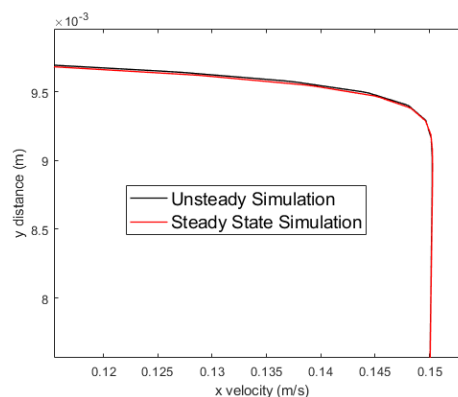


Figure 4.8: Velocity Profile - Zoomed in View

It can be seen from Fig. 4.7 and Fig. 4.8 that the velocity profiles of both the cases collapse on each other. Further from Table 4.2 it can be seen that the  $\sigma_p$  is nearly identical which further confirms the convergence.

Table 4.2: Pressure Profile Non-Uniformity Comparison of Steady and Unsteady Simulations

Simulation Type	$\sigma_p$
Steady State	0.0357
Unsteady	0.0356

The above results detail the steady state solutions of the systems which will be used as reference states for the perturbation analysis in the following sections. Further x-velocity monitors were added inside the contraction to check for velocity unsteadiness and the results showed constant values. The results also show that without an external forcing source, no curvature instabilities like Gortler vortices form on the top wall of the contraction. This shows that there is a need for forced perturbations to exist in the flow field. This result is supported by experimental and DNS research on Gortler vortices where the instability is triggered by forced perturbations as seen by Boiko et al 2010 [60] and Sharma and Ducoin 2018 [54].

## 4.2. Unsteady Laminar With Perturbations (Without Side Walls)

In this section results from transient laminar simulations by forcing sinusoidal perturbations in the boundary layer are detailed and discussed. Perturbations with six different wavenumbers  $\lambda = 83.33, 166.66, 250, 333.33, 416.66$  and  $500$  will be analysed to see their effect on boundary layer instabilities in the contraction. The simulations are run for a flow time of 40 seconds and performed on domain 2.

### 4.2.1. Perturbation Wave-number = $83.33m^{-1}$ (1 Sine Wave)

In this subsection the results on forcing perturbations of wavenumber 83.33 are detailed.

#### Initial Perturbation Velocity Field

The perturbation is introduced 54mm upstream of the contraction inlet on the top boundary layer. A wavenumber of  $83.33m^{-1}$  produces a velocity perturbation in the negative y-direction in the form of 1 sine wave. This is shown as a x-velocity contour plot in the YZ-plane at  $x=-54mm$  in Fig. 4.9.

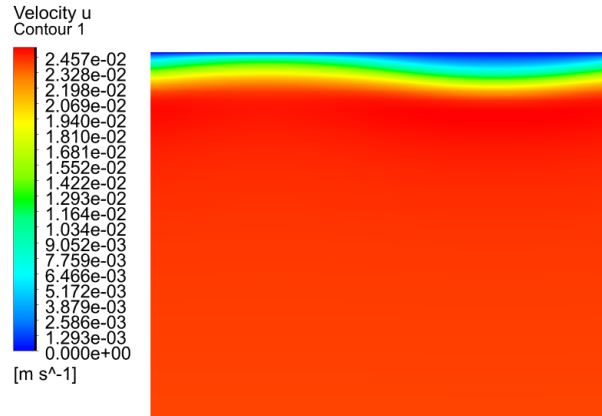


Figure 4.9: X-Velocity Contour Plot of Initial Perturbation on YZ-Plane at X=-54mm

#### Instability Evolution in Contraction

To visualise the growth of the Gortler instability in the contraction, several YZ-plane cross sections are taken along the length of the contraction as shown in Fig. 4.10. The planes are generated from the inlet of the contraction at  $x=0m$  to the outlet at  $x=0.175m$ .

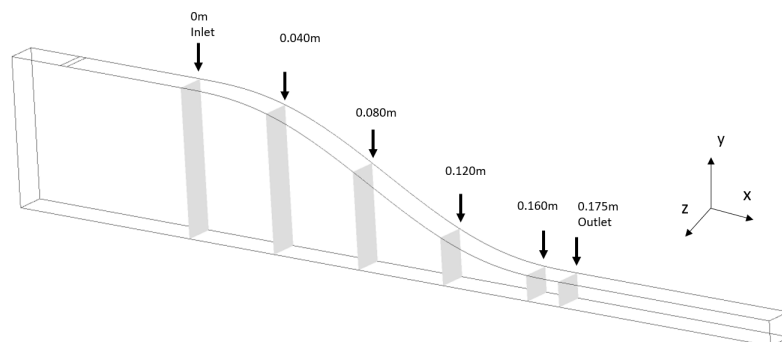


Figure 4.10: YZ planes at different x distances to visualise vortex growth

The x-velocity contours of the top boundary layer are plotted on these parallel planes to analyse the growth of Gortler vortices as shown in Fig. 4.11.

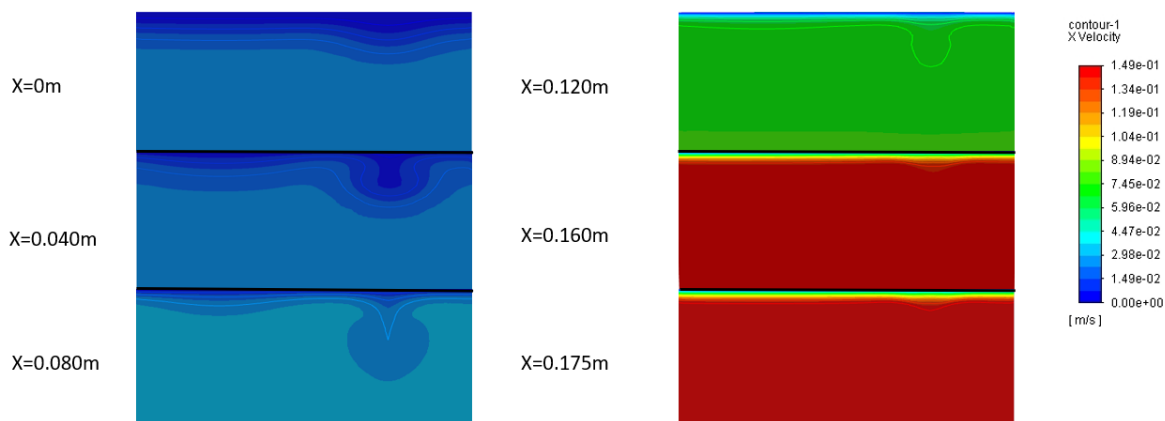


Figure 4.11: Growth of Gortler Instability shown by x-velocity contour plot from  $x=0$  to  $x=0.175$

From Fig. 4.11 it is evident that the perturbation grows due to the curvature of the contraction. It is seen that the instability causes an elongation of the trough of the sine wave which leads to a thickening of the boundary layer. Initially a spike like structure is seen at a downstream distance of around  $x=0.04\text{m}$ , after which a mushroom like structure is formed. Both these structures were also found in experimental results by Peerhossaini and Wesfreid 1988 [58].

The mushroom structure consists of counter-rotating vortices that transport low momentum fluid from the boundary layer to the bulk flow and high momentum fluid to the boundary layer. This growth and mushroom structure is also seen in experimental studies like Benmalek 1993 [70], Ito 1980 [71] and DNS by Mendez et al 2018 [50], Souza et al 2004 [72] results on perturbed boundary layers on concave walls. Fig 4.12 shows a comparison between experimental, DNS and transient laminar results from the present work. The similarity of the mushroom structure is seen in the comparison.

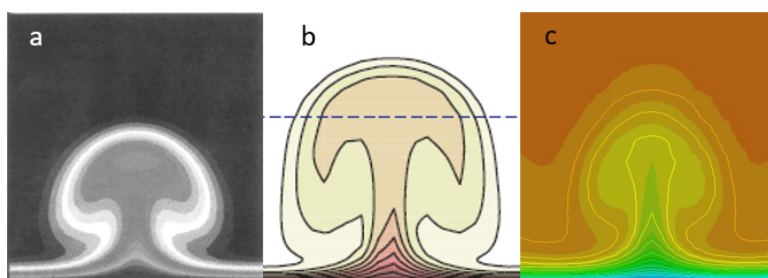


Figure 4.12: (a) Experimental Benmalek 1993 [70] (b) DNS Mendez et al 2018 [50] (c) Present work comparison on mushroom structure in Gortler Instability.

To analyse if the vortices formed due to the instability become increasingly unstable as they exit the contraction, the stream-wise direction vorticity contours are plotted as shown in Fig. 4.13.

From Fig. 4.13 it is seen that the induced perturbation initially gains energy in the concave section of the contraction, which results in higher vorticity. However, near the outlet the vortex becomes stable and begins to lose energy. It is also seen that secondary instabilities arise around  $0.04\text{m}$  downstream

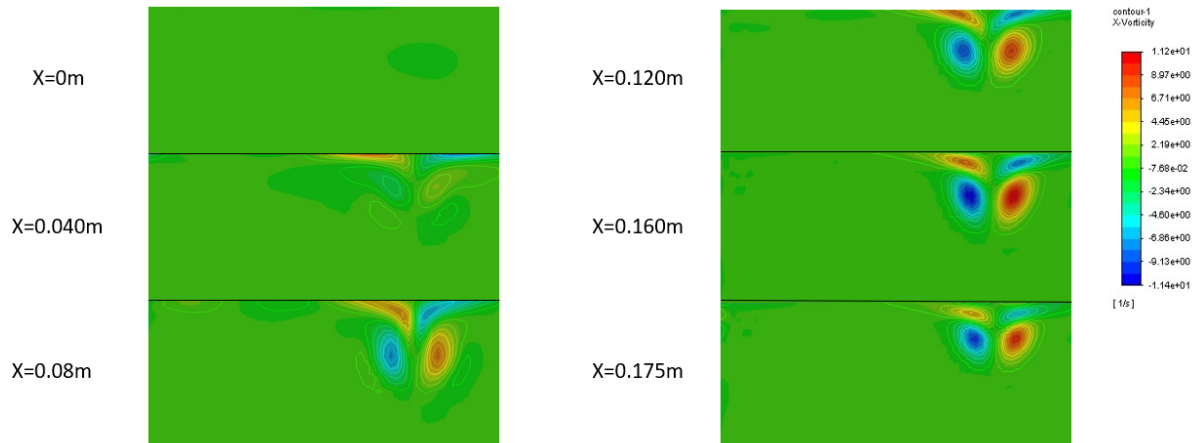


Figure 4.13: Growth of Gortler Instability shown by x-vorticity contour plot from  $x=0$  to  $x=0.175$

of the contraction inlet. The secondary instability consists of a second pair of steady counter-rotating vortices that are formed from the initial perturbation. These vortices do not generate further instabilities and slowly start losing energy at the end of the contraction.

The secondary vortices formed remain close to the top boundary layer and do not migrate downwards. This formation of secondary vortices is also described in DNS studies by Ren and Fu 2015 [73] for high speed boundary layers on concave walls. A comparison of the secondary instabilities is shown in Fig. 4.14 and Fig. 4.15.

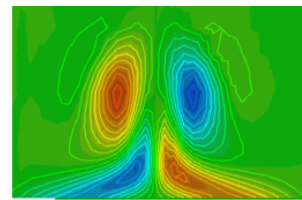
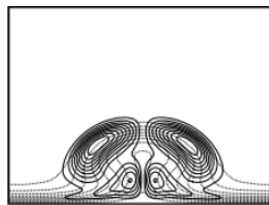


Figure 4.14: Secondary Instability in DNS by Ren and Fu 2015 [73] Figure 4.15: Secondary instability formed within contraction in present study

To further analyse at which specific point in the contraction the secondary vortices start losing energy, iso-surfaces of stream-wise vorticity  $+8.0$   $1/s$  and  $-8.0$   $1/s$  are generated and shown in Fig. 4.16. The thickness of the iso-surface shows how the vorticity varies with the stream-wise coordinate. It is seen that the maximum vorticity occurs at a distance of  $0.153m$  downstream of the inlet. The maximum values were found to be  $+11.5$   $1/s$  and  $-11.5$   $1/s$ . The vorticity maximums were found to be in the secondary vortices. It is seen that as the vortex moves further downstream towards the inlet it loses more energy as shown by the tapering of the iso-surface.

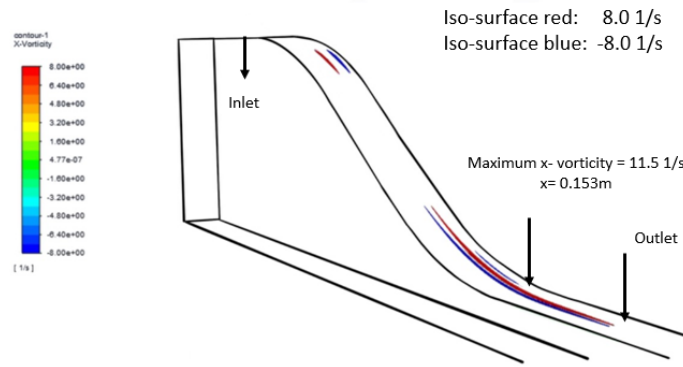


Figure 4.16: Iso-surface of Maximum values of Clockwise (Blue) and Counter- Clockwise Vorticity (Red)

### 4.2.2. Perturbation Wave-number= $166.66m^{-1}$ (2 Sine Waves)

In this subsection the results on forcing perturbations of wavenumber  $166.66m^{-1}$  are detailed.

#### Initial Perturbation Velocity Field

The perturbation is introduced 54mm upstream of the contraction inlet on the top boundary layer. A wavenumber of  $166.66m^{-1}$  produces a velocity perturbation in the negative y-direction in the form of 2 distinct sine wave. This is shown as a x-velocity contour plot in the YZ-plane at  $x=-54mm$  in Fig. 4.17.

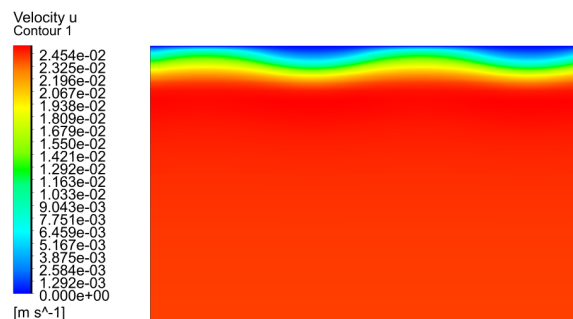


Figure 4.17: X-Velocity Contour Plot of Initial Perturbation on YZ-Plane at X=-54mm

#### Instability Evolution in Contraction

The growth of the instability is visualised as described in Fig. 4.10 of section 4.2.1. The contours of the x-velocity of the top boundary layer are plotted on these planes in Fig. 4.18 to visualise the evolution of the flow in the contraction.

It is seen that as the perturbation enters the contraction inlet, both the troughs of the sine wave begin elongate to form two distinct Gortler vortices. The characteristic mushroom structure of the vortex as shown in Fig 4.12 is seen at a distance 80mm downstream of the contraction inlet. The vortex structure grows rapidly in the concave half of the section while in the convex section the vortex structure seems to diminish and gets elongated in the decreasing boundary layer. To further investigate the formation

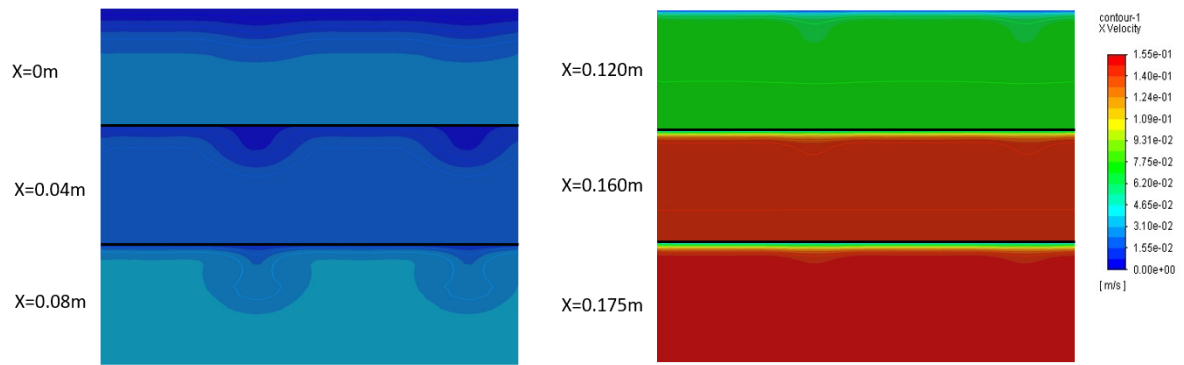


Figure 4.18: Growth of Gortler Instability shown by x-velocity contour plot from x=0 to x=0.175

of the vortices, the x-vorticity contours are plotted as shown in Fig. 4.19.

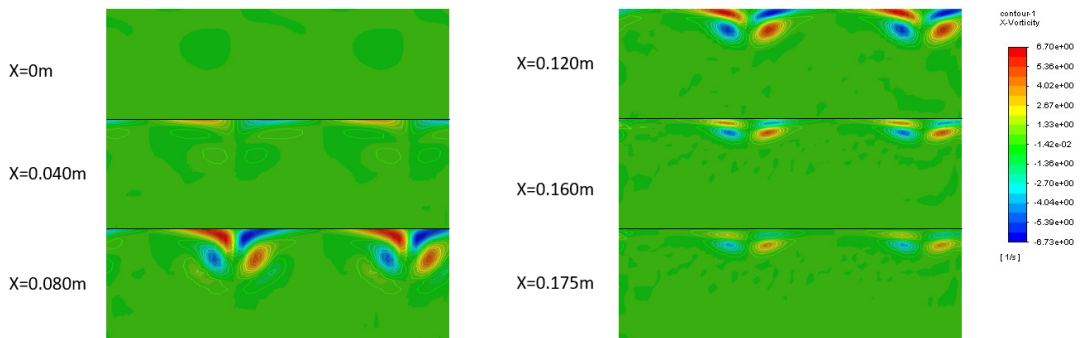


Figure 4.19: Growth of Gortler Instability shown by x-vorticity contour plot from x=0 to x=0.175

From the figure it is evident that a pair of secondary instability vortices are also formed for wavenumber  $166.66m^{-1}$ . These secondary vortices initially gain energy in the concave section of the contraction while losing energy and fading away at the outlet of the contraction. The primary vortices also show a similar behaviour. To quantify the extent of increase and decrease of x-vorticity in the contraction, iso-surfaces are generated of the x- vorticity  $+5.5$  1/s and  $-5.5$  1/s Fig. 4.20.

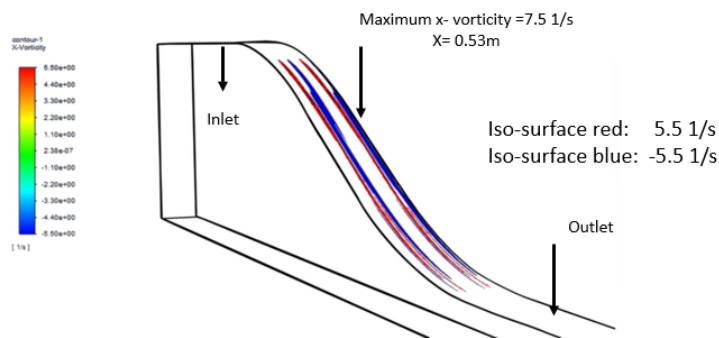


Figure 4.20: Iso-surface of Maximum values of Clockwise (Blue) and Counter- Clockwise Vorticity (Red)

The maximum vorticity value was found to be +7.5 1/s and -7.5 1/s at a distance of 0.53m downstream of the inlet. The vorticity maximums are seen to be from the primary vortices that are generated due to the initial perturbation. After the maximum is reached the vortices quickly start losing energy as the flow moves downstream towards the contraction outlet as seen from the tapering of the iso-surfaces..

### 4.2.3. Perturbation Wave-number= $250m^{-1}$ (3 Sine Waves)

In this subsection the results on forcing perturbations of wavenumber  $250m^{-1}$  are detailed.

#### Initial Perturbation Velocity Field

The perturbation is introduced 54mm upstream of the contraction inlet on the top boundary layer. A wavenumber of  $250m^{-1}$  produces a velocity perturbation in the negative y-direction in the form of 3 distinct sine wave. This is shown as a x-velocity contour plot in the YZ-plane at  $x=-54mm$  in Fig. 4.21.

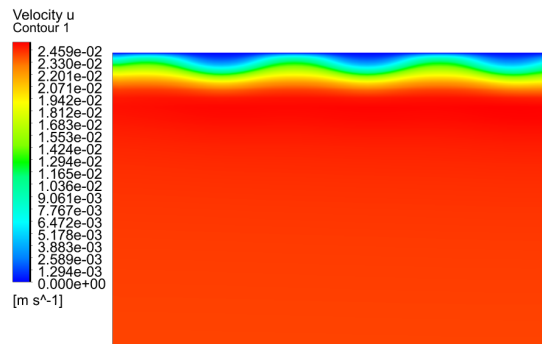


Figure 4.21: X-Velocity Contour Plot of Initial Perturbation on YZ-Plane at X=-54mm

#### Instability Evolution in Contraction

To understand the growth of the Gortler vortices in the contraction the x-velocity contours are plotted at different yz planes as described in Fig. 4.10 of section 4.2.1.

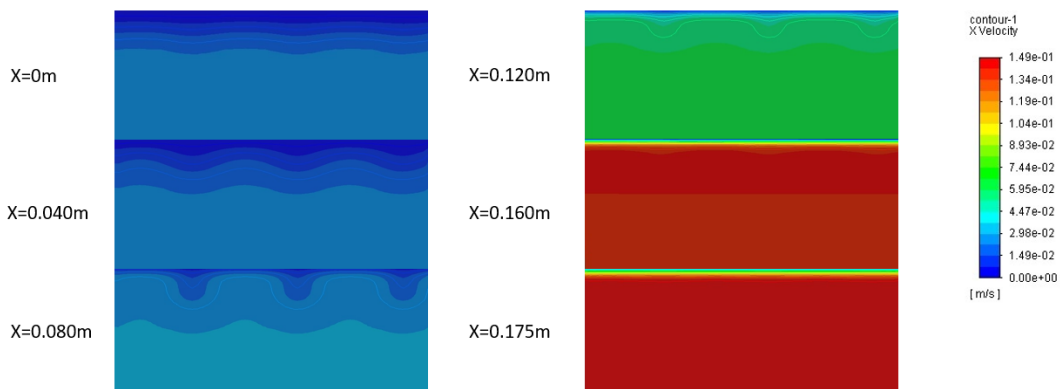


Figure 4.22: Growth of Gortler Instability shown by x-velocity contour plot from  $x=0$  to  $x=0.175$

Fig. 4.22 that the instability initially grows in the concave section but then begins to lose energy in

the concave section. The mushroom structure typical of Gortler vortices is not fully developed for this wavenumber which indicates that only a weak secondary instability is formed within the contraction.

To further analyse the formation of a weak secondary instability, the x-vorticity is plotted in the contraction. This is shown in Fig. 4.23.

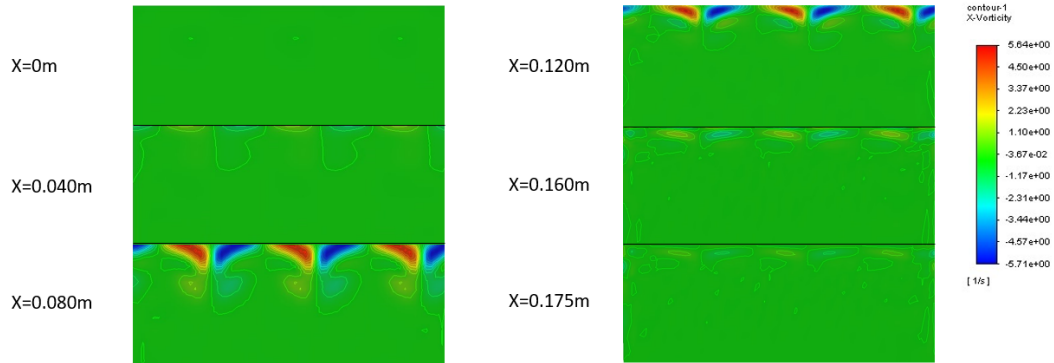


Figure 4.23: Growth of Gortler Instability shown by x-vorticity contour plot from  $x=0$  to  $x=0.175$

The vorticity contours also show that the secondary vortices are very weak when compared to the primary vortices and hence are not efficient in transporting momentum to and from the boundary layer. As the flow develops in the contraction both the primary and secondary vortices lose energy and die out.

To find the maximum vorticity in the contraction iso-surfaces of the vorticity maxima are plotted. The maximum vorticity values are  $+6.5 \text{ 1/s}$  and  $-6.5 \text{ 1/s}$  and occur at a distance  $0.099\text{m}$  downstream of the contraction inlet. This is shown in Fig. 4.29 where the iso-surfaces have maximum thickness. The maximum is seen to occur in the primary vortices after which the vortices lose energy as seen in the figure.

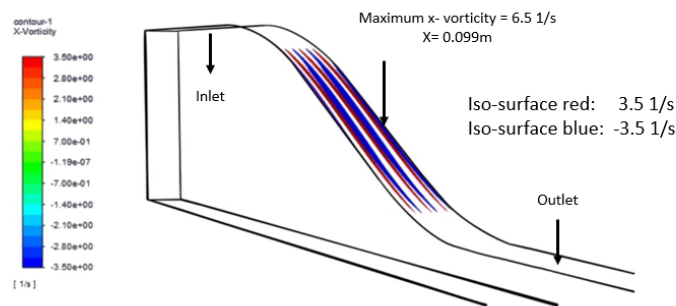


Figure 4.24: Iso-surface of Maximum values of Clockwise (Blue) and Counter- Clockwise Vorticity (Red)

#### 4.2.4. Higher Wave-numbers

Three higher wavenumber perturbations were also simulated in the contraction,  $\lambda = 333.33\text{m}^{-1}$  (4 sine waves),  $416.66\text{m}^{-1}$  (5 sine waves) and  $500\text{m}^{-1}$  (6 sine waves). It was found that none of these

wavenumber produce any secondary instabilities in the contraction. All the primary vortices lose energy and fade away by the time they reach the end of the contraction. Hence their results are excluded in this study.

#### 4.2.5. Comparison of Different Perturbations

All the wavenumbers were to seen to form steady Gortler vortices in the contraction to varying degrees. The most unstable wavenumber was found to be  $\lambda = 83.33m^{-1}$  ( 1 sine wave) which formed secondary vortices with higher vorticity. This wavenumber is also seen to be the most unstable from linear stability analysis [74] and is used to perturb flows in DNS studies such as Mendez et al [39]. This was also the only wave number to produce x-vorticity maxima in the secondary vortices, while all the others produced maxima on their primary vortices. However for all wavenumbers simulated it was seen that both primary and secondary vortices begin to lose energy and dissipate.

A lower wavenumber produced a higher maximum vorticity in the contraction. The downstream distance of the maxima also varies with wavenumber. For a lower wave number of  $\lambda= 83.33m^{-1}$ , since the secondary vortices dominate the instability, the maximum is reached downstream of the inflection point at a distance of 0.153m from contraction inlet. For wavenumbers  $\lambda= 166.66m^{-1}$  and 250, the primary vortices dominate the flow. As the primary vortices gain energy earlier in the contraction, the maxima of the vortices are reached at a distance of 0.053m and 0.099m respectively. For all the wavenumbers simulated the maximum x-vorticity only remains for around 20mm before its starts dissipating.

#### 4.2.6. Secondary Instabilities and Inflectional Velocity Profiles

The formation of secondary instabilities only occurs for lower numbers of  $\lambda= 83.33m^{-1}$ , 166.66 and 250 and is confirmed by plotting the stream-wise velocity profiles taken in the wall normal direction. It is seen that for these wavenumbers, in the up-wash region generated by the vortices, an inflection point is created in the velocity profile within the boundary layer. The velocity profile at different stream-wise coordinates for the most unstable wavenumber  $x=83.33$  is plotted in the contraction and shown in Fig.4.25- 4.28.

It is observed that the inflection point is formed at around  $x=0.030$  and vanishes at around  $x=0.160$ . This is in conjunction with the x- vorticity plots in Fig. 4.13 which shows that the presence of an inflectional point in the boundary layer is the necessary condition for formation of secondary instabilities. This is also confirmed by experimental evidence by studies such as Mitsudharmadi et al 2005 [49] where inflectional profiles were seen to mark the onset of secondary instabilities.

A similar formation of inflection points was observed for  $\lambda= 166.66$  and 250 perturbations. However higher than this no inflectional velocity profiles were found which is aligned with the x-vorticity results for these wavenumbers.

#### 4.2.7. Effects of Gortler Vortices on Wall Shear in Contraction

The formation of the Gortler vortices in the contraction is seen to change the wall shear stress distribution on the top wall. Fig. 4.29 shows the contours of x-wall shear stress distribution on the top wall. The figure shows alternating streaks formed by periodic regions of high and low wall shear stress. A wavenumber of  $333m^{-1}$  is chosen to demonstrate this phenomenon.

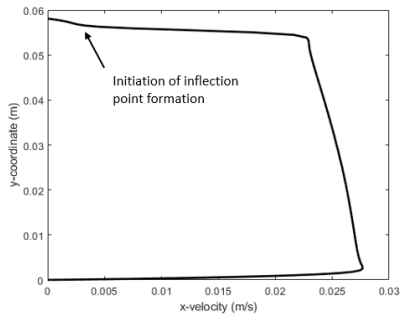


Figure 4.25: X-Velocity Profile Showing Initialisation of Inflection Point formation at  $x=0.030\text{m}$  in upwash region

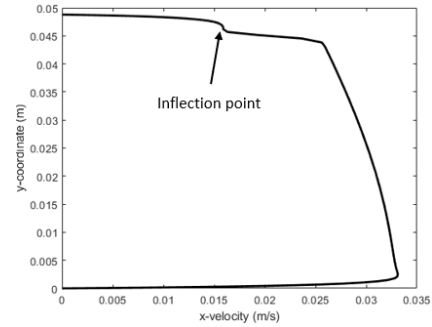


Figure 4.26: X-Velocity Profile Showing Inflection Point at  $x=0.060\text{m}$  in upwash region

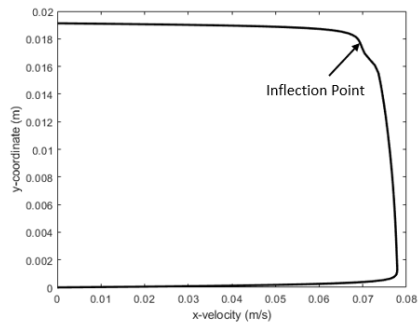


Figure 4.27: X-Velocity Profile Showing Inflection Point at  $x=0.060\text{m}$  in upwash region

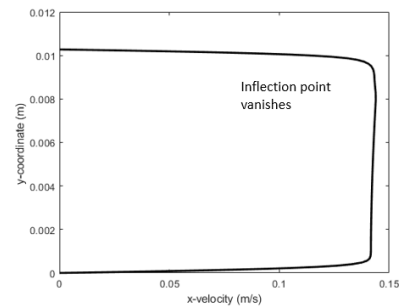


Figure 4.28: X-Velocity Profile Showing Inflection Point Vanishing at  $x=0.160\text{m}$  in upwash region

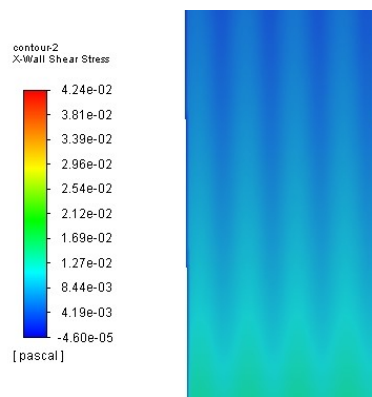


Figure 4.29: Streak formation in X-Wall Shear Stress Distribution on Top Wall of Contraction

These streaks are also observed in experimental research on the formation of Gortler vortices on curved surfaces such as experimental work by Huang 2021 [59]. The formation of these streaks can be attributed to the generation of up-wash and down-wash areas induced by the counter-rotating vortices as shown in Fig. 4.30. High momentum fluid moving towards a boundary layer causes it to become thinner thus increasing wall shear stresses in that region. The opposite effect is seen when low momentum fluid moves away from the boundary layer.

The change in periodic distribution of wall shear stress as the Gortler vortices move through the contraction is shown in Fig. 4.31. The figure shows that the amplitude of sinusoidal x-wall shear stress

Red Vortices: + Vorticity ( Counter Clockwise )  
 Blue Vortices: - Vorticity ( Clockwise )

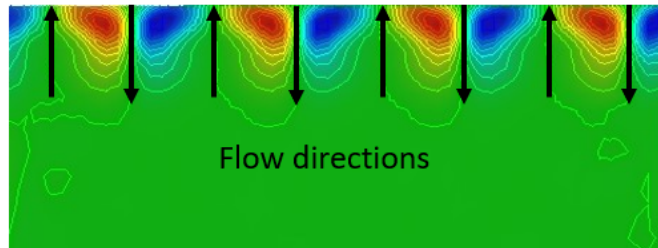


Figure 4.30: Upwash and Downwash generated by Gortler Vortices

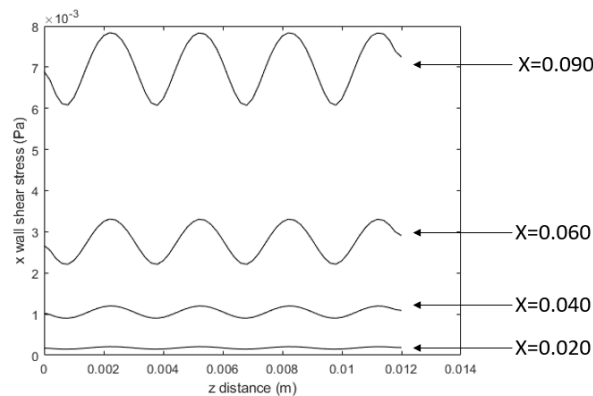


Figure 4.31: Evolution of Periodic X Wall Shear Stress Distribution as Flow Evolves in Contraction

increases as the vortices grow. The mean of the wave also increases with x distance since the flow is accelerated in the contraction leading to decrease in boundary layer thickness.

### 4.3. Unsteady Laminar With Perturbations (With Side Walls)

In section 2.4.2 the domain simulated (Fig 2.4) has periodic boundaries on either side in the span-wise direction. However since the experimental setup consists of a walled setup, perturbation analysis was also performed on a walled domain (Fig 2.6) to analyse if perturbations destabilize the system from its steady state solution.. In section 2.4.2 it was also seen that the most unstable wavenumber with the highest vorticity is  $\lambda = 83.33 \text{ m}^{-1}$ . Hence, this wavenumber is used to analyse the wall effects.

The x-velocity contours are plotted in Fig 4.32 to see the growth of the instability in the contraction.

From the x-velocity contours it is seen that the two waves in the contraction evolve very differently. The wave does not evolve into a Gortler vortex but instead merges into the boundary layer on the side wall. However the wave near the centre of the contraction continuous to grow independent of the wall effects and forms a steady Gortler vortex.

To visualise if the perturbation destabilises the solution from its steady state the x-vorticity contours at the contraction outlet are compared with the steady state solution obtained in subsection 4.1.2.

It is seen from the x-vorticity contours that the Gortler vortices do not destabilise the flow field from

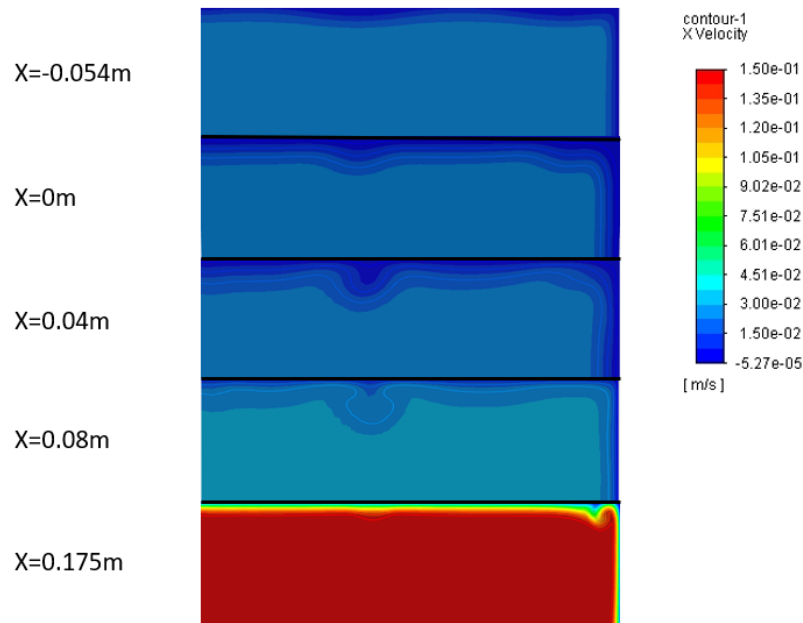


Figure 4.32: Growth of Gortler Instability shown by x-velocity contour plot from  $x=0$  to  $x=0.175$



Figure 4.33: Unsteady Solution: X- Vorticity without Perturbations at Contraction Outlet  $x=0.175$



Figure 4.34: Unsteady Solution: X- Vorticity with additional Gortler Vortices at Contraction Outlet  $x=0.175$

its steady state solution but a new steady state solution is formed (Fig. 4.34) which is superimposition of the steady state solution in Fig 4.33 with steady Gortler vortices. The strong corner vortices remain in their original steady state and are not affected by the weak Gortler vortex that is absorbed.

The centre-line velocity needs to be unaffected by the perturbations. Hence to see if there is any

flow towards the centre-line due to the addition of perturbations, the z-velocity is plotted at the contraction outlet  $x=0.175\text{m}$  in Fig 4.35.

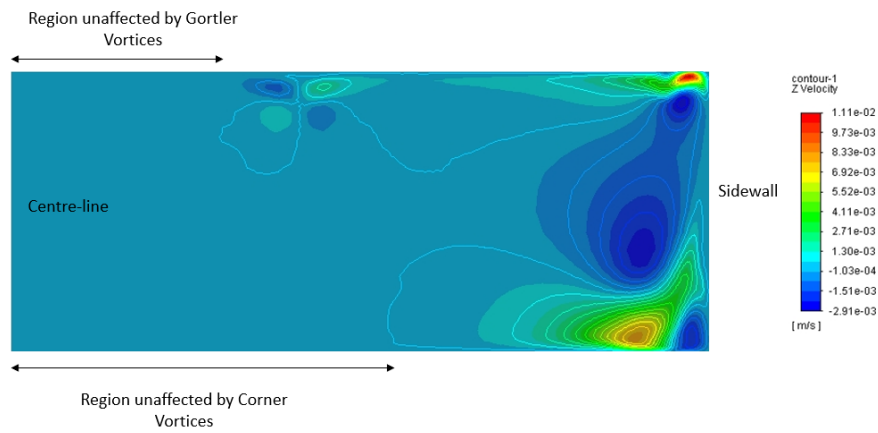


Figure 4.35: Z-Velocity Contours to Show Extent of Contraction outlet affected by Corner and Gortler Vortices

From the figure it is seen that the width of the channel is more than sufficient to ensure that the centre-line velocity remains undisturbed due to the presence of vortices in the contraction. The centre-line velocity of the un-perturbed and perturbed channel are shown in Fig 4.36 and 4.37 to show that they are identical.

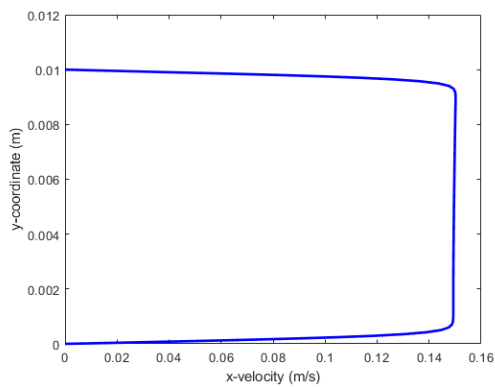


Figure 4.36: Unperturbed Simulation Centre-Line X- Velocity vs Y-Coordinate at X=0.175

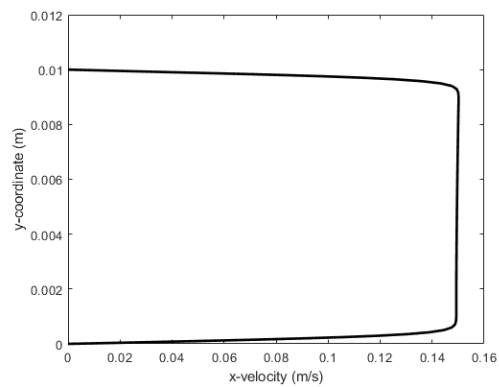


Figure 4.37: Perturbed Simulation Centre-Line X- Velocity vs Y-Coordinate at X=0.175 with Gortler Vortices

This shows that the centre-line boundary layer where the experiments need to be performed is remains steady and undisturbed by the Gortler vortices formed in the contraction. Hence this validates the novel 1D contraction shape and deems it suitable for use for heat transfer boundary layer measurements to analyse hydrodynamic instabilities in SCO<sub>2</sub>.

#### 4.4. Alternative Perturbation method: Random Inlet Turbulence

In section 4.2 and 4.3 the perturbations used to trigger Gortler vortices were in the form of sinusoidal waves with fixed wave-numbers in the span-wise direction. However experimental research such as Bippes and Deyhle [75] has shown that free-stream turbulence also easily excites Gortler vortices in wind tunnels. To test if these vortices are triggered in the 1D contraction concave-convex geometry, an LES simulation is performed using an inlet turbulence level of 5%. The x-velocity and x-vorticity contours are plotted in the YZ plane and shown in Fig 4.38.

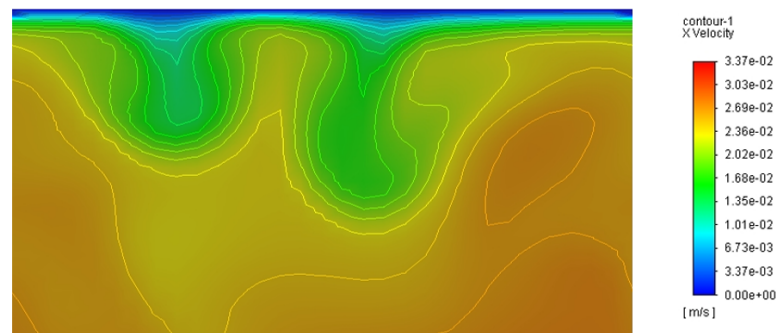


Figure 4.38: X-Velocity Contour Show Unsteady Gortler Vortices at X=0.060 due to inlet turbulence of 5%

The figure shows that the inlet turbulence levels are able to trigger unsteady Gortler vortices in the contraction. Since the random turbulence consists of a number of wavenumbers superimposed onto each other, the vortices formed do not have a fixed wavelength in the span-wise direction and are asymmetric. This results is also seen in DNS simulations by Schrader et al [51] where the Gortler vortices formed on a concave surface are not symmetric as shown in Fig 4.39.

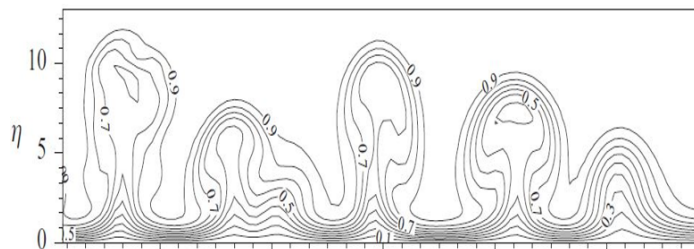


Figure 4.39: Asymmetric Gortler Vortices seen in DNS results of Schrader et al.[51]

Similar to the sinusoidal perturbation, the Gortler vortices formed in the contraction due to inlet turbulence are damped and lose energy as they leave the contraction. It has been shown by Hall [76] that steady perturbations have higher amplitudes than unsteady perturbation. However since the flow through the contraction is laminar and the turbulent flow through the contraction is un-physical, using inlet turbulence to trigger perturbations is not investigated further.

#### Chapter Summary

This chapter details the unsteady simulations performed on the contraction. Firstly the results from unsteady simulations without perturbations are detailed to act as a reference steady state case. Next, results from unsteady simulations adding sinusoidal perturbations of varying wavenumber are shown. The stability of the different wavelengths are compared and their effects on the wall shear of the contraction are given. Finally an alternative method of perturbation using inlet random turbulence is given.

# 5

## Conclusion

This chapter summarises the results obtained from the simulations in this study. The future scope of this field and recommendations for further research are proposed.

### 5.1. Summary

A detailed literature review was conducted on contraction optimisation methods to reduce secondary flows and formation of Gortler vortices in the contraction. It was seen that existing research focuses on general wall shape comparison studies of 2D and 3D contractions but very little research was found on optimisation procedures. The literature on the formation of Gortler vortices is mostly restricted to strictly concave surfaces on which DNS studies have been conducted. Moreover, no studies were found in the field of perturbation simulations in concave-convex contractions.

The present study aimed to overcome this research gap by:

- optimising the geometry of a novel 1D contraction using a multi-objective optimisation to reduce secondary flows such as boundary layer separation and flow non-uniformity's.
- simulating the formation and stability of Gortler vortices in the top boundary layer of the 1D contraction using forced perturbations.

To achieve these research objectives, a computational methodology consisting of physical domain geometry, steady state analysis procedure, optimisation methods, unsteady analysis, boundary conditions, computational domain and mesh, governing equations and numerical methods was used for the numerical simulations.

The key findings of this study are as follows:

For the contraction optimisation, the steady state laminar simulations showed that adverse pressure gradients can occur within the contraction. Qualitatively these pressure gradients match the experimental and numerical data in literature on 2D contractions where the maximum of the adverse pressure gradients occur just within the contraction, both at the inlet and outlet. These adverse gradients were seen to cause flow reversals only at the inlet of the contraction. This reversal could either occur at the edge of the side wall or on the concave wall face. A contraction length of 175mm was found to have no flow reversals and to be the optimum length for this 1D contraction geometry. The length of the settling chamber was selected to be 80mm since this length was found to be sufficient in ensuring the absence of any boundary interference from the contraction and a minimum boundary layer thickness at contraction inlet.

Next, to optimise the wall shape of the geometry, a multi-objective optimisation procedure was used to find the best performing inflection point value given by Brassard parameter  $f$ . It was found that various flow parameters such as contraction critical inlet boundary layer Reynold's number  $Re_{\delta_{1cr}}$ , exit flow non-uniformity  $\sigma_p$ , outlet pressure gradients  $dp/dx$  and outlet boundary layer  $Re_{\delta_{1out}}$  are functions of  $f$ . Since  $Re_{\delta_{1cr}}$  and  $\sigma_p$  were deemed to be the most important for contraction design, they were used as objective functions in the optimisation procedure. A normalised objective space of these two parameters was plotted. The best performing  $f$  value was taken by measuring the distance of every Pareto optimal point from the ideal point (0,0) which had the highest  $Re_{\delta_{1cr}}$  and lowest  $\sigma_p$ . This optimal point was found to be  $f=0.65$ . A rounded value of  $f=0.7$  was selected for the construction of the experimental setup whose inflection point value is around 101mm.

Unsteady simulations on this  $f=0.7$  shape contraction without perturbations showed that there were no fluctuations in the contraction and that the solution converged to the steady state case. Hence, this was taken to be the reference state for the perturbation analysis simulations. Sinusoidal perturbations of varying wavenumbers were added to the unsteady laminar simulation of varying wavenumbers from  $\lambda = 83.33m^{-1}$  to  $500m^{-1}$  by blowing and suction of the boundary layer before the contraction. This perturbation was successful in triggering the Gortler vortices and coherent structures such as spike formation and mushroom structures were observed. This was qualitatively found to be similar to both experimental and DNS results. It was found that  $\lambda = 83.33m^{-1}$  case is the most unstable wavenumber and produces the highest vorticity in the contraction. It also produces strong secondary vortices that dominate the primary vortices. The vorticity maximum was seen to occur in the secondary vortices for this wavenumber but occurred in the primary vortices for all other wavenumbers. The stream-wise coordinate of the vorticity maximum was also seen to vary with the perturbation wavenumber. It was observed that the secondary instabilities were triggered due to inflectional velocity profiles in the boundary layer as seen in experimental studies.

The Gortler vortices were also found to affect the wall shear stress in the contraction. It was seen that Gortler streaks are formed within the contraction on plotting the x-wall shear distribution. These streaks are seen in experimental and DNS studies. The amplitude of the shear variation is seen to rise as the Gortler vortices evolve downstream of the inlet. Sinusoidal perturbations were also added to Domain-3 to analyse the effect of side walls on the formation of Gortler vortices. This analysis was done only for the most unstable  $\lambda=83.33$  wavenumber. It was seen that the Gortler vortices closest to the wall were absorbed into the corner vortices of the steady state case and lost all their energy. The Gortler vortex near the centre line was unaffected by the wall effects and evolved similar to the domain-2 case forming a steady Gortler vortex. It was found that a new steady state was reached which was a superposition of the steady state corner vortices along with the added Gortler vortex near the centre-line. The vortices did not affect the centreline velocity of the bottom boundary and hence the novel 1D contraction was suitable for the boundary layer instability experiments.

Lastly, an alternative method of perturbation using inlet random turbulence intensity perturbation was analysed to see if they are successful in triggering Gortler vortices. It was seen that at an inlet turbulence level of 5%, Gortler vortices were successfully triggered in concave-convex curvature of the 1D contraction. The Gortler vortices formed were not symmetrical and displayed a random behaviour which is also seen in DNS simulations. This was attributed to several wave-lengths being triggered from the initial perturbation.

## 5.2. Recommendations and Scope for Future Research

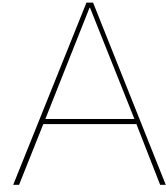
The design and perturbation analysis of contractions is a complex subject and hence there are many more different ideas and research directions that can be taken. Some of these possible future research ideas are listed below.

- The number of variables optimised plays a large role in the complexity of the optimisation prob-

lem. In this study only one input variable is optimised, being the parameter  $f$  which defines the inflection point distance. Further research can be done to also include additional parameters into the optimisation such as inlet curvature, outlet curvature and contraction ratio, to understand if they have positive or negative effects on the performance of the contraction.

- Another research focus could also be to write a computer program that implements an integrated CFD solver along with the multi-objective optimisation technique. Such a solver could automatically find the best wall shape once the code is run. This method is however not possible when commercial solvers like Fluent are used for the simulations of more complex geometries.
- For further understanding the formation and risk of Gortler vortices, more analysis can be done by simulating additional wavenumbers to develop a better understanding of the neutral stability curve for this geometry.
- The effect of other secondary flows like buoyancy also need to be understood better in the design of the experimental setup. Buoyancy due to heat exchange can lead to a destabilisation of a laminar developing Blasius boundary layer in  $\text{SCO}_2$  due to the large gradients in densities near the Widom line. This can affect the transition of the boundary layer by TS waves. DNS simulations could be performed to further understand this affect.
- Numerical simulations could also be performed on the bottom flat wall by adding perturbations to the growing boundary layer to analyse other instability mechanisms such as T-S waves.





# Appendix

## A.1. Mesh Independence study

A mesh independence study is performed for Domain -1 which is the larger domain used for the steady state analysis. The mesh independence is performed for four different mesh sizes. The parameters used for confirming mesh convergence are the mean velocity of the flow at the contraction outlet and the velocity profile at the contraction outlet. The results of the mesh independence study are shown below. Table A.1 shows that after an element number of 1.5 million the mean velocity at the contraction outlet

Table A.1: Summary of Domain type for each simulation

Mesh Number	No. of elements	Mean Velocity (m/s)
Mesh 1	416010	0.130065
Mesh 2	750010	0.125725
Mesh 3	1512010	0.125245
Mesh 4	3206260	0.125266

converges and the solution becomes independent of the mesh. This can also be seen in a graphical view by plotting number of elements with mean mesh velocity as shown in Fig. A.1.

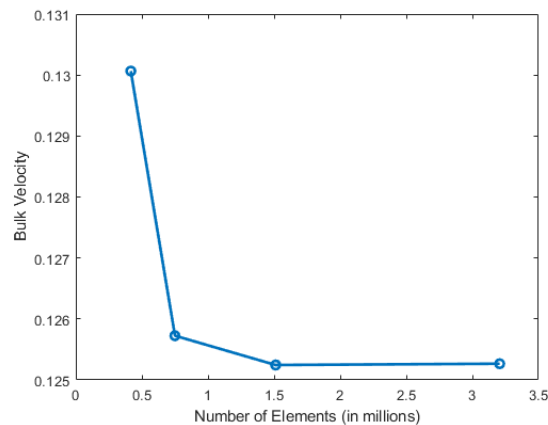


Figure A.1: Number of Elements in Mesh vs Mean Velocity Plot to Show Mesh Independence

Hence from the independence study it is decided that mesh 3, with 1.5 million elements is suitable for

the simulations.

For domain-2 and domain-3 on which unsteady laminar and LES are performed the same basic mesh is used with extra refinement near the wall to fully capture the effects. This refining is done by fixing the wall  $y$ -plus to a certain value required to fully capture the flow in the boundary layer. For the unsteady laminar simulations  $y^+ = 5$  and for the LES  $y^+ = 10$ .

# B

## Appendix

### B.1. Sixth Order Polynomial Shape

The sixth order Sargison [17] polynomial wall shape is also simulated using a steady laminar method to compare with the fifth order transformed polynomial shape. The chosen sixth order shape has its inflection point as downstream as possible while also maintaining a monotonic decrease of the contraction height. This comes to an inflection point distance of  $x_m=105\text{m}$ . This was found to be the best performing sixth order curve shape by Sargison and Rossi. The wall shape is shown in Fig. B.1.

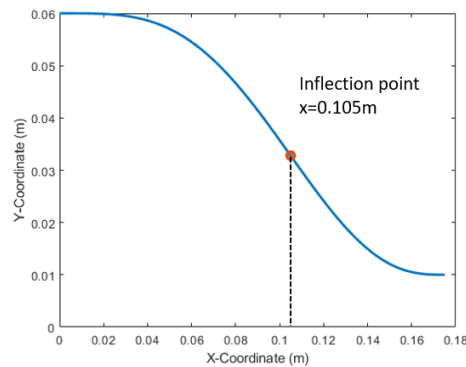


Figure B.1: Number of Elements in Mesh vs Mean Velocity Plot to Show Mesh Independence

Steady state laminar simulations were performed on the sixth order contraction and its  $Re_{\delta_{1cr}}$  was determined. These results are compared to the fifth order polynomial  $f=0.5$  and  $f=0.7$  which have comparable inflection point distances of  $x_m=0.101\text{m}$  and  $x_m=0.119\text{m}$ . The comparison is shown in Table B.1.

Table B.1: Performance Comparison of 6th order to 5th Order Polynomial

Wall Shape Type	$X_m(m)$	$Re_{\delta_{1cr}}$
6th Order	0.105	650
5th Order $f=0.7$	0.101	1060
5th Order $f=0.5$	0.119	2000

This data shows that due to its relatively low  $Re_{\delta_{1cr}}$  indicates a higher risk of flow reversal and separation in the contraction. Hence it is not included in the contraction optimisation procedure.

# Bibliography

- [1] T. Stocker, D. Qin, G. Plattner, *et al.*, "Contribution of working group i to the fifth assessment report of the intergovernmental panel on climate change," *Climate change*, vol. 5, pp. 1–1552, 2013.
- [2] Y. Ahn, S. J. Bae, M. Kim, *et al.*, "Review of supercritical co<sub>2</sub> power cycle technology and current status of research and development," *Nuclear engineering and technology*, vol. 47, no. 6, pp. 647–661, 2015.
- [3] J. Ren, O. Marxen, and R. Pecnik, "Boundary-layer stability of supercritical fluids in the vicinity of the widom line," *Journal of Fluid Mechanics*, vol. 871, pp. 831–864, 2019.
- [4] J. H. Bell and R. D. Mehta, "Design and calibration of the mixing layer and wind tunnel," Tech. Rep., 1989.
- [5] H.-S. Tsien, "On the design of the contraction cone for a wind tunnel," *Journal of the aeronautical sciences*, vol. 10, no. 2, pp. 68–70, 1943.
- [6] M. Cohen and N. Ritchie, "Low-speed three-dimensional contraction design," *The Aeronautical Journal*, vol. 66, no. 616, pp. 231–236, 1962.
- [7] H. Rouse, "Cavitation-free inlets and contractions," *Mech. Eng.*, vol. 71, pp. 213–216, 1949.
- [8] H. Sturm, G. Dumstorff, P. Busche, D. Westermann, and W. Lang, "Boundary layer separation and reattachment detection on airfoils by thermal flow sensors," *Sensors*, vol. 12, no. 11, pp. 14 292–14 306, 2012.
- [9] B. S. Stratford and G. Gadd, "Flow in the laminar boundary layer near separation," 1954.
- [10] B. Stratford, "The prediction of separation of the turbulent boundary layer," *Journal of fluid mechanics*, vol. 5, no. 1, pp. 1–16, 1959.
- [11] T. Morel, "Comprehensive design of axisymmetric wind tunnel contractions," 1975.
- [12] T. Morel, "Design of two-dimensional wind tunnel contractions," 1977.
- [13] J. H. Bell and R. D. Mehta, "Contraction design for small low-speed wind tunnels," Tech. Rep., 1988.
- [14] W. Mikhail, "Rainbird," optimum design of wind tunnel contractions," in *10th Aerodynamic Testing Conference*, 1978.
- [15] D. Brassard and M. Ferchichi, "Transformation of a polynomial for a contraction wall profile," *J. Fluids Eng.*, vol. 127, no. 1, pp. 183–185, 2005.
- [16] C. J. Doolan, "Numerical evaluation of contemporary low-speed wind tunnel contraction designs," 2007.
- [17] J. Sargison, G. Walker, and R. Rossi, "Design and calibration of a wind tunnel with a two dimensional contraction," 2004.
- [18] J. Dagenhart and W. S. Saric, "Crossflow stability and transition experiments in swept-wing flow," Tech. Rep., 1999.
- [19] Y.-x. Su, "Flow analysis and design of three-dimensional wind tunnel contractions," *AIAA journal*, vol. 29, no. 11, pp. 1912–1920, 1991.
- [20] R. D. Mehta, "Aspects of the design and performance of blower tunnel components," Ph.D. dissertation, University of London, 1979.
- [21] L. Prandtl, "Über flüssigkeitsbewegung bei sehr kleiner reibung," *Verhandl. III, Internat. Math.-Kong., Heidelberg, Teubner, Leipzig*, 1904, pp. 484–491, 1904.

- [22] S. Seyyedi, A. Dogonchi, M. Hashemi-Tilehnoee, and D. Ganji, "Improved velocity and temperature profiles for integral solution in the laminar boundary layer flow on a semi-infinite flat plate," *Heat Transfer—Asian Research*, vol. 48, no. 1, pp. 182–215, 2019.
- [23] H. Schlichting and K. Gersten, *Boundary layer theory*. Springer, 2015.
- [24] H. Y. Hafeez and C. E. Ndikilar, "Boundary layer equations in fluid dynamics," in *Applications of Heat, Mass and Fluid Boundary Layers*, Elsevier, 2020, pp. 67–94.
- [25] F.-M. Fang, J. Chen, and Y. Hong, "Experimental and analytical evaluation of flow in a square-to-square wind tunnel contraction," *Journal of Wind Engineering and Industrial Aerodynamics*, vol. 89, no. 3-4, pp. 247–262, 2001.
- [26] J. Watmuff, "Design of a new contraction for the arl (aeronautical research laboratories) low speed wind tunnel," AERONAUTICAL RESEARCH LABS MELBOURNE (AUSTRALIA), Tech. Rep., 1986.
- [27] L. Leifsson and S. Koziel, "Simulation-driven design of low-speed wind tunnel contraction," *Journal of Computational Science*, vol. 7, pp. 1–12, 2015.
- [28] C. Doolan and R. Morgans, "Numerical evaluation and optimization of low speed wind tunnel contractions," in *18th AIAA Computational Fluid Dynamics Conference*, 2007, p. 3827.
- [29] L. Rayleigh, "On the dynamics of revolving fluids," *Proceedings of the Royal Society of London. Series A, Containing Papers of a Mathematical and Physical Character*, vol. 93, no. 648, pp. 148–154, 1917.
- [30] G. Taylor, "□□, stability of a viscous liquid contained between two rotating cylinders, phil," *Transi. Roy. Soc. Lond. A*, vol. 223, pp. 289–343, 1923.
- [31] P. R. Childs, "Chapter 6 - rotating cylinders, annuli, and spheres," in *Rotating Flow*, P. R. Childs, Ed., Oxford: Butterworth-Heinemann, 2011, pp. 177–247, ISBN: 978-0-12-382098-3. DOI: <https://doi.org/10.1016/B978-0-12-382098-3.00006-8>. [Online]. Available: <https://www.sciencedirect.com/science/article/pii/B9780123820983000068>.
- [32] W. R. Dean, "Fluid motion in a curved channel," *Proceedings of the Royal Society of London. Series A, Containing Papers of a Mathematical and Physical Character*, vol. 121, no. 787, pp. 402–420, 1928.
- [33] A. Kalpakli, R. Örlü, and P. H. Alfredsson, "Dean vortices in turbulent flows: Rocking or rolling?" *Journal of visualization*, vol. 15, no. 1, pp. 37–38, 2012.
- [34] L. Rayleigh, "On the stability, or instability, of certain fluid motions," *Proc. London Math. Soc.*, vol. 9, pp. 57–70, 1880.
- [35] H. Görtler, "Über den einfluß der wandkrümmung auf die entstehung der turbulenz," *ZAMM—Journal of Applied Mathematics and Mechanics/Zeitschrift für Angewandte Mathematik und Mechanik*, vol. 20, no. 3, pp. 138–147, 1940.
- [36] J. Floryan, "On the görtler instability of boundary layers," *Progress in Aerospace Sciences*, vol. 28, no. 3, pp. 235–271, 1991.
- [37] J. M. Floryan and W. S. Saric, "Stability of görtler vortices in boundary layers," *AIAA journal*, vol. 20, no. 3, pp. 316–324, 1982.
- [38] W. S. Saric *et al.*, "Görtler vortices," *Annual Review of Fluid Mechanics*, vol. 26, no. 1, pp. 379–409, 1994.
- [39] M. Méndez, M. S. Shadloo, and A. Hadjadj, "Heat-transfer analysis of a transitional boundary layer over a concave surface with görtler vortices by means of direct numerical simulations," *Physics of Fluids*, vol. 32, no. 7, p. 074 111, 2020.
- [40] P. Hall, "The linear development of görtler vortices in growing boundary layers," *Journal of Fluid Mechanics*, vol. 130, pp. 41–58, 1983.
- [41] A. Boiko, A. Ivanov, Y. S. Kachanov, D. Mischenko, and Y. M. Nechepurenko, "Excitation of unsteady görtler vortices by localized surface nonuniformities," *Theoretical and Computational Fluid Dynamics*, vol. 31, no. 1, pp. 67–88, 2017.

- [42] N. Gregory and W. Walker, *The effect on transition of isolated surface excrescences in the boundary layer*. Citeseer, 1956.
- [43] I. E. Beckwith and B. B. Holley, "Gortler vortices and transition in wall boundary layers of two mach 5 nozzles," Tech. Rep., 1981.
- [44] J. D. Swearingen and R. F. Blackwelder, "The growth and breakdown of streamwise vortices in the presence of a wall," *Journal of Fluid Mechanics*, vol. 182, pp. 255–290, 1987.
- [45] S. Winoto, H. Mitsudharmadi, and D. A. Shah, "Visualizing görtler vortices," *Journal of Visualization*, vol. 8, no. 4, pp. 315–322, 2005.
- [46] A. Ito, "Visualization of boundary layer transition along a concave wall," *Flow Visualization IV*, pp. 339–344, 1987.
- [47] G. Huang, W. Si, and C. Lee, "Inner structures of görtler streaks," *Physics of Fluids*, vol. 33, no. 3, p. 034 116, 2021.
- [48] I. Tani, "Production of longitudinal vortices in the boundary layer along a concave wall," *Journal of Geophysical Research*, vol. 67, no. 8, pp. 3075–3080, 1962.
- [49] H. Mitsudharmadi, S. Winoto, and D. Shah, "Secondary instability in forced wavelength görtler vortices," *Physics of Fluids*, vol. 17, no. 7, p. 074 104, 2005.
- [50] M. Méndez, M. S. Shadloo, A. Hadjadj, and A. Ducoin, "Boundary layer transition over a concave surface caused by centrifugal instabilities," *Computers & Fluids*, vol. 171, pp. 135–153, 2018.
- [51] L.-U. Schrader, L. Brandt, and T. A. Zaki, "Receptivity, instability and breakdown of görtler flow," *Journal of fluid mechanics*, vol. 682, pp. 362–396, 2011.
- [52] A. Ducoin, S. Roy, and M. Safdari Shadloo, "Direct numerical simulation of nonlinear secondary instabilities on the pressure side of a savonius style wind turbine," in *Fluids Engineering Division Summer Meeting*, American Society of Mechanical Engineers, vol. 50282, 2016, V01AT08A004.
- [53] W. Liu and J. A. Domaradzki, "Direct numerical simulation of transition to turbulence in görtler flow," *Journal of Fluid Mechanics*, vol. 246, pp. 267–299, 1993.
- [54] S. Sharma and A. Ducoin, "Direct numerical simulation of the effect of inlet isotropic turbulence on centrifugal instabilities over a curved wall," *Computers & Fluids*, vol. 174, pp. 1–13, 2018.
- [55] A. Ducoin, M. S. Shadloo, and S. Roy, "Direct numerical simulation of flow instabilities over savonius style wind turbine blades," *Renewable energy*, vol. 105, pp. 374–385, 2017.
- [56] A. S. Lopes, U. Piomelli, and J. Palma, "Large-eddy simulation of the flow in an s-duct," *Journal of Turbulence*, no. 7, N11, 2006.
- [57] Y.-H. Tseng and J. H. Ferziger, "Large-eddy simulation of turbulent wavy boundary flow—illustration of vortex dynamics," *Journal of turbulence*, vol. 5, no. 1, p. 034, 2004.
- [58] H. Peerhossaini and J. Wesfreid, "Experimental study of the taylor-görtler instability," in *Propagation in systems far from equilibrium*, Springer, 1988, pp. 399–412.
- [59] G. Huang, "Interactions between görtler vortices and the second mode in hypersonic boundary layer," *Physics of Fluids*, vol. 33, no. 11, p. 111 701, 2021.
- [60] A. Boiko, A. Ivanov, Y. S. Kachanov, and D. Mischenko, "Steady and unsteady görtler boundary-layer instability on concave wall," *European Journal of Mechanics-B/Fluids*, vol. 29, no. 2, pp. 61–83, 2010.
- [61] "A. inc, "ansys fluent 18.2 user's manual," 2017.,"
- [62] Y.-H. Kao, Z.-W. Jiang, and S.-C. Fang, "A computational simulation study of fluid mechanics of low-speed wind tunnel contractions," *Fluids*, vol. 2, no. 2, p. 23, 2017.
- [63] J. P. Van Doormaal and G. D. Raithby, "Enhancements of the simple method for predicting incompressible fluid flows," *Numerical heat transfer*, vol. 7, no. 2, pp. 147–163, 1984.
- [64] E. Bertolini, P. Pieringer, and W. Sanz, "Effect of different subgrid-scale models and inflow turbulence conditions on the boundary layer transition in a transonic linear turbine cascade," *International Journal of Turbomachinery, Propulsion and Power*, vol. 6, no. 3, p. 35, 2021.

- [65] G. Johl, M. Passmore, and P. Render, "Design methodology and performance of an indraft wind tunnel," *The aeronautical journal*, vol. 108, no. 1087, pp. 465–473, 2004.
- [66] P. Bradshaw, "Effects of streamline curvature on turbulent flow.," ADVISORY GROUP FOR AEROSPACE RESEARCH and DEVELOPMENT PARIS (FRANCE), Tech. Rep., 1973.
- [67] R. Madhusudn, P. A. Narayana, V. Balabaskaran, and E. Tulapurkara, "Boundary layer studies over an s-blade," *Fluid Dynamics Research*, vol. 14, no. 5, p. 241, 1994.
- [68] R. Lakshman and R. Basak, "Analysis of transformed fifth order polynomial curve for the contraction of wind tunnel by using openfoam," in *IOP conference series: materials science and engineering*, IOP Publishing, vol. 377, 2018, p. 012 048.
- [69] M. R. Lastra, J. M. F. Oro, M. G. Vega, E. B. Marigorta, and C. S. Morros, "Novel design and experimental validation of a contraction nozzle for aerodynamic measurements in a subsonic wind tunnel," *Journal of Wind Engineering and Industrial Aerodynamics*, vol. 118, pp. 35–43, 2013.
- [70] A. Benmalek, *Nonlinear development of Görtler vortices over variable curvature walls*. Arizona State University, 1993.
- [71] A. Ito, "The generation and breakdown of longitudinal vortices along a concave wall," *J. Japan Soc. Aero. Space Sci*, vol. 28, pp. 327–333, 1980.
- [72] L. De Souza, M. de Mendonça, M. De Medeiros, and M. Kloker, "Seeding of görtler vortices through a suction and blowing strip," *Journal of the Brazilian Society of Mechanical Sciences and Engineering*, vol. 26, pp. 269–279, 2004.
- [73] J. Ren and S. Fu, "Secondary instabilities of görtler vortices in high-speed boundary layer flows," *Journal of Fluid Mechanics*, vol. 781, pp. 388–421, 2015.
- [74] J. M. Floryan and W. S. Saric, "Wavelength selection and growth of görtler vortices," *AIAA journal*, vol. 22, no. 11, pp. 1529–1538, 1984.
- [75] H. Bippes and H. Deyhle, "The receptivity problem in boundary layers with streamwise vortex disturbances," *Zeitschrift fur Flugwissenschaften und Weltraumforschung*, vol. 16, no. 1, pp. 34–41, 1992.
- [76] P. Hall, "Taylor-gortler vortices in fully developed or boundary layer flows," in *Springer-Verlag London Ltd. Proceedings*, 1982, pp. 341–344.